이학박사 학위논문

Investigation of $j_{\mathrm{eff}} = 1/2$ State and Electronic and Magnetic Properties of A_2IrO_3 (A=Na,Li)

A_2IrO_3 (A=Na,Li)의 $j_{\mathrm{eff}=1/2}$ 상태와 또한 전자적 성질과 자성에 대한 연구

2012년 12월

서울대학교 대학원

물리천문학부

김 흥 식

Investigation of $j_{\text{eff}} = 1/2$ State and Electronic and Magnetic Properties of $A_2\text{IrO}_3$ (A=Na,Li)

Heung-Sik Kim

Supervised by

Professor **Jaejun Yu**

A Dissertation

Submitted to the Faculty of

Seoul National University

in Partial Fulfillment of

the Requirements for the Degree of

Doctor of Philosophy

December 2012

Department of Physics and Astronomy

Graduate School

Seoul National University

Abstract

Atomic spin-orbit coupling (SOC), which originates from the relativistic effects on the electrons near the atomic nuclei, becomes dominant energy scale for the compounds with heavy elements. It has been found that the atomic SOC has been the driving force for many novel quantum phenomena such as the topological insulator phases, the Rashba splitting of the surface bands on heavy metals, and also several exotic quantum magnetic ground states. The SOC manifests itself with the formation of the spin-orbital entangled states characterized by the total angular momentum j-quantum numbers, from which various nontrivial quantum phases arise. Especially in the case of some $5d$-transition metal oxides (TMO) with local cubic symmetry such as $Sr_{n+1}Ir_nO_{3n+1}$ $(n = 1, 2, \cdots)$, the $j_{\text{eff}} = 1/2$ states from the t_{2g} d-orbital and spin $s = 1/2$ entangled by the SOC become the low-energy degree of freedom near the Fermi level. Coupled with the on-site Coulomb correlations, which is another dominant energy energy scale on the $5d$-TMOs, the nature of the $j_{\text{eff}} = 1/2$ is suggested to yield emergent quantum phases in these compounds, especially in the case of A_2IrO_3-type compounds (A=Na,Li) for which the weak-topological insulator phase and the Kitaev spin-liquid phase has been suggested. Yet, except in the $Sr_{n+1}Ir_nO_{3n+1}$-series where the

$j_{\text{eff}} = 1/2$-ness is confirmed by both the experimental data and the first-principles electronic structure calculations, for A_2IrO_3 compounds the validity of such scenario has not been checked in detail.

In this thesis we investigate the role of the SOC on the electronic structure and magnetic properties of A_2IrO_3 compounds, especially the formation of the $j_{\text{eff}} = 1/2$ states and its consequences. To achieve quantitative argument based on realistic ground, we perform the first-principles electronic structure calculations based on the density-functional theory, analyze the basic electronic structures of these compounds with the strong spin-orbit couplings, and construct an effective tight-binding Hamiltonian based on the maximally localized Wannier functions on the energy ranges of our interest. From the Wannier function calculations for the entire t_{2g}-complex of Ir atoms and also for the t_{2g}+p-orbitals from the oxygen atoms, we can decompose the band structure into various hopping channels between neighboring Ir and oxygen atoms, and also understand the effect of the lattice strain on the band structures. Also, selecting the energy range to be near the Fermi level, we can directly read the nature of the state to be the $j_{\text{eff}} = 1/2$, and also construct the minimal tight-binding Hamiltonian which are directly mapped to the recently suggested theoretical models. It is found that, the long-range in-plane hopping terms inside the honeycomb lattice of Ir atoms make relatively strong contributions to the tight-binding model in addition to the relatively small but significant inter-layer hopping terms. The ratio between the nearest and the third nearest-neighbor hoppings, which can be controlled by the lattice strain, plays a critical role in determination of the Z_2-invariant character of Li_2IrO_3.

In the strong-coupling limit where the on-site correlation comes into play, we also derive an effective Hamiltonian and its parameters for the magnetic exchange interactions. The resulting pseudospin Hamiltonian consists of not only the Heisenberg term, but also the Kitaev terms as suggested in previous studies and additional Dzyaloshinskii-Moriya terms. By comparing out models to the results of previous studies we guess the ground states for the Na_2IrO_3 and Li_2IrO_3, and also we perform the DFT+U calculations as well as the classical spin energy for our effective spin model for the both compounds. We compare our results to experimental data, and discuss about the limitations in our approach.

Our work provides detailed understandings not only on the A_2MO_3-type compounds but also on other layered transition metal oxides with similar local geometry, as well as providing a realistic starting point for more elaborate analysis to discover novel quantum phases in these compounds.

Keywords: density functional theory, 5d-transition metal oxides, spin-orbit coupling, on-site Coulomb interactions, topological insulator, Wannier functions

Student Number: 2005-23191

Contents

Abstract **iv**

1 Introduction **1**

2 Computation Methods **6**

2.1 Density Functional Theory 7

2.1.1 Hohenberg-Kohn Theorem 7

2.1.2 Kohn-Sham Equation and Self-consistency 11

2.1.3 Local Density Approximation 13

2.1.4 Generalized Gradient Approximation 14

2.2 DFT+U Method 15

2.3 Spin-Orbit Coupling within Non-collinear Spin Formalism . . 19

2.3.1 Non-collinear Spin Density Functional 19

2.3.2 Spin-orbit Coupling 23

2.4 Maximally-Localized Wannier Functions 25

3 Electronic Structure and Topological Character of A_2IrO_3 in the Weak-Interaction Limit **27**

3.1 Introduction 28

3.2 Crystal structures 33
3.3 Electronic structures without the SOC 34
3.4 Electronic structures with the SOC 44
3.5 Effective Hamiltonian for the $j_{\text{eff}} = 1/2$-Wannier orbitals . . . 49
3.6 Strain-induced topological insulator phases in Li_2IrO_3 53
3.7 Discussions 58

4 Effective Magnetic Interactions in the Strong-Interaction Limit 62
4.1 Introduction 63
4.2 Robustness of the $j_{\text{eff}} = 1/2$ states under the on-site Coulomb correlations 66
4.3 Derivation of the pseudospin Hamiltonian 71
4.4 Guessing out the magnetic ground state 73
4.5 Phase diagram from the DFT calculations 80
4.6 Discussions 87

5 Summary and Perspectives 90

A Table of $j_{\text{eff}} = 1/2$ hopping terms 93

Bibliography 96

Abstract in Korean 102

List of Figures

3.1 Complex hopping terms in (a) KM- and (b) SI-model. Green, purple and blue arrows correspond to hopping terms that couple to σ_x, σ_y, and σ_z, respectively. Solid and dashed lines are hoppings that connects sites belonging to A- and B-sublattices, respectively. 30

3.2 (a) Crystal structure of A_2IrO_3 compounds in which alternate stacking of A- and $A_{1/3}Ir_{2/3}O_2$-layers. (b) Schematic top view showing the monoclinic stacking of the $A_{1/3}Ir_{2/3}O_2$-layers along the z-axis, in which the three inequivalent positions for the stacking of the triangular layers A, B, and C is marked as blue dot, red and green triangles, respectively. Vectors to the three nearest-neighboring Ir atoms $\delta_{1,2,3}$ and the next-nearest-neighbors $\mathbf{a}_{1,2,3}$ are illustrated as blue and red arrow, respectively. (c) Bond lengths between nearest-neighboring Ir atoms for Na_2IrO_3 and Li_2IrO_3. Ir-O bond lengths and the O-Ir-O bond angles for (d) Na_2IrO_3 and (e) Li_2IrO_3 are represented, showing the compression and the threefold rotation of IrO_6 octahedra. 35

3.3 Band structure and projected density of states of (a) Li_2IrO_3 and (b) Na_2IrO_3, where the first Brillouin zone used in the calculations and its special k-points are shown in (c). For both bands, the blue-colored Wannier-interpolated bands for the t_{2g} orbitals are overlaid onto the bands from the DFT calculations. (d) shows one of the constructed t_{2g}-Wannier orbitals in which significant oxygen p-orbital components are mixed. Note the small($\lesssim 0.1$eV) splitting of the e'_g doublet at the Γ-point. 36

3.4 Overlap between the neighboring $\{t_{2g}+p\}$-Wannier functions of Na_2IrO_3, illustrating the most significant hopping paths in the A_2IrO_3-type compounds. (a) hopping through the $dp\pi$-type hopping between Ir to O. (b)hopping through the $dd\sigma$-type direct overlap between nearest-neighboring t_{2g} orbitals (c) the $dpd\delta$ type, where the insets provides schematics of the relevant orbitals. (d,e) the next-nearest-neighbor hopping terms where the direction of the neighboring t_{2g}-orbital robes (d) toward the A-cation and (e) the toward the intermediate Ir site. 39

3.5 Bands and projected density of states of (a,c) Na_2IrO_3 and (b,d) Li_2IrO_3, where the orange curves are the bands without the *A*-site cations located (a,b) at the center of the Ir honeycomb and (c,d) between the two adjacent $A_{1/3}Ir_{2/3}O_2$ layers, while the bands from the original unit cell is inserted as guide for the eye. Note that the orange curves shows rigid shifts with respect to the black ones, which can be interpreted as shift of the orbital on-site energies. 42

3.6 Bands of t_{2g} orbitals of Na_2IrO_3(first and second rows) and Li_2IrO_3(third and fourth rows) with the SOC strength $\lambda_{SO} = 0$(first column), $\frac{1}{2}\lambda_0$(second column), λ_0(third column), and $2\lambda_0$(last column), where $\lambda_0 = 0.4eV$ is the natural the SOC strength of the Ir atom. The first and third rows shows a_{1g}-e'_g weights of the bands, while the second and fourth rows shows the $j_{\text{eff}} = 1/2$ and $3/2$ weights. Note that, all of the states are doubly degenerate due to the time-reversal and inversion symmetry. 46

3.7 The bands of (a) Na_2IrO_3 and (b) Li_2IrO_3 with the SOC plotted in black line overlaid with the thick blue curves representing the Wannier-downfolded bands. (c) About $\sim$80% of the weight of the constructed $j_{\text{eff}} = 1/2$ Wannier orbitals is centered at site 0 and the rest $\sim$20% is spread evenly along its neighboring sites 1,2, and 3. The components on the center site is mostly $j_{\text{eff}} = 1/2$ states with its (d) spin-up real part, (e) spin-down real part, and (f) the spin-down imaginary part are shown. 48

3.8 (Color online) Major hopping terms between the $j_{\text{eff}} = 1/2$-Wannier orbitals in both compounds, where the in-plane (a) nearest-neighbor, (b) next- and (c) third-nearest neighbor term and (d) inter-layer coupling terms are shown, whose values are in the Table. 3.4 LaTeX Error: Can be used only in preambleSee the LaTeX manual or LaTeX Companion for explanation.Your command was ignored.Type I ¡command¿ ¡return¿ to replace it with another command,or ¡return¿ to continue without it.3.4. The hopping terms with different character is represented as arrows with different shape and color. 51

3.9 (a) Schematic side view of Li_2IrO_3 where the inter-layer distance c is increased from its equilibrium distance c_0. (b) The change of t_{n1} and t_{n3} in terms of the inter-layer distance, and (c) the band inversion at the M_2-point at $c/c_0 = 1.26$. (d) d_{xy} orbital from one of the $\{t_{2g}+p\}$-Wannier orbitals, where the solid and transparent surfaces are from the results of $c/c_0 =$ 1.0 and 1.3, respectively, and the shaded arrow is along the out-of-plane direction. (e) The projected DOS of Ir d- and Li s-orbitals(10 times magnified) with increasing c/c_0 from 1.0 to 1.3. (f) Enhancement of the magnitude of the trigonal crystal field Δ_{tri} and the α in (3.18 LaTeX Error: Can be used only in preambleSee the LaTeX manual or LaTeX Companion for explanation.Your command was ignored.Type I ¡command¿ ¡return¿ to replace it with another command,or ¡return¿ to continue without it.3.18) in terms of the c/c_0-ratio. 56

3.10 (a) The direction of the uniaxial strain to Li_2IrO_3 along the $\mathbf{a}_1$ direction. (b) The position of the lowest unoccupied and highest unoccupied $j_{\text{eff}} = 1/2$ states in terms of the strain, where the Z_2-invariant of the system turns into (1;110) at $\Delta\mathbf{a}_1 \simeq 2\%$. (c-e) Evolution of the $j_{\text{eff}} = 1/2$ bands as the strain is increased. (d) The surface state of from the slab of 50 Ir layers where the surface band indices are illustrated in (g). 59

4.1 (a) Illustration of the nearest-neighbor γ-bonds in (4.1 LaTeX Error: Can be used only in preambleSee the LaTeX manual or LaTeX Companion for explanation.Your command was ignored.Type I ¡command¿ ¡return¿ to replace it with another command,or ¡return¿ to continue without it.4.1). (b) Two possible bondings between the neighboring t_{2g}-orbitals along the $\gamma = z$-bond. 64

4.2 Bands of (a,b) Na_2IrO_3 and (c,d) Li_2IrO_3, where the bands in the upper row (a,c) are from the Neel-AFM ground state, while the ones in the lower row (b,d) are from the FM states, where in every bands $U = 1.5$eV has been used. (e) and (f) shows the shift of the center of the occupied $j_{\text{eff}} = 1/2$-Wannier orbitals of Neel-AF and FM ground states, respectively. 69

4.3 Illustrative representation of the pseudospin exchange parameters (a,d) J, (b,e) $\mathbf{D}$ and (c,f) Γ for (a-c) Na_2IrO_3 and (d-f) Li_2IrO_3, where only components with magnitude larger than 3meV are shown. 75

4.4 Schematic spin ordering of (a) Neel-AF, (b) stripy, and (c) zigzag configuration. (d) shows the energy per an Ir atom of each configurations (4.17 LaTeX Error: Can be used only in preambleSee the LaTeX manual or LaTeX Companion for explanation.Your command was ignored.Type I ¡command¿ ¡return¿ to replace it with another command,or ¡return¿ to continue without it.4.17-4.20 LaTeX Error: Can be used only in preambleSee the LaTeX manual or LaTeX Companion for explanation.Your command was ignored.Type I ¡command¿ ¡return¿ to replace it with another command,or ¡return¿ to continue without it.4.20) in terms of the Hund's coupling in the case of Li_2IrO_3. 79

A.1 (Color online) (a) shows planar view of an Ir honeycomb lattice with position index of each Ir atoms in terms of the Bravais lattice vectors, with a single unit cell represented as dotted lines. (b) shows side view of the stacking of Ir lattices. In (a) and (b) $\mathbf{a}_1$ to $\mathbf{a}_3$ are the Bravais lattice vectors of the unit cell used in this calculation. (c) shows projected view of adjacent Ir layers onto the xy-plane, and major inter-layer hopping terms are illustrated as arrows with different colors and line types. 95

Chapter 1

Introduction

The physics of the transition metal oxides (TMO), especially in the $3d$-TMOs in which the coupling of spin, lattice, and orbital degree of freedom due to the strong on-site Coulomb correlations of the $3d$-orbitals, includes various emergent phenomena such as the Mott-Hubbard metal-insulator transitions, colossal magnetoresistence, and the high-temperature superconductivity. Due to the large on-site correlations and the hopping terms, other energy scales such as spin-orbit couplings have been treated as minor perturbations which yields only quantitative modifications to the ground states. It has been known that the magnitude of the spin-orbit coupling becomes stronger as the atomic number of the constituent elements increases, and found to modify the shape of the Fermi surface significantly as in the case of Sr_2RuO_4. Yet, it has not known until the discovery of the $j_{\text{eff}} = 1/2$ states in layers strontium iridate Sr_2IrO_4 and also the theoretical and experimental discovery of the topological insulators, that the the spin-orbit coupling can realize various exotic quantum phases by coupling the spin and or-

bital degrees of freedom in a nontrivial fashion. Based on the $j_{\text{eff}} = 1/2$- and $3/2$-states, which has become the new degree of freedom in the case of the $5d$-transition metal oxides, a number of topologically nontrivial phases including weak-topological insulators, Weyl semimetal, and axionic insulator phases has been suggested in the one-particle pictures.

The magnitude of the Coulomb correlations on the $5d$-transition metal oxides are decreased due to rather delocalized $5d$-orbitals, yet it is still comparable to those of the spin-orbit coupling and they are equally important in understanding the electronic and magnetic properties in these compounds. Indeed, it has been found that the spin-orbit coupling and the Coulomb correlation cooperate to yield the Mott-insulator phases in Sr_2IrO_4. Also, based on the picture where the $j_{\text{eff}} = 1/2$-states are correlated by the Coulomb interactions, various magnetic models which are hard to be realized without the help of the spin-orbit coupling has been suggested to realize gapless quantum spin liquid phases for the topological quantum computation.

Layered iridate compounds with a two-dimensional honeycomb Ir lattice, A_2IrO_3 (A = Li, Na), has drawn much attention as a candidate for topological insulators (TI) [1] with electron correlations since the first suggestion of the weak-topological insulator phase in Na_2IrO_3 based on the model tight-binding Hamiltonian of the $j_{\text{eff}} = \frac{1}{2}$-states. In addition, a recent discovery of spin-liquid phase on the honeycomb lattice[8] has triggered a number of researches about the role of correlations and the resulting emergent phases on the Kane-Mele (KM) model[9]. Both nontrivial hopping terms induced by the strong spin-orbit coupling and significant on-site Coulomb correlations make A_2IrO_3 a possible candidate for the exactly solvable spin

model suggested by Kitaev[13]. The study of the quantum spin Hamiltonian on the honeycomb lattice, especially the so-called the Heisenberg-Kitaev (HK) model[29] and its derivatives[31, 32, 35, 34], are active because of its possible application to topological quantum computations.

Recent experimental reports on the nature of magnetic ground state of Na_2IrO_3 and Li_2IrO_3 suggested that a zig-zag type AFM ordering within the Ir honeycomb lattice manifests in these compounds. Such an AFM ordering cannot be explained by the earlier HK model[29] with nearest-neighbor Heisenberg terms only. Further theoretical investigations have found that, the zig-zag type order can be stabilized when the second- and third-nearest neighbor Heisenberg terms[35, 36] are included. It is also suggested that, while Na_2IrO_3 is closer to the AFM-ordered regime, Li_2IrO_3 locates near the borderline between magnetic order and Kitaev spin liquid phase [34, 35] due to the more dominant Kitaev term present in Li_2IrO_3 compared to Na_2IrO_3.

Most of the discussions on the exotic ground state rely on the assumption of the robustness of $j_{\text{eff}} = 1/2$ states in A_2IrO_3. However, when considering the presence of trigonal crystal field in A_2IrO_3 as well as the band structures, it is not clear whether the $j_{\text{eff}} = 1/2$ state, originally suggested in Sr_2IrO_4[38, 39] without any trigonal field, can sustain its character in the honeycomb Ir lattice. Especially, recently published result on the electron structure of Na_2IrO_3 claims the formation of the molecular-orbital states which might discourage the formation of the localized $j_{\text{eff}} = 1/2$-states. Further there is a concern about the validity of the suggested spin Hamiltonians, partially due to the threefold distortions which are inherent in these

layers iridates, and to the long-range exchange interactions needed to incorporate the magnetic orders found in recent neutron scattering studies. Due to the increasing number of the relevant parameters, also to the difficulty in the growth of the high-quality crystals which are crucial for the study of magnetic properties, the search for the realistic electronic structures and theoretical arguments based on it is indispensable.

In this thesis, we perform first-principles calculations for the band structures of A_2IrO_3, analyze the electronic structure and the role of the spin-orbit coupling on the band structures, and present a realistic minimal effective Hamiltonian by using maximally-localized Wannier functions. By comparing the results for Na_2IrO_3 and Li_2IrO_3, our results state the difference in the electronic structures in terms of the size of the in-plane lattice constant. Also for both compounds we emphasize the significance of nontrivial long-range hopping terms arising from the extended nature of the Wannier orbitals. Such long-range hopping terms are important in understanding the low-energy electronic degree of freedom and the related magnetic properties, and also play a crucial role in determination of the topological character of this system. In the case of Li_2IrO_3, by controlling the lattice strain we can tune the ratio between nearest-neighbor and longer-range hopping parameters and have achieved the following phase transition to the topological insulator phases in our first-principles calculations. In addition, we derive effective $j_{\text{eff}} = 1/2$ pseudospin Hamiltonians from our noninteracting models for both compounds. The resulting Hamiltonian is characterized by the dominant Kitaev-type anisotropic second neighbor exchange terms, as well as smaller but significant Dzyaloshinskii-Moriya(DM) and Heisenberg

interactions. We estimate the magnitude of the nearest-neighbor Heisenberg and Kitaev terms suggested in Ref. [29], and discuss possible magnetic ground state in terms of Hund's coupling of Ir atom. Finally, based on our GGA+SO+U calculations we present a phase diagram with respect to the lattice size and the magnitude of the on-site correlations in search of the ground states in the intermediate strength of the correlations.

Chapter 2

Computation Methods

In this chapter, we briefly review the fundamentals of the density functional theory(DFT) - the Hohenberg-Kohn theorem, the Kohn-sham ansatz, and the exchange-correlation functionals - and the explain several method to treat the basis, pseudopotentials, and the spin-orbit coupling. Then we will discuss the DFT+U method to treat the on-site Coulomb correlations in DFT codes. After that, we will also summarize the formalism for the maximally-localized Wannier functions.

2.1 Density Functional Theory

The ultimate goal of the solid state physicists is to understand the following exact many-particle Hamiltonian,

$$\begin{aligned}\mathscr{H} = &-\sum_i \frac{\hbar^2}{2m_e}\nabla_i^2 - \sum_{i\neq I}\frac{Z_I e^2}{|\mathbf{r}_i - \mathbf{R}_I|} + \sum_{i\neq j}\frac{e^2}{|\mathbf{r}_i - \mathbf{r}_j|} \\ &-\sum_I \frac{\hbar^2}{2M_I}\nabla_I^2 + \sum_{I\neq J}\frac{Z_I Z_J e^2}{|\mathbf{R}_I - \mathbf{R}_J|}\end{aligned} \tag{2.1}$$

where the capital and small letters denote the indices and physical quantities of the nuclei and electrons, respectively. Adopting the Born-Oppenheimer approximation removes the second line of above Hamiltonian by freezing off the nucleus degree of freedom, still the remaining N-electron many-body problem reside in a region where the computational power of modern computers cannot reach. Instead, in the DFT we turn the unsolvable problem into the one we can treat, by choosing the density of the electrons as our central physical quantity instead of following the wave function approach. In the following sections we will review these fundamental grounds and practical implementations of DFT.

2.1.1 Hohenberg-Kohn Theorem

In the following, we state the Hohenberg-Kohn theorems which are the foundations of the modern DFT. We quote the theorems and their proofs from [14].

Theorem 1. For any non degenerate system of interacting particles in an external potential $V_{\text{ext}}(\mathbf{r})$, the potential $V_{\text{ext}}(\mathbf{r})$ is determined uniquely, except for a constant, by the ground state particle density $n_0(\mathbf{r})$.

Corollary 1. Since the Hamiltonian is thus fully determined, except for a constant energy shift of the energy, it follows that the many-body wave functions for all states (ground and excited) are determined. *Therefore all properties of the system are completely determined given only the ground state density* $n_0(\mathbf{r})$.

Proof of Theorem 1. Let us consider a N-electron system of density $n_0(\mathbf{r})$ in the external potential $V_{\text{ext}}(\mathbf{r})$, which has the ground state $|\Psi\rangle$ and the ground state energy E of the hamiltonian H. Now assume that another potential $V'_{\text{ext}}(\mathbf{r})$ gives the same density $n_0(\mathbf{r})$ but corresponds to $H' = T + U + V'$ and $|\Psi'\rangle$. By the assumptions of nondegenerate ground state,

$$\begin{aligned} E \equiv \langle\Psi|H|\Psi\rangle &< \langle\Psi'|H|\Psi'\rangle \\ &= \langle\Psi'|H + V'_{\text{ext}} - V'_{\text{ext}}|\Psi'\rangle \\ &= \langle\Psi'|H' - V'_{\text{ext}} + V_{\text{ext}}|\Psi'\rangle \\ &= E' - \int d\mathbf{r}[V'_{\text{ext}}(\mathbf{r}) - V_{\text{ext}}(\mathbf{r})]n_0(\mathbf{r}) \end{aligned} \tag{2.2}$$

Similarly, the interchange of the primed quantities by the unprimed ones in (2.2) yields,

$$E' < E - \int d\mathbf{r}[V_{\text{ext}}(\mathbf{r}) - V'_{\text{ext}}(\mathbf{r})]n_0(\mathbf{r}) \tag{2.3}$$

By adding (2.2) and (2.3), we obtain

$$E + E' < E' + E, \tag{2.4}$$

which leads to a contradiction.

Therefore the ground state electron density $n_0(\mathbf{r})$ cannot sustain two different external potential $V_{\text{ext}}(\mathbf{r})$ and $V'_{\text{ext}}(\mathbf{r})$. It follows that, $n_0(\mathbf{r})$ determines the ground state completely since it determines the potential uniquely.

Theorem 2. An *universal functional* for the energy $E[n]$ in terms of the density $n(\mathbf{r})$can be defined, valid for any external potential $V_{\text{ext}}(\mathbf{r})$. For any particular $V_{\text{ext}}(\mathbf{r})$, the exact ground state energy of the system is the global minimum value of this functional, and the density $n(\mathbf{r})$ that minimize the functional is the ground state density $n_0(\mathbf{r})$.

Corollary 2. The functional $E[n]$ alone is sufficient to determine the exact ground state energy and density.

Proof of Theorem 2. The following energy functional

$$\begin{aligned} E_V[n'] &\equiv \int d\mathbf{r} V_{\text{ext}}(\mathbf{r}) n'(\mathbf{r}) + F[n'(\mathbf{r})], \\ \text{where } F[n] &= \langle \Psi | T + U | \Psi \rangle \end{aligned} \tag{2.5}$$

and F is the sum of kinetic and Coulomb interaction energy. Note that the above $V_{\text{ext}}(\mathbf{r})$ is not assumed to be a functional of $n_0(\mathbf{r})$. From the Rayleigh-Ritz principle, an enegry functional is given by

$$\mathscr{E}_V[\Psi'] \equiv \langle \Psi' | V_{\text{ext}} | \Psi' \rangle + \langle \Psi' | T + U | \Psi' \rangle \tag{2.6}$$

has its minimum when $\Psi' = \Psi$. Now let us assume that Ψ' is the ground state of different density $n'(\mathbf{r})$. Then

$$\begin{aligned} \mathscr{E}_V[\Psi'] &= \int d\mathbf{r} V_{\text{ext}}(\mathbf{r}) n'(\mathbf{r}) + F[n'(\mathbf{r})] = E_v[n'] \\ &> \mathscr{E}_V[\Psi] = \int d\mathbf{r} V_{\text{ext}}(\mathbf{r}) n_0(\mathbf{r}) + F[n_0(\mathbf{r})] \equiv E_V[n_0] \end{aligned} \tag{2.7}$$

which shows the minimal property of energy associated with $n_0(\mathbf{r})$ and N.

Due to Theorem 1, one can in principle find everything about any system once the exact ground state density of that system is given. Also, Theorem 2 tells us that there is a *system-independent universal* energy functional except the system-dependent $v(\mathbf{r})$. Once the energy functional is known, than in principle one can get the exact ground state density and ground state energy by minimizing the functional with respect to the density. Problem is, not much information about the quantum mechanical properties are contained in the density, and the relations with the density and physical properties of the system are hardly known. Also, any realistic energy functionals should have nonanalytic behavior with respect to the occupation numbers for the electronic states due to the presence of the electronic correlations, which is hardly to be captured within the density-only functionals. Due to the these reasons, one should solve the N-particle Schrödinger equation with only the information of the ground state density, which is still a difficult task. In the next section we state the Kohn-Sham ansatz, which changes the N-particle problem into a practically solvable fictitious *one-particle* problem.

2.1.2 Kohn-Sham Equation and Self-consistency

The problem of the density-only approach is already known from the result of the Thomas-Fermi approximations, which is the earliest density functional approach to the quantum systems. Replacing all of the orbital-dependent terms such as the kinetic energy, the Thomas-Fermi approach lose the power to treat the quantum properties such as the shell structure of atoms and binding of molecules. Instead, Kohn and Sham choose to preserve the kinetic energy operator in a fictitious one-particle system, assuming that *this one-particle system reproduces the ground state density of the original N-particle many-body system* given the exact potential energy functional for the one-particle Hamiltonian. From now on we call this the Kohn-Sham(KS) Hamiltonian.

We assume the one-particle orbitals ψ_i for a given i-th state, which we will call KS orbitals. The variational principle is applied to obtain the Kohn-Sham (KS) equation and self-consistent field equation[16]. Starting from a trial charge density $n(\mathbf{r}) = \sum_i |\psi_i|^2$, we minimize the total energy $E[n]$ with the constraint of normalization. The summation and integration run to the total number of electrons, N. The energy variation with respect to $\psi_i(\mathbf{r})$ (or equivalently, $\psi_i^*(\mathbf{r})$),

$$\frac{\delta}{\delta \psi_i^*(\mathbf{r})} \left(E[n] - \sum_j \varepsilon_j \int d\mathbf{r} |\psi_j|^2 \right) = 0 \tag{2.8}$$

gives KS equation:

$$\left(-\frac{1}{2}\nabla^2 + v_{\mathrm{KS}}^{\sigma}[n(\mathbf{r})] \right) \psi_i(\mathbf{r}) = \varepsilon_i \psi_i(\mathbf{r}) \tag{2.9}$$

Here, v_{KS} is the sum of the external potential, Hartree, exchange, and the correlation terms

$$\begin{aligned} v_{\mathrm{KS}}^{\sigma}(\mathbf{r}) &\equiv \frac{\delta E_{\mathrm{ext}}[n]}{\delta n(\mathbf{r},\sigma)} + \frac{\delta E_{\mathrm{Hartree}}[n]}{\delta n(\mathbf{r},\sigma)} + \frac{\delta E_{\mathrm{xc}}[n]}{\delta n(\mathbf{r},\sigma)} \\ &= V_{\mathrm{ext}}(\mathbf{r}) + V_{\mathrm{Hartree}}(\mathbf{r}) + V_{\mathrm{xc}}^{\sigma}(\mathbf{r}), \end{aligned} \tag{2.10}$$

where the Hartree term is the Coulomb potential from the charge density

$$V_{\mathrm{Hartree}}(\mathbf{r}) = \int d\mathbf{r}' \frac{n(\mathbf{r}')}{|\mathbf{r}-\mathbf{r}'|}, \tag{2.11}$$

and the exchange-correlation potential is spin-dependent due to the presence of the *exchange-correlation hole* as follows:

$$V_{\mathrm{xc}}(\mathbf{r},\sigma) = \varepsilon_{\mathrm{xc}}([n],\mathbf{r}) + n(\mathbf{r}) \frac{\delta \varepsilon_{\mathrm{xc}}([n],\mathbf{r})}{\delta n(\mathbf{r},\sigma)} \tag{2.12}$$

where the exchange-correlation energy $\varepsilon_{\mathrm{xc}}([n],\mathbf{r})$ is expressed in terms of the exchange-correlation hole $[g_{\mathrm{xc}}(\mathbf{r},\sigma;\mathbf{r}',\sigma') - 1]$ such as

$$\varepsilon_{\mathrm{xc}}([n],\mathbf{r}) = \frac{1}{2} \sum_{\sigma\sigma'} \int d\mathbf{r}' \frac{n(\mathbf{r},\sigma) n(\mathbf{r}',\sigma')}{|\mathbf{r}-\mathbf{r}'|} [g_{\mathrm{xc}}(\mathbf{r},\sigma;\mathbf{r}',\sigma') - 1]. \tag{2.13}$$

The exchange-correlation hole can be understood as a pair correlation function regarding the correlation between the position of any two electrons, and can be decomposed into exchange and correlation hole, each of them representing the repulsion between the electrons with the same spin due to the Pauli exclusion principle and the repulsion due to the Coulomb correlation, respectively. Due to the presence of the second Hohenberg-Kohn

theorem, in principle these exchange-correlation hole is a functional of the electron density, still it is a highly nontrivial job to find the exact functional form. In the next section we explain two approximations that construct the functional with the electron density only and with the spatial gradient of the density. With them, now the solution of the KS equation ψ_i gives new density $n(\mathbf{r})$ and one can construct the self-consistent equations.

It should be noted that ε_i is introduced as a Lagrange multiplier for the fictitious single particle KS wavefunction ψ_i, and therefore it is not the physical single particle eigenenergy. Still, one can assign physical meanings to the KS eigenvalues. First, in a finite system the highest occupied KS eigenvalue is minus the ionization energy. Also, the KS eigenvalues and the KS orbitals can be understood as a zeroth-order approximations for the energy and the many-particle states, and they can be used as a starting point of the more elaborate many-body calculations such as the fixed-node diffusion Monte Carlo methods.

2.1.3 Local Density Approximation

The simplest and practical approach for the exchange-correlation functional is the so-called local density approximation (LDA). In the slowly varying inhomogeneous electron system, E_{xc} can be written as

$$E_{\mathrm{xc}}[n] \approx \int d\mathbf{r} n(\mathbf{r}) \varepsilon_{\mathrm{xc}}(n(\mathbf{r})) \tag{2.14}$$

where $\varepsilon_{xc}(n(\mathbf{r}))$ defined in (2.13). LDA assumes the slowly varying electron density in the real space and treats the inhomogeneous system as a piece-

wise homogeneous one. Space is devided into a set of small discrete cells and the electron density in the volume ω_i is assumed to be constant. Then energy functional $G[n]$ is calculated by

$$G(n) \approx \sum_i \omega_i g^{homo}(n_i) \tag{2.15}$$

where $g^{homo}(n_i)$ is the energy density of an homogeneous electron system. Practically the correlation energy functional is constructed by fitting the functional form to the result of the quantum Mote Carlo simulation of the uniform electron gas[17].

2.1.4 Generalized Gradient Approximation

In the cases where inhomogeneity of the system is severe so that the piecewise continuity argument in the previous section is not relevant, then one should take into account the nonlocal effect of the density on the energy functional. The simplest way to incorporate the non locality is considering the effect of the density gradient. In the so-called generalized gradient approximation(GGA), the exchange-correlation energy has the following form:

$$\begin{aligned} E_{xc}^{\mathrm{GGA}}[n^{\uparrow}, n^{\downarrow}] &= \int d\mathbf{r} n(\mathbf{r}) \varepsilon_{xc}(n^{\uparrow}, n^{\downarrow}, |\nabla n^{\uparrow}|, |\nabla n^{\downarrow}|, \cdots) \\ &\equiv \int d\mathbf{r} \varepsilon_x^{\mathrm{hom}}(n) F_{xc}(n^{\uparrow}, n^{\downarrow}, |\nabla n^{\uparrow}|, |\nabla n^{\downarrow}|, \cdots) \end{aligned} \tag{2.16}$$

where F_{xc} is dimensionless and $\varepsilon_{xc}^{\mathrm{him}}(n)$ is the exchange energy of the spinless homogeneous electron gas. Here, F_{xc} is expanded in terms of the dimension-

less density gradients of m-th order

$$s_m = \frac{|\nabla^m n|}{(2k_F)^m n}. \tag{2.17}$$

Numerous forms for F_{xc} in terms of s_m has been suggested, and among them the ones proposed by Perdew, Burke, and Enzerhof[18], which is most widely used, is adopted in this work.

2.2 DFT+U Method

One of the serious problem of the exchange-correlation functionals introduced in previous section is that, they do not cancel the self-interactions exactly. Such self-interaction problem becomes severe in the systems with strong on-site Coulomb repulsions, with which the systems favor integer occupation for the orbitals, and both LDA and GGA yields qualitatively incorrect magnetic ground states in such systems. One of the methods that cure such problem is the DFT+U method, which we will briefly state in this section.

DFT+U method[19] is one of the simplest orbital-dependent functionals in which a generalized Hubbard model is introduced in order to treat the localized d- and f-electrons based on the unrestricted Hatree-Fock method. Then, in conjunction with the generalized Hubbard model, DFT+U total energy functional is given by adding the energy E_U^0 of a Hubbard model for the localized electrons to exchange-correlation functional and subtracting a double counting energy E_U^{dc} of the localized electrons described in a mean-

field level:

$$E_{\mathrm{LDA}+U} = E_{\mathrm{DFT}} + E_{\mathrm{HF}} - E_U^{dc}. \tag{2.18}$$

There are has two different kind of DFT+U formalism depending on how to choose the form of E_{HF}. First, the rotationally-invariant formalism introduced by Lichtenstein *et al.*[20] choose E_{HF} to be

$$E_{\mathrm{HF}}^{\mathrm{RI}} = \frac{1}{2}\sum_{\{\gamma\}} \left(U_{\gamma_1\gamma_3\gamma_2\gamma_4} - U_{\gamma_1\gamma_2\gamma_4\gamma_2}\right) \hat{n}_{\gamma_1\gamma_2}\hat{n}_{\gamma_3\gamma_4} \tag{2.19}$$

where the density matrix is determined by the PAW on-site occupancies in the projector-augmented wave formalism

$$\hat{n}_{\gamma_1\gamma_2} = \langle \Psi^{s_2} | m_2 \rangle \langle m_1 | \Psi^{s_1} \rangle \tag{2.20}$$

and the on-site electron-electron interaction

$$U_{\gamma_1\gamma_3\gamma_2\gamma_4} = \langle m_1 m_3 | \frac{1}{|\mathbf{r} - \mathbf{r}'|} | m_2 m_4 \rangle \delta_{s_1 s_2} \delta_{s_3 s_4} \tag{2.21}$$

where m represents azimuthal quantum number of the spherical harmonics in the given orbital complex. The matrix element of the bare Coulomb interaction is represented in terms of the Slater's integrals F^0, F^2, F^4, and F^6 such that

$$\langle m_1 m_3 | \frac{1}{|\mathbf{r} - \mathbf{r}'|} | m_2 m_4 \rangle = \sum_k a_k(m_1, m_2, m_3, m_4) F^k \tag{2.22}$$

where $0 \leq k \leq 2l$ and

$$a_k(m_1, m_2, m_3, m_4) = \frac{4\pi}{2k+1} \sum_{q=-k}^{k} \langle lm_1|Y_{kq}|lm_2\rangle \langle lm_3|Y_{kq}^*|lm_4\rangle. \tag{2.23}$$

Here, if we represent $U_{\gamma_1\gamma_3\gamma_2\gamma_4}$ in terms of the Slater's integrals for the bare electrons, then it becomes unscreened Coulomb interactions. Since the Coulomb interactions are screened inside solids, we use system- and element-specific effective on-site Coulomb and exchange parameters U and J such that $F^0 = U$, $F^2 = \frac{14}{1+0.625}J$, $F^4 = 0.625F^2$, and $F^6 = 0$ for d-electrons.

Instead of using the rotationally-invariant form, we can adopt simplified formalism with spherically averaged $U_{\gamma_1\gamma_3\gamma_2\gamma_4}$[21] such that

$$E_{\mathrm{HF}}^{\mathrm{simple}} = \frac{1}{2}\sum_{\alpha} U_\alpha \sum_{\sigma mm'} n_{\alpha m}^{\sigma} n_{\alpha m'}^{-\sigma} + \frac{1}{2}\sum_{\alpha}(U_\alpha - J_\alpha) \sum_{\sigma m \neq m'} n_{\alpha m}^{\sigma} n_{\alpha m'}^{\sigma} \tag{2.24}$$

where σ is the spin index and $\alpha \equiv (ilp)$ with the site index i, angular momentum quantum number l, and multiplicity number of radial basis function p. $n_{\alpha m}^{\sigma}$ is an eigenvalue of the occupation number matrix to be discussed later.

One possible choice of the double counting term E_U^{dc} is

$$E_U^{dc} = \frac{1}{2}\sum_{\alpha} U_\alpha N_\alpha(N_\alpha - 1) - \frac{1}{2}\sum_{\alpha} J_\alpha \sum_{\sigma} N_\alpha^{\sigma}(N_\alpha^{\sigma} - 1) \tag{2.25}$$

where $N_\alpha^{\sigma} = \sum_m n_{\alpha m}^{\sigma}$ and $N_\alpha = N_\alpha^{\uparrow} + N_\alpha^{\downarrow}$. It is noted that the above expression for the double counting term is also derived by assuming an integer occupation number, 0 or 1, in the atomic limit. Thus, this form is expected to be valid for highly localized d- and f-electrons. Another possible way is to es-

timate the double counting term by assuming the uniform occupancy [22]. In the codes we have used in this thesis, OpenMX and VASP, atomic limit is adopted, since the DFT+U formalism is adopted for the localized d- and f-electrons.

In the case of the simplified approach, the energy correction $E_U \equiv E_{\rm HF} - E_U^{dc}$ to the exchange-correlation energy can be written by a penalty functional as follows:

$$E_U = \frac{1}{2}\sum_{\alpha}(U_\alpha - J_\alpha)\sum_{\sigma}\{{\rm Tr}(n_\alpha^\sigma) - {\rm Tr}(n_\alpha^\sigma n_\alpha^\sigma)\} \tag{2.26}$$

If $(U_\alpha - J_\alpha)$ is positive, the energy correction always impose a positive penalty on the total energy except for the case with a diagonal integer occupation number 0 or 1, which leads to the orbital polarization. It is easy to verify that the derivative of the functional with respect to N_α^σ is discontinuous at an integer value, since the diagonal occupation number $n_{\alpha m}^\sigma$ varies 0 to 1 in principle. It is convenient to define an effective Coulomb energy as $\bar{U}_\alpha \equiv (U_\alpha - J_\alpha)$, since only the difference is important in this spherically averaged but still rotationally invariant form of DFT+U energy functional.

Considering the multiple structure of d- and f-orbitals and the rotational invariance of the energy correction, we can make an unitary transformation of Eq. (2.19) with respect to each subshell α:

$$\begin{aligned} E_U &= \frac{1}{2}\sum_{\alpha}\bar{U}_\alpha\sum_{\sigma}[{\rm Tr}(\mathbb{A}_\alpha n_\alpha^\sigma \mathbb{A}_\alpha^\dagger) - {\rm Tr}(\mathbb{A}_\alpha n_\alpha^\sigma \mathbb{A}_\alpha^\dagger \mathbb{A}_\alpha n_\alpha^\sigma \mathbb{A}_\alpha^\dagger)] \\ &= \frac{1}{2}\sum_{\alpha}\bar{U}_\alpha\sum_{\sigma}\left[\sum_{m}\mathbf{n}_{\alpha mm}^\sigma - \sum_{mm'}\mathbf{n}_{\alpha mm'}^\sigma \mathbf{n}_{\alpha m'm}^\sigma\right], \end{aligned} \tag{2.27}$$

where the off-diagonal terms within the subshell α of the occupation number matrix are taken into account, while those between subshells are neglected.

2.3 Spin-Orbit Coupling within Non-collinear Spin Formalism

2.3.1 Non-collinear Spin Density Functional

A two component spinor wave function is defined by

$$| \psi_\nu \rangle = | \varphi_\nu^\alpha \alpha \rangle + | \varphi_\nu^\beta \beta \rangle \tag{2.28}$$

where $| \varphi_\nu^\alpha \alpha \rangle \equiv | \varphi_\nu^\alpha \rangle \, | \alpha \rangle$ with a spatial function $| \varphi_\nu^\alpha \rangle$ and a spin function $| \alpha \rangle$. Then the density operator is written as

$$\mathbf{n} = \sum_\nu f_\nu \, | \psi_\nu \rangle \langle \psi_\nu | = \sum_\nu f_\nu \begin{pmatrix} | \varphi_\nu^\alpha \rangle \\ | \varphi_\nu^\beta \rangle \end{pmatrix} \begin{pmatrix} \langle \varphi_\nu^\alpha | & \langle \varphi_\nu^\beta | \end{pmatrix} \tag{2.29}$$

where the last expression is in the spinor representation. With the definition of the density operator $\mathbf{n}$, a non-collinear electron density in real space is given by

$$\begin{aligned} n_{\sigma\sigma'} &= \langle \mathbf{r}\sigma \,|\, \mathbf{n} \,|\, \mathbf{r}\sigma' \rangle \\ &= \sum_\nu f_\nu \varphi_\nu^\sigma \varphi_\nu^{\sigma' *} \end{aligned} \tag{2.30}$$

where $\sigma, \sigma' = \alpha$ or β and $\mid \mathbf{r}\rangle$ is a position eigenvector. Then the up- and down-spin densities at each point are defined by diagonalizing a density matrix consisting of non-collinear electron densities as follows:

$$\begin{aligned} \begin{pmatrix} n'_{\uparrow} & 0 \\ 0 & n'_{\downarrow} \end{pmatrix} &= U\mathbf{n}U^{\dagger} \\ &= U \begin{pmatrix} n_{\alpha\alpha} & n_{\alpha\beta} \\ n_{\beta\alpha} & n_{\beta\beta} \end{pmatrix} U^{\dagger} \end{aligned} \tag{2.31}$$

The non-collinear total energy functional [24, 25] could be written as

$$\begin{aligned} E_{\text{tot}} &= \sum_{\sigma\nu} f_{\nu} \langle \varphi_{\nu}^{\sigma} \mid \hat{T} \mid \varphi_{\nu}^{\sigma} \rangle + \sum_{\sigma\sigma'} \int w_{\sigma\sigma'} n_{\sigma'\sigma} \\ &+ \frac{1}{2} \int\int d\mathbf{r} d\mathbf{r}' \frac{n'(\mathbf{r}) n'(\mathbf{r}')}{|\mathbf{r} - \mathbf{r}'|} + E_{xc}(n_{\sigma\sigma'}), \end{aligned} \tag{2.32}$$

where the first term is the kinetic energy, the second the electron-core Coulomb energy, the third and the fourth are the Hatree and the exchange-correlation energy, respectively. Alternatively, the total energy E_{tot} can be expressed in terms of the KS eigen energies ε_{ν} as follows:

$$E_{\text{tot}} = E_{\text{band}} - \frac{1}{2} \int d\mathbf{r} v_{\text{H}} n' - \int d\mathbf{r} \text{Tr}(v_{xc}\mathbf{n}) + E_{xc} \tag{2.33}$$

where v_{xc} is a non0collinear exchange-correlation potential. To take a variational principle on E_{tot} with respect to the spatial wave functions, let us

introduce a fuctional F:

$$F = E_{\mathrm{tot}} + \sum_{\nu\nu'} \varepsilon_{\nu\nu'}(\delta_{\nu\nu'} - \langle \psi_\nu \mid \psi_{\nu'} \rangle). \tag{2.34}$$

The variation of F with respect to the spatial wave functions is found to be

$$\frac{\delta F}{\delta \varphi_\mu^{\sigma *}} = \hat{T}\varphi_\mu^\sigma + \sum_{\sigma'} w_{\sigma\sigma'}\varphi_\mu^{\sigma'} + v_{\mathrm{H}}\varphi_\mu^\sigma + \sum_{\sigma'} v_{xc}^{\sigma\sigma'}\varphi_\mu^{\sigma'} - \sum_\nu \varepsilon_{\mu\nu}\varphi_\nu^\sigma \tag{2.35}$$

with

$$v_{\mathrm{H}} = \int d\mathbf{r}' \frac{n'(\mathbf{r}')}{|\mathbf{r} - \mathbf{r}'|},\ v_{xc}^{\sigma\sigma'} = \frac{\delta E_{xc}}{\delta n_{\sigma'\sigma}}.$$

Considering a unitary transformation of φ_μ^σ so that $epsilon_{\mu\nu}$ can be diagonalized, we can obtain the non-collinear KS equation.

$$\begin{pmatrix} \hat{T} + w_{\alpha\alpha} + v_{\mathrm{H}} + v_{xc}^{\alpha\alpha} & w_{\alpha\beta} + v_{xc}^{\alpha\beta} \\ w_{\beta\alpha} + v_{xc}^{\beta\alpha} & \hat{T} + w_{\beta\beta} + v_{\mathrm{H}} + v_{xc}^{\beta\beta} \end{pmatrix} \begin{pmatrix} \varphi_\mu^\alpha \\ \varphi_\mu^\beta \end{pmatrix} = \varepsilon_\mu \begin{pmatrix} \varphi_\mu^\alpha \\ \varphi_\mu^\beta \end{pmatrix} \tag{2.36}$$

The off-diagonal potentials consist of the exchange-correlation potential and the other contributions w such as spin-orbit interactions.

As denoted in Eq. (2.39), the unitary matrix U diagonalizes the total non-collinear density matrix rather than that of each state ν. Since the exchange-correlation term is approximated by the LDA or GGA functional, once the non-collinear density matrix $\mathbf{n}$ is diagonalized, the diagonal components for each up- and down-densities are used to evaluate the exchange-correlation

potential $\bar{v}_{xc}$ within LDA or GGA.

$$\begin{aligned}
\bar{v}_{xc} &= \begin{pmatrix} v_{xc}^{\uparrow} & 0 \\ 0 & v_{xc}^{\downarrow} \end{pmatrix} \\
&= \frac{1}{2}(v_{xc}^{\uparrow} + v_{xc}^{\downarrow})\sigma_0 + \frac{1}{2}(v_{xc}^{\uparrow} - v_{xc}^{\downarrow})\sigma_3 \\
&= v_{xc}^{0}\sigma_0 + \Delta v_{xc}\sigma_3. \qquad (2.37)
\end{aligned}$$

where σ_0 is 2×2 identity matix and σ_3 is the third components of Pauli matrices. Then, the potential $\bar{v}_{xc}$ is transformed to the non-collinear exchange-correlation potential v_{xc} by using $U^{\dagger}$

$$\begin{aligned}
v_{xc} &= U^{\dagger}\bar{v}_{xc}U \\
&= v_{xc}^{0}\sigma_0 + \Delta v_{xc}U^{\dagger}\sigma_3 U \\
&= v_{xc}^{0}\sigma_0 + \Delta v_{xc}\bar{\sigma}_3 \qquad (2.38)
\end{aligned}$$

Then, the effective potnetial v_{eff} can be written in Pauli matrices as follows:

$$v_{\text{eff}} = v_{\text{eff}}^{0}\sigma_0 + \Delta v_{xc}\bar{\sigma}_3 + w \qquad (2.39)$$

where

$$v_{\text{eff}}^{0} = v_{\text{H}} + v_{xc}^{0},\ w = \begin{pmatrix} w_{\alpha\alpha} & w_{\alpha\beta} \\ w_{\beta\alpha} & w_{\beta\beta} \end{pmatrix}.$$

2.3.2 Spin-orbit Coupling

In our mehtods, the spin-orbit coupling is incorporated through j-dependent pseudo-potnetials [26]. Under a spherical potential, coupled Dirac equations for the radial parts are given by

$$\frac{dG_{nlj}}{dr} + \frac{\kappa}{r} G_{nlj} - a\left[\frac{2}{a^2} + \varepsilon_{nlj} - V(r)\right] F_{nlj} = 0 \tag{2.40}$$

$$\frac{dF_{nlj}}{dr} - \frac{\kappa}{r} F_{nlj} + a\left[\varepsilon_{nlj} - V(r)\right] G_{nlj} = 0, \tag{2.41}$$

where G and F are the majority and minority components of the radial wave function, $a \equiv 1/c (= 1/137 \text{in a.u.})$, $\kappa = l$ and $\kappa = -(l+1)$ for $j = l - \frac{1}{2}$ and $j = l\frac{1}{2}$, respectively. Combining both equations and eliminating F, we have the following equation for G:

$$\left[\frac{1}{2M(r)}\left(\frac{d^2}{dr^2} + \frac{a^2}{2M(r)}\frac{dV}{dr}\frac{d}{dr} + \frac{a^2}{2M(r)}\frac{\kappa}{r}\frac{dV}{dr} - \frac{\kappa(\kappa+1)}{r^2}\right) + \varepsilon_{nlj} - V\right] G_{nlj} = 0 \tag{2.42}$$

with

$$M(r) = 1 + \frac{a^2(\varepsilon_{nlj} - V)}{2}.$$

By solving Eq. (2.50) numerically and generating j-dependent pseudo-potential V_{ps}^{j}, we can define a general pseudo-potnetial by

$$V_{\text{ps}} = \sum_{lm}\left[\mid \Phi_J^M \rangle V_{\text{ps}}^{l+\frac{1}{2}} \langle \Phi_J^M \mid + \mid \Phi_{J'}^{M'} \rangle V_{\text{ps}}^{l-\frac{1}{2}} \langle \Phi_{J'}^{M'} \mid \right], \tag{2.43}$$

where for $J = l + \frac{1}{2}$ and $M = m + \frac{1}{2}$

$$| \Phi_J^M \rangle = \left(\frac{l+m+1}{2l+1} \right)^{\frac{1}{2}} | Y_l^m \rangle | \alpha \rangle + \left(\frac{l-m}{2l+1} \right)^{\frac{1}{2}} | Y_l^{m+1} \rangle | \beta \rangle, \tag{2.44}$$

and for $J' = l - \frac{1}{2}$ and $M' = m - \frac{1}{2}$

$$| \Phi_{J'}^{M'} \rangle = \left(\frac{l-m+1}{2l+1} \right)^{\frac{1}{2}} | Y_l^{m-1} \rangle | \alpha \rangle + \left(\frac{l+m}{2l+1} \right)^{\frac{1}{2}} | Y_l^m \rangle | \beta \rangle. \tag{2.45}$$

Φ_J^M and $\Phi_{J'}^{M'}$ are constituents of the eigenfunction of Dirac equation. By introducing a local potential V_{L} which approaches $-\frac{Z_{\mathrm{eff}}}{r}$ as r increases, the j-dependent pseudo-potential is divided into two parts:

$$V_{\mathrm{ps}}^{l+\frac{1}{2}} = V_{\mathrm{NL}}^{l+\frac{1}{2}} + V_{\mathrm{L}} \tag{2.46}$$

$$V_{\mathrm{ps}}^{l-\frac{1}{2}} = V_{\mathrm{NL}}^{l-\frac{1}{2}} + V_{\mathrm{L}} \tag{2.47}$$

The non-local potential $V_{\mathrm{NL}}^{l+\frac{1}{2}}$ and $V_{\mathrm{NL}}^{l-\frac{1}{2}}$ are non-zero within a certain cutoff radius. Then the pseudo-potential defined by Eq. (2.51) is written by

$$\begin{aligned} V_{\mathrm{ps}} &= V_{\mathrm{L}} + \sum_{lm} \left[| \Phi_J^M \rangle V_{\mathrm{NL}}^{l+\frac{1}{2}} \langle \Phi_J^M | + | \Phi_{J'}^{M'} \rangle V_{\mathrm{NL}}^{l-\frac{1}{2}} \langle \Phi_{J'}^{M'} | \right] \\ &= V_{\mathrm{L}} + \hat{V}_{\mathrm{NL}}^{l+\frac{1}{2}} + \hat{V}_{\mathrm{NL}}^{l-\frac{1}{2}}. \end{aligned} \tag{2.48}$$

The non-local part can be transformed by the Blochl projector into a separable form.

2.4 Maximally-Localized Wannier Functions

Electronic structure calculation typically solves problems in terms of the Bloch function basis, which are characterized by the band index n and the crystal momentum $\mathbf{k}$. Alternatively, one can choose Wannier functions by Fourier-transforming the Block functions so that they are characterized by the Bravais lattice vector $\mathbf{R}$ instead of the momentum $\mathbf{k}$ such that

$$w_{n\mathbf{R}}(\mathbf{r}) = \frac{V}{(2\pi)^3} \int_{\mathrm{BZ}} \left[\sum_m U_{mn}^{(\mathbf{k})} \psi_{m\mathbf{k}}(\mathbf{r}) \right] e^{-i\mathbf{k}\cdot\mathbf{R}} d\mathbf{k} \tag{2.49}$$

where V is the unit cell volume, the integral is over the Brillouin zone, and $\mathbf{U}^{(\mathbf{k})}$ is a unitary matrix that mixes the Bloch states at each $\mathbf{k}$ point. $\mathbf{U}^{(\mathbf{k})}$ is a '*gauge*' degree of freedom since it does not be determined uniquely in the matrix calculations but does not affect any physically observable properties. Due to such problem, Wannier functions had not been widely used in electronic structure calculations until the seminal work of Marzari and Vanderbilt, in which an way to determine $\mathbf{U}^{(\mathbf{k})}$ uniquely is developed so that the the spread functional Ω is minimized[57]. The spread functional Ω is the amount of the spatial spread of the Wannier function, and is defined as follows:

$$\Omega = \sum_n \left[\langle w_{n\mathbf{0}}(\mathbf{r}) | r^2 | w_{n\mathbf{0}}(\mathbf{r}) \rangle - |\langle w_{n\mathbf{0}}(\mathbf{r}) | \mathbf{r} | w_{n\mathbf{0}}(\mathbf{r}) \rangle|^2 \right]. \tag{2.50}$$

The total spread can be decomposed into a gauge-invariant term Ω_{I} plus a term $\tilde{\Omega}$ which is dependent on the choice of $\mathbf{U}^{(\mathbf{k})}$. $\tilde{\Omega}$ can be further decomposed into terms diagonal and off-diagonal in the Wannier function basis,

Ω_{D} and Ω_{OD},

$$\Omega = \Omega_{\mathrm{I}} + \Omega_{\mathrm{D}} + \Omega_{\mathrm{OD}} \tag{2.51}$$

where

$$\Omega_{\mathrm{I}} = \sum_{n} \left[\langle w_{n\mathbf{0}}(\mathbf{r}) | r^2 | w_{n\mathbf{0}}(\mathbf{r}) \rangle - \sum_{n} \sum_{\mathbf{R}\neq 0} |\langle w_{m\mathbf{R}}(\mathbf{r}) | \mathbf{r} | w_{n\mathbf{0}}(\mathbf{r}) \rangle|^2 \right] \tag{2.52}$$

$$\Omega_{\mathrm{D}} = \sum_{n} \sum_{\mathbf{R}\neq 0} |\langle w_{n\mathbf{R}}(\mathbf{r}) | \mathbf{r} | w_{n\mathbf{0}}(\mathbf{r}) \rangle|^2 \tag{2.53}$$

$$\Omega_{\mathrm{OD}} = \sum_{m\neq n} \sum_{\mathbf{R}\neq 0} |\langle w_{m\mathbf{R}}(\mathbf{r}) | \mathbf{r} | w_{n\mathbf{0}}(\mathbf{r}) \rangle|^2 \tag{2.54}$$

In the maximally-localized Wannier function formalism, the gauge-dependent spread $\tilde{\Omega}$ is minimized with respect to the set of $\mathbf{U}^{(\mathbf{k})}$.

For the band complex which overlaps with other irrelevant bands, one needs to 'disentangle' the bands from the other ones. In this case, one first set an energy range that all of the bands are taken inside. For the Bloch states, one performs an unitary transform such that

$$|u^{\mathrm{opt}}_{n\mathbf{k}}\rangle = \sum_{m\in N^{(\mathbf{k})}_{\mathrm{win}}} U^{\mathrm{dis}(\mathbf{k})}_{mn} |u_{m\mathbf{k}}\rangle \tag{2.55}$$

where $\mathbf{U}^{\mathrm{dis}(\mathbf{k})}$ is a rectangular $N \times N^{(\mathbf{k})}_{\mathrm{win}}$ matrix. One minimize the gauge-independent spread Ω_{I} in terms of $\mathbf{U}^{\mathrm{dis}(\mathbf{k})}$ to get the disentangled Wannier functions[58]. After the Wannier functions are estabilished, one can get the overlap and the matrix elements for the Hamiltonian from the DFT calculations.

Chapter 3

Electronic Structure and Topological Character of A_2IrO_3 in the Weak-Interaction Limit

In this chapter, we consider the effect of the SOC on the electronic structure of the A_2IrO_3 compounds without taking into account the on-site Coulomb correlations. First we investigate the electronic structure without including the SOC, and from the Wannier function data we clarify various hopping channels between Ir t_{2g}-orbitals as well as the role of A-site cations and the trigonal crystal fields. Upon including the SOC, we illustrate the crossover from the quasi-molecular orbital scenario suggested by Mazin *et al.* and confirm that the $j_{\text{eff}} = 1/2$ states are dominant near the Fermi level. With that $j_{\text{eff}} = 1/2$ states we construct minimal effective Hamiltonians, which has similar structure with that suggest by Shitade *et al.*. Finally we discuss how

to drive this system to a topological insulator phase from our model Hamiltonian, and suggest a couple of ways to realize it in our first-principles calculations.

3.1 Introduction

The role of the spin-orbit coupling(the SOC) on the honeycomb lattice has been one of the most important subjects in the condensed matter physics the SOCiety, especially because of the suggestion of the quantum spin-Hall effect(QSHE) on graphene[2, 3], which is the two-dimensional realization of the topological insulators with time-reversal symmetry[1]. Originally, Haldane suggested a model which shows a quantum Hall effect without external magnetic field[4], which is now termed a 'quantum anomalous Hall effect', on the honeycomb lattice. Haldane's suggestion was based on the assumption that, the alternating magnetic fluxes within the honeycomb lattice on a spineless electrons can generate complex next-nearest-neighbor hopping terms such that

$$\mathscr{H}_{\text{Haldane}} = t \sum_{\langle ij \rangle} c_i^\dagger c_j + it' \sum_{\langle\langle ij \rangle\rangle} \nu_{ij} c_i^\dagger c_j \tag{3.1}$$

where $\nu_{ij} = \pm$ if t' connects sites belonging to the A(B)-sublattice of the honeycomb. The imaginary term opens gap at the Dirac points and turns this system to an insulator characterized by an integer Chern number $C = 1$, which is the same *topological* invariant that characterize the integer quantum Hall systems. Such theoretically interesting yet highly artificial model

can hardly be realized in the realistic materials, but later Kane and Mele found that the time-reversal-symmetric analogue of Haldane's model can be realized with the help of the SOC. The so-called Kane-Mele(KM) model can be understood as a combination of two copies of the Haldane's model, each of them consisting of electrons with opposite spins, in a fashion that the resulting Hamiltonian conserves the time-reversal symmetry such that

$$\mathscr{H}_{\mathrm{KM}} = t \sum_{\langle ij \rangle \mu} c^{\dagger}_{i\mu} c_{j\mu} + it' \sum_{\langle\langle ij \rangle\rangle \mu\nu} \nu_{ij} c^{\dagger}_{i\mu} \sigma^{z}_{\mu\nu} c_{j\nu} \tag{3.2}$$

where σ^z is the z-component of the Pauli matrix for the spin and the greek letters are spin indices. The imaginary next-nearest-neighbor term it' in the Haldane model comes from the Aharanov-Bohm phase accumulated as an electron hops from one to another sites due to the artificial alternating fluxes within the honeycomb lattice, while the spin-dependent term $it'\tau^z$ in the KM-model arises from the atomic the SOC which acts on the electron as an '*effective magnetic fields*'. Although the magnitude of the SOC on graphene is found to be vanishingly small[5], another honeycomb lattices with strong the SOC such as Bismuth bilayers[6] can host KM-model. Because of the time-reversal symmetry Chern number vanishes in this model, but instead another topological quantity - the so-called Z_2-invariant is found to be non-trivial in the insulator phase. Like the Haldane's model the KM-model has a pair of well-defined chiral edge states, each of them having opposite spins and also with opposite velocity.

To realize such model on realistic materials, one needs nondegenerate orbitals with very strong the SOC on each atomic sites. Recent discoveries of

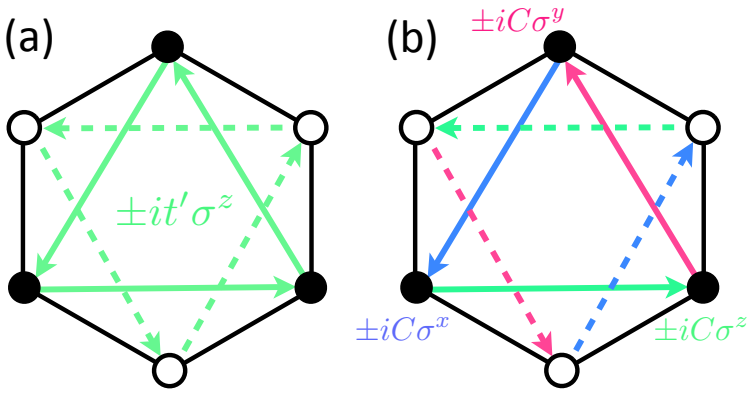

Figure 3.1: Complex hopping terms in (a) KM- and (b) SI-model. Green, purple and blue arrows correspond to hopping terms that couple to σ_x, σ_y, and σ_z, respectively. Solid and dashed lines are hoppings that connects sites belonging to A- and B-sublattices, respectively.

the '$j_{\text{eff}} = 1/2$' states on the layered perovskite iridate Sr_2IrO_4[38, 39] found that such states are realized in the iridium oxides with local cubic symmetry near the Ir-sites. When the SOC λ_{SO} dominates all over the other energy scales except the cubic crystal field Δ_{cubic} such that $\Delta_{\text{cubic}} \gg \lambda_{\text{SO}} \gg \Delta_{\text{others}}$, then the t_{2g} complex acts as effective $l_{\text{eff}} = 1$ and the resulting states are split into $j_{\text{eff}} = (l_{\text{eff}} = 1) \oplus (s = 1/2) = 1/2$ and $3/2$ complexes. As in the case Sr_2IrO_4, when there's five electrons occupied in the t_{2g} complex provided that the magnitude of the SOC is also larger than the strength of the hopping terms between the t_{2g} orbitals, then the low-energy physics of that system is characterized by the $j_{\text{eff}} = 1/2$ states. Assuming that the $j_{\text{eff}} = 1/2$-scenario is also valid in the case of Na_2IrO_3, Shitade *et al.* suggested a model Hamiltonian consisting of $j_{\text{eff}} = 1/2$ states on a honeycomb lattice. That sodium-iridate(SI) model has very similar structure with that of KM-model, except

that the next-nearest-neighbor hopping depends on the direction such that

$$\mathscr{H}_{\mathrm{SI}} = t \sum_{\langle ij\rangle\mu} d^{\dagger}_{i\mu} d_{j\mu} + \sum_{\langle\langle ij\rangle\rangle\mu\nu} t'_{ij\mu\nu} d^{\dagger}_{i\mu} d_{i\nu}, \tag{3.3}$$

where the next-nearest-neighbor term is

$$t'_{ij\mu\nu} = t'_0 \delta_{\mu\nu} + iC\sigma^a_{\mu\nu} \quad (a = x, y, z) \tag{3.4}$$

and a is determined by the direction of the hopping as illustrated in Fig. 3.1. The major difference between KM- and SI-model is, while KM-model conserves electron spin, or spin-orbit coupled pseudospin, SI-model mixes the Kramers doublet states as the electrons moves onto the lattice. Such difference is not significant in the weak-interaction limit where both model show the same QSHE, but upon inclusion of the on-site Coulomb correlations both model shows quite different behavior - especially SI-model shows a gapped phase without any order and also with fractional excitations[70, 68].

Contrary to the recent active theoretical studies on the suggested model Hamiltonians and experimental data on these materials, the number of studies based on first-principles calculations on these layered iridates are relatively small, which are crucial to understand the electronic structure on the realistic grounds. First DFT calculation results on Na_2IrO_3[41] captures some of the important features of the electronic structure, but the result is based on an artificial lattice structure with much smaller lattice constant. Recent work of Mazin *et al.*[73] provides detailed information about the bands of Na_2IrO_3, but according to our result they underestimate the impact of

the SOC on the t_{2g} complex. Up to the author's knowledge, for Li_2IrO_3 only the total energy calculation for different magnetic ground states[34] without detailed electronic structure analysis has been published.

In this chapter, we investigate the electronic properties of Na_2IrO_3 and Li_2IrO_3 from our DFT calculations, compare the difference of the two materials with DFT and Wannier function analysis, and construct the effective parameter-free model Hamiltonians of $j_{\text{eff}} = 1/2$ state. First, to understand the hopping structure between Ir t_{2g}-orbitals, without including the SOC we perform the calculations and clarify the major hopping channels that determines the band structures for both compounds. We compare the bands of Na_2IrO_3 and Li_2IrO_3 and discuss their difference in terms of the lr-Ir distance and also the role of *A*-site cations. It is found that, due to the smaller lattice size the overlap between neighboring Ir t_{2g}-orbitals in Li_2IrO_3 is larger than that of Na_2IrO_3, so yielding larger band dispersion in Li_2IrO_3. It is also found that, for both compounds *A*-cations acts only as sources of electron and Coulomb potential. As the SOC is included in the calculation we observe the crossover from the t_{2g} to the $j_{\text{eff}} = 1/2$ and $3/2$ states, and it also can be confirmed from the character of the constructed Wannier functions which consists of nearly perfect $j_{\text{eff}} = 1/2$ state at the centering Ir and small $j_{\text{eff}} = 3/2$ satellites at the three nearest-neighboring Ir sites. The resulting minimal effective Hamiltonian $\mathscr{H}_{\text{eff}}$ is, especially in the case of Li_2IrO_3, very close to the one suggested by Shitade *et al.* except significant third-nearest-neighbor hopping t_{n3} and interlayer coupling terms. We find that the phase transition from the topologically trivial phase to a three-dimensional topological insulator phase can be achieved as we tune the ratio between

the nearest- and third-nearest-neighbor terms t_{n3}/t_{n1} in the $\mathscr{H}_{\text{eff}}$. Since the nearest-neighbor term results from the competition between different hopping channels within the t_{2g} orbitals, it is quite susceptible to small amount of external perturbations and easy to be tuned. By using different kind of lattice strain we have realized the tuning the t_{n3}/t_{n1} in out DFT calculations.

3.2 Crystal structures

Before discussing our main results, let us first discuss about the structural properties of both compounds, and briefly explain about the unit cell adopted in this work. For Li_2IrO_3, there has been a couple of structure data for the polycrystalline samples[49, 50], and one of them claims *C2/c* unit cell[49] while the other one suggests that *C2/m* model gives the best fit to the x-ray diffraction data[50]. Both of the unit cell have qualitatively similar structure, but the *C2/m* unit cell has less distorted Ir honeycomb lattices and the mirror symmetry with respect to the plane perpendicular to the crystallographic $\mathbf{a}_2$-axis in Fig. 3.2(a). Starting from both of the experimental unit cells, our structure optimizations up to 10^{-4}Hartree/Åof force criterion yields the *C2/m*-compatible uni cell with nearly ideal honeycomb lattice of Ir atoms. Compared to the case of Li_2IrO_3 there has been several high-quality single crystal grown by a couple of groups[65, 66], and both of the samples agree that they have the *C2/m*-symmetry, correcting the previous result[33] showing more distorted *C2/m*-space group. Since the samples from independent studies shows only small quantitative differences, we use the structures in Ref. [65] without structural optimizations.

The in-plane lattice constant $\mathbf{a}_{1,2}$ are 5.427 and 5.1617Åfor Na_2IrO_3 and Li_2IrO_3, respectively. Contrary to the difference in the lattice constants, the distance between the Ir and oxygen atoms are nearly identical($\simeq$ 2.06Å) for both compounds as in Fig. 3.2.(d) and (e). For the lattice constants to be larger and yet the Ir-O bond lengths to remain rather unchanged, the upper and lower oxygen triangles should be rotated in opposite directions respectively also the $A_{1/3}Ir_{2/3}O_2$-layer should be compressed in the case of Na_2IrO_3. Such tendency can be seen by comparing the Ir-O bond angles within the IrO_6 octahedra for the both compounds as in Fig. 3.2.(d) and (e). The larger threefold distortion in Na_2IrO_3 gives slightly larger amount of trigonal crystal fields for Na_2IrO_3 as shown in later sections.

The crystal structure adopted for the calculations is *'minimal'* unit cells reduced from the original *C2/m* one, in which the in-plane Bravais lattice vectors are $\mathbf{a}_1$ and $\mathbf{a}_2$ in Fig. 3.2. (b). Due to the tilting of c-axis vector, which reflects the monoclinic stacking in theses compounds, the first Brillouin zone of our unit cell deviates from that of hexagonal unit cell as in the Fig. 3.2(c). The resulting Brillouin zone is distorted from that of hexagonal BZ, but we will still use the zone indices of hexagonal Brillouin zone at the 8 time-reversal-invariant-momenta(TRIM) for convenience.

3.3 Electronic structures without the SOC

Fig . 3.3(a) and (b) shows the electronic structure of Na_2IrO_3 and Li_2IrO_3 in the absence of the SOC. As it can be easily guessed from the local geometry near the Ir atoms, the *d*-complex of Ir is clearly split into t_{2g} and e_g complexes

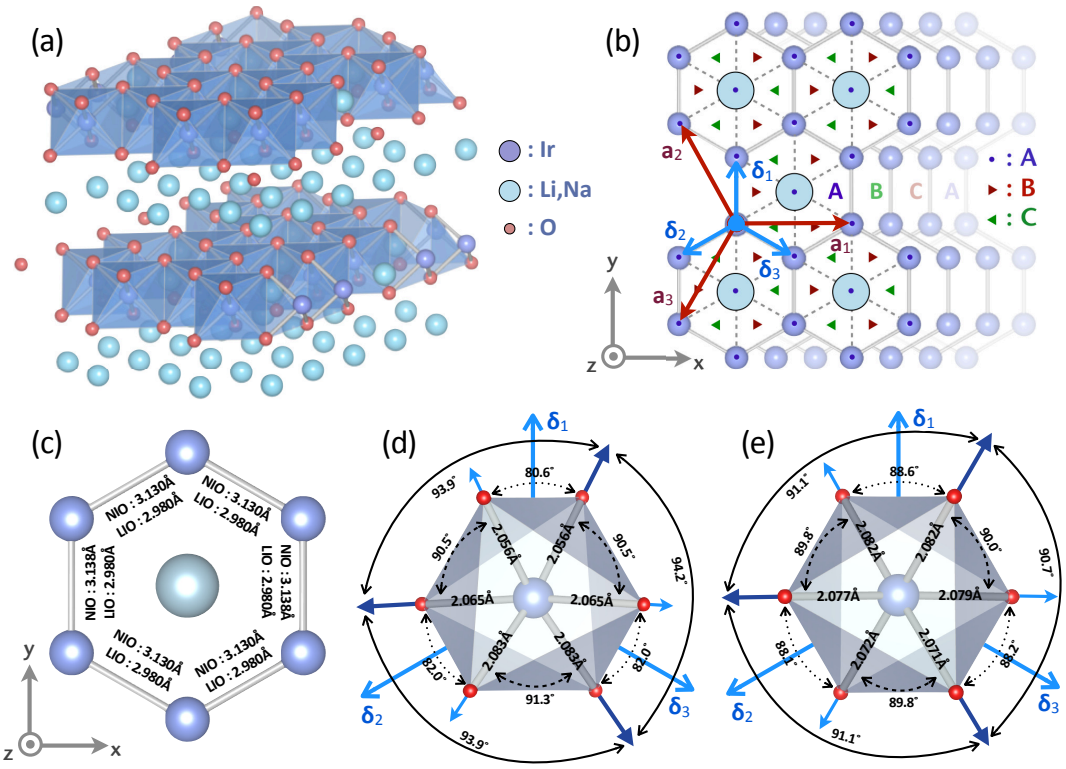

Figure 3.2: (a) Crystal structure of A_2IrO_3 compounds in which alternate stacking of A- and $A_{1/3}Ir_{2/3}O_2$-layers. (b) Schematic top view showing the monoclinic stacking of the $A_{1/3}Ir_{2/3}O_2$-layers along the z-axis, in which the three inequivalent positions for the stacking of the triangular layers A, B, and C is marked as blue dot, red and green triangles, respectively. Vectors to the three nearest-neighboring Ir atoms $\delta_{1,2,3}$ and the next-nearest-neighbors $\mathbf{a}_{1,2,3}$ are illustrated as blue and red arrow, respectively. (c) Bond lengths between nearest-neighboring Ir atoms for Na_2IrO_3 and Li_2IrO_3. Ir-O bond lengths and the O-Ir-O bond angles for (d) Na_2IrO_3 and (e) Li_2IrO_3 are represented, showing the compression and the threefold rotation of IrO_6 octahedra.

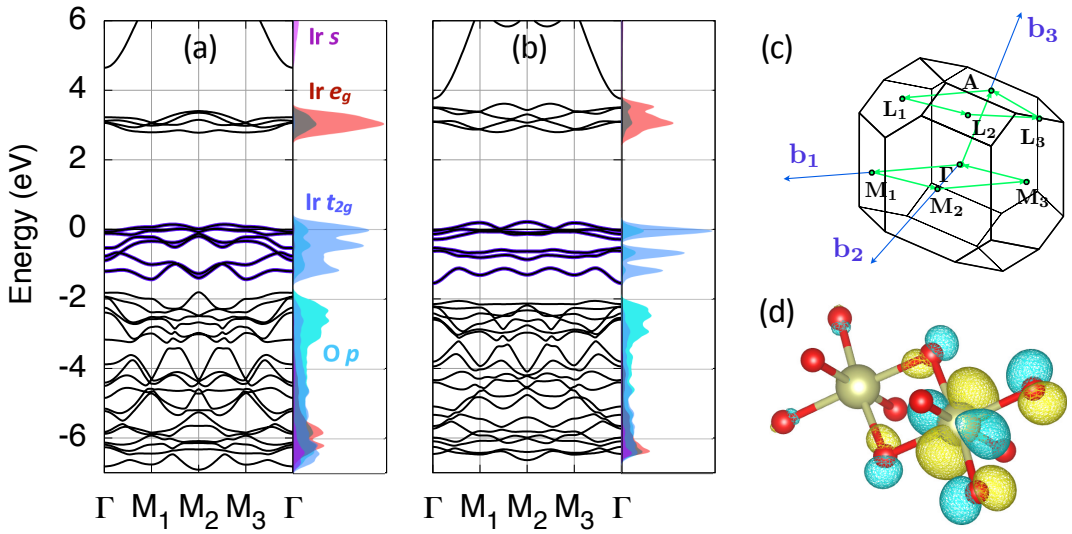

Figure 3.3: Band structure and projected density of states of (a) Li_2IrO_3 and (b) Na_2IrO_3, where the first Brillouin zone used in the calculations and its special k-points are shown in (c). For both bands, the blue-colored Wannier-interpolated bands for the t_{2g} orbitals are overlaid onto the bands from the DFT calculations. (d) shows one of the constructed t_{2g}-Wannier orbitals in which significant oxygen p-orbital components are mixed. Note the small($\lesssim$ 0.1eV) splitting of the e_g' doublet at the Γ-point.

for both compounds. Despite the 5% difference of the lattice constants between the two compounds, the magnitude of the splitting between t_{2g} and e_g is nearly same, reflecting the fact that that distance between Ir and O atoms are nearly same for both compounds. One can see that, the t_{2g} band of Na_2IrO_3 shows flatter dispersion than those of Li_2IrO_3, and the splitting of the t_{2g} complex into three peaks is much clearer. Mazin *et al.*[73] pointed that, such features are the manifestation of the formation of benzene-like quasi-molecular-orbitals(QMO) composed of Ir t_{2g} orbitals, with each orbitals consisting it connected to each other with the $dp\pi$-type hopping through intermediate oxygens as in Fig. 3.4.(a). From the hopping integrals between the t_{2g} Wannier orbitals, they found that the oxygen-mediated $dp\pi$-type hopping is dominant all over the other energy scales - three times larger than the second largest $dpd\sigma$-type hopping terms in Fig. 3.4.(b) in the case of Na_2IrO_3. Consequently, nearly flat bands of QMOs weakly coupled to each other occurs, as it can be seen from the band structure. To confirm their scenario and to check that such scenario also holds for Li_2IrO_3, we performed Wannier function calculations for the both compounds and classify major hopping paths between neighboring Ir atoms. It is found that, contrary to the case of Na_2IrO_3 where the well-localized QMOs are weakly coupled to each other, the strong direct σ-type hopping between the nearest-neighbor t_{2g}-orbitals yields larger band dispersion in Li_2IrO_3, so making the weakly-coupled QMO scenario inadequate in this case.

The character of the Wannier functions we construct depends on the energy range one choose, and in this chapter two different energy range have been used; -7$\sim$1eV from the Fermi level in which the t_{2g}- and the

p-complexes are fully included, and -1.8$\sim$1eV within which only the t_{2g}-complex is captured. The Wannier orbital constructed from the second choice contains contributions not only from the t_{2g}-orbitals but also from the p-orbitals of the neighboring oxygens as shown in Fig. 3.3.(c). Since the π-type overlap between the t_{2g}- and p-orbitals gives the strongest hopping path, as is in other oxide materials, the resulting Wannier orbitals has considerable amount of p-orbital components that overlaps with t_{2g}-orbitals in that way. From now on we name them $\{t_{2g}+p\}$-Wannier orbitals. The Wannier orbitals from the first energy range choice, within which the t_{2g}- and also the full p-complex, will be called '*Atomic*' Wannier functions.

Projecting the entire DFT Hamiltonian onto the $\{t_{2g}+p\}$-Wannier orbitals yields the six-band effective Hamiltonian which exactly reproduces the DFT band structure as in Fig. 3.3. The first column for the each directions in the Table 3.1 shows the major hopping terms for the six-band Hamiltonian. The second column shows the hopping integral between the t_{2g}-orbitals from the atomic Wannier functions, and one can say that they represent the hopping integral mostly from the direct hopping terms between Ir t_{2g}-orbitals. Subtracting the values of the second column from the first one gives the contributions from the oxygen-mediated process $\sim \frac{t_{pd}^2}{\epsilon_d - \epsilon_p}$. It should also be noted that, although the resulting Wannier orbitals are farely well-localized in the real space, still the overlap between themselves does not decay to zero up to the distance of $\sim$10Å, so it is hard to list up all of the nonzero terms.

Comparing the hopping terms of Na_2IrO_3 to those of Li_2IrO_3, one can notice the relation between the in-plane lattice constant *i.e.* distance between neighboring Ir atoms and the hopping integrals, especially the *dd*-direct

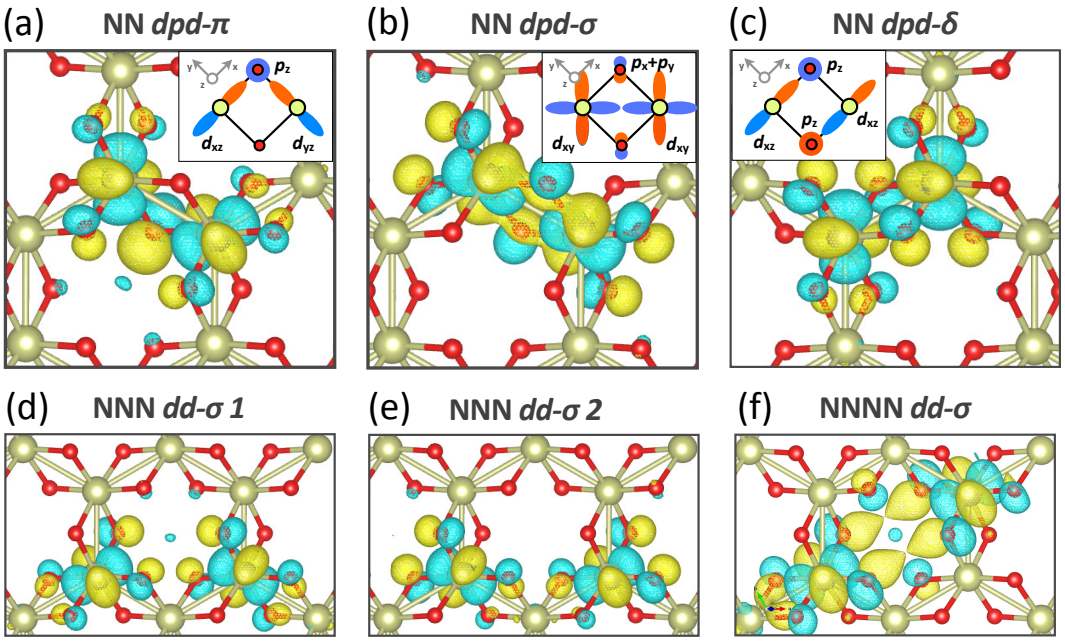

Figure 3.4: Overlap between the neighboring $\{t_{2g}+p\}$-Wannier functions of Na_2IrO_3, illustrating the most significant hopping paths in the A_2IrO_3-type compounds. (a) hopping through the $dp\pi$-type hopping between Ir to O. (b)hopping through the $dd\sigma$-type direct overlap between nearest-neighboring t_{2g} orbitals (c) the $dpd\delta$ type, where the insets provides schematics of the relevant orbitals. (d,e) the next-nearest-neighbor hopping terms where the direction of the neighboring t_{2g}-orbital robes (d) toward the A-cation and (e) the toward the intermediate Ir site.

			δ_1, $\mathbf{a}_1$			δ_2, $\mathbf{a}_2$			δ_3, $\mathbf{a}_3$		
			$\{t_{2g}+p\}$	Atomic	p-only	$\{t_{2g}+p\}$	Atomic	p-only	$\{t_{2g}+p\}$	Atomic	p-only
Na_2IrO_3	NN	dpd-π	0.285	-0.039	0.324	0.288	-0.047	0.335	0.287	-0.045	0.332
		dpd-σ	0.063	-0.346	0.409	0.023	-0.368	0.391	0.034	-0.359	0.393
		dpd-δ	0.031	0.130	-0.099	0.049	0.135	-0.086	0.043	0.132	-0.089
			0.023	0.130	-0.107	0.012	0.131	-0.119	0.013	0.128	-0.115
	NNN	dd-σ 1	-0.090	0.010	-0.100	-0.088	0.010	-0.098	-0.088	0.010	-0.098
		dd-σ 2	-0.036	0.010	-0.046	-0.043	0.010	-0.053	-0.045	0.010	-0.055
	NNNN	dd-σ	-0.022	-0.005	-0.017	-0.024	-0.005	-0.019	-0.024	-0.005	-0.019
Li_2IrO_3	NN	dpd-π	0.202	-0.113	0.315	0.216	-0.104	0.320	0.217	-0.105	0.322
		dpd-σ	-0.263	-0.603	0.340	-0.244	-0.591	0.347	-0.240	-0.590	0.350
		dpd-δ	0.097	0.183	-0.086	0.100	0.189	-0.089	0.096	0.186	-0.090
			0.090	0.177	-0.087	0.086	0.165	-0.079	0.088	0.168	-0.080
	NNN	dd-σ 1	-0.081	0.013	-0.094	-0.079	0.011	-0.090	-0.079	0.012	-0.091
		dd-σ 2	-0.049	0.015	-0.064	-0.048	0.014	-0.062	-0.048	0.014	-0.062
	NNNN	dd-σ	-0.025	-0.007	-0.018	-0.025	-0.007	-0.018	-0.024	-0.007	-0.017

Table 3.1: Major in-plane hopping integrals between the Ir $\{t_{2g}+p\}$- and atomic Wannier orbitals for Na_2IrO_3 and Li_2IrO_3. For each directions, the p-only components comes from the $\{t_{2g}+p\}$-components subtracted by the atomic Wannier function components. The notations for each terms are as shown in Fig. 3.4 and the directions in Fig. 3.2.

hopping terms. The most dramatic change comes from the $dpd-\sigma$ terms, which becomes the largest hopping term for the $\{t_{2g}+p\}$-Wannier orbitals in the case of Li_2IrO_3 and enhances the bandwidth of the Li_2IrO_3 compared to Na_2IrO_3 as shown in Fig. 3.3.(a). Such huge difference can be understood as the crossover from the oxygen-mediated to the direct hopping process between neighboring Ir t_{2g}-orbitals as the distance between the Ir atoms is reduced by $\sim$0.2Å, which can be checked directly from the contributions from the direct hopping of the dpd-σ terms. Note that, for nearest-neighbor terms of both compounds, the direct and the oxygen-mediated components tend to compete to each other, and that under lattice strain they behave in opposite way. Because of such feature, significantly large amount of change of the nearest-neighbor hopping terms can happen with rather small amount of strain, in case we deal effective models near the Fermi level. For the next-nearest- and third-nearest-neighbor terms, contrary to the previous speculations that the *s*-orbital components of the *A*-site cations are important in these long-ranged hopping integrals[41, 42], it is revealed that the oxygen-mediated process still does the major role for these terms. To be more specific, we calculate the bands and the hopping integrals with and without the in-plane *A*-cations for both compounds, and compare the bands as well as the hopping terms.

In the Fig. 3.5, the absence of the *A*-site cations does not affect the dispersions significantly. Rather, the role of the *A*-cations is the center of the Coulomb potentials that shift the on-site energies of the Ir and oxygen orbitals after they give up electrons to the oxygens. The shift of the potential energies becomes more significant as we remove the *A*-cations intercalated

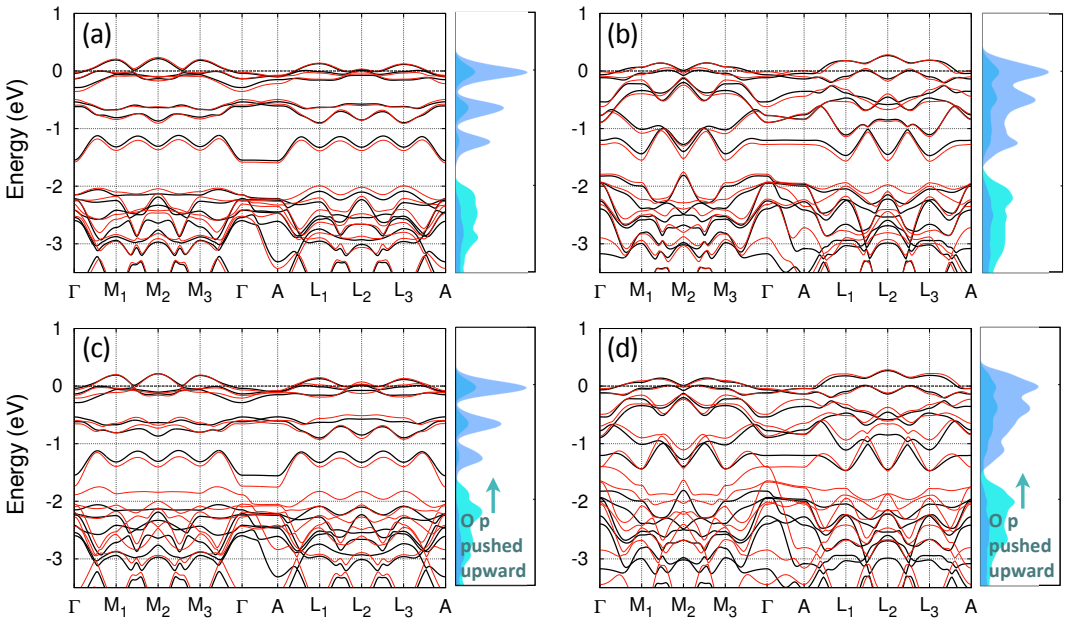

Figure 3.5: Bands and projected density of states of (a,c) Na_2IrO_3 and (b,d) Li_2IrO_3, where the orange curves are the bands without the *A*-site cations located (a,b) at the center of the Ir honeycomb and (c,d) between the two adjacent $A_{1/3}Ir_{2/3}O_2$ layers, while the bands from the original unit cell is inserted as guide for the eye. Note that the orange curves shows rigid shifts with respect to the black ones, which can be interpreted as shift of the orbital on-site energies.

		NNN dd-σ 1	NNNN dd-σ	$\varepsilon_{d_{xy}}$	ε_{p_z}	$\Delta\varepsilon_{dp}$
Na_2IrO_3	with Na	0.010	-0.005	2.436	1.543	0.893
	without Na	0.009	-0.003	1.731	1.074	0.657
Li_2IrO_3	with Li	0.013	-0.007	2.371	1.492	0.879
	without Li	0.013	-0.004	0.823	1.285	0.538

Table 3.2: Nearest- and next-nearest hopping terms, on-site energies of d_{xy}- and p_z-orbitals that couples to each other through π-type overlap, and the energy difference between them with and without the in-plane A-site cations locating on the center of the Ir honeycomb lattice.

between the $A_{1/3}Ir_{2/3}O_2$ layers, which are three times as many as the in-plane cations.

Further, let us compare the next- and the third-nearest-neighbor hopping terms to those from the calculation without A-cations. If the s-orbitals from the A-cations are involved in those terms, then the long-range hopping terms should be the ones that affected mostly by the presence or absence of the A-cations, and the values from the Table. 3.2 shows that it is not the case. Rather, it just shifts the on-site energies of the t_{2g} and p-orbitals, resulting the rigid band shifts in the Fig. 3.5.

Finally, we comment about the magnitude of the trigonal crystal fields, which comes from the contraction of the IrO_6 octahedra along one of the three-fold axis. The Hamiltonian for the on-site energies of the t_{2g}-orbitals is

$$\mathscr{H}_{\text{onsite}} = \begin{pmatrix} 0 & \Delta_a & \Delta_b \\ \Delta_a & 0 & \Delta_c \\ \Delta_b & \Delta_c & 0 \end{pmatrix} \tag{3.5}$$

where $\Delta_a = \Delta_b = \Delta_c = \frac{1}{3}\Delta_{\text{tri}}$ if the trigonal crystal symmetry presents. From the on-site energies of the $\{t_{2g}$+$p\}$- and the atomic Wannier orbitals one can directly get $\mathscr{H}_{\text{onsite}}$; $\Delta_a = \Delta_b = -0.017$eV and $\Delta_c = -0.014$eV for Na_2IrO_3, and $\Delta_a = -0.005$eV, $\Delta_b = -0.006$eV and $\Delta_c = -0.002$eV for Li_2IrO_3. The symmetry lowering due to the monoclinic stacking order of alternating $A_{1/3}Ir_{2/3}O_2$-layers is reflected on the unequal magnitude of the off-diagonal terms of the $\mathscr{H}_{\text{onsite}}$, but one can argue that the stronger three-fold contraction of the IrO_6 octahedra in Na_2IrO_3 yields three-times larger values compared to the case of Li_2IrO_3. In both compounds, the magnitude of $\Delta_{\text{try}} \sim 0.05$eV for Na_2IrO_3 and $0.01 \sim 0.02$eV for Li_2IrO_3, which are at least one order-of-magnitude smaller than other energy scales, especially smaller than the SOC.

3.4 Electronic structures with the SOC

In the situation that the trigonal crystal field Δ_{tri} is the dominant energy scale within the t_{2g}-complex, then the t_{2g} splits into a_{1g} and e'_g-doublets such that

$$|a_{1g}\rangle = \frac{1}{\sqrt{3}}\left(|d_{xy}\rangle + |d_{xz}\rangle + |d_{yz}\rangle\right) \tag{3.6}$$

$$|e'_{g,\pm}\rangle = \frac{1}{\sqrt{3}}\left(|d_{xy}\rangle + e^{\pm i\theta}|d_{xz}\rangle + e^{\mp i\theta}|d_{yz}\rangle\right) \tag{3.7}$$

where $\theta = 2\pi/3$. Hosub *et al.*[41] pointed that, when Δ_{tri} is much stronger than the SOC so that the bands near the Fermi level are dominated by the e'_g, then the SOC acts on the e'_g-doublets as an effective Zeeman field such

that

$$\langle \mathscr{H}_{\mathrm{SO}} \rangle_{e'_g} = \langle \lambda_0 \mathbf{L} \cdot \mathbf{S} \rangle_{e'_g} = \frac{\lambda_0}{2} \left(\begin{array}{c|c} \hat{n} \cdot \sigma & \\ \hline & -\hat{n} \cdot \sigma \end{array} \right), \tag{3.8}$$

where $\hat{n}$ is along the threefold axis, which are perpendicular to the Ir honeycomb plane in out case. Even though the magnitude of Δ_{tri} is found to be insignificant in the $A_2\mathrm{IrO}_3$ compounds, the $dpd\pi$-hopping terms between the t_{2g} orbitals that has quasi-threefold symmetry induces a_{1g} and e'_g states[73], as it can be seen in the first column of Fig. 3.6 where one can check clear splitting at Γ-point. As we tune the strength of the SOC from zero to half of the natural strength of the SOC of Ir($\frac{1}{2}\lambda_0$), the SOC just splits the e'_g-doublets without changing the character of the states at Γ.

The situation changes as the SOC is increased beyond $\frac{1}{2}\lambda_0$ where one of the a_{1g} character diffuses across the entire t_{2g} complex and the a_{1g}-e'_g characterization becomes invalid. Instead, the separation between the $j_{\mathrm{eff}} = 1/2$ and $3/2$ becomes clearer as the SOC grows beyond $\frac{1}{2}\lambda_0$, and at $\lambda_{\mathrm{SO}} = \lambda_0$ the average weight of the $j_{\mathrm{eff}} = 1/2$ component of the bands just above/below the Fermi level is about 78% for both compounds. Doubling the SOC enhances the splitting, but does not yields qualitative changes in the character of the bands as shown in the fourth column of Fig. 3.6. Our results, both the insignificant amount of the trigonal crystal field and the manifestation of the $j_{\mathrm{eff}} = 1/2$ states near the Fermi level, is the also consistent with recent RIXS[46], ARPES[47], and optical data data[48].

To confirm the $j_{\mathrm{eff}} = 1/2$-ness of the states near the Fermi level, we construct Wannier orbitals for the $j_{\mathrm{eff}} = 1/2$-like bands. By choosing the energy range in which the $j_{\mathrm{eff}} = 1/2$-dominated bands are captured, we can con-

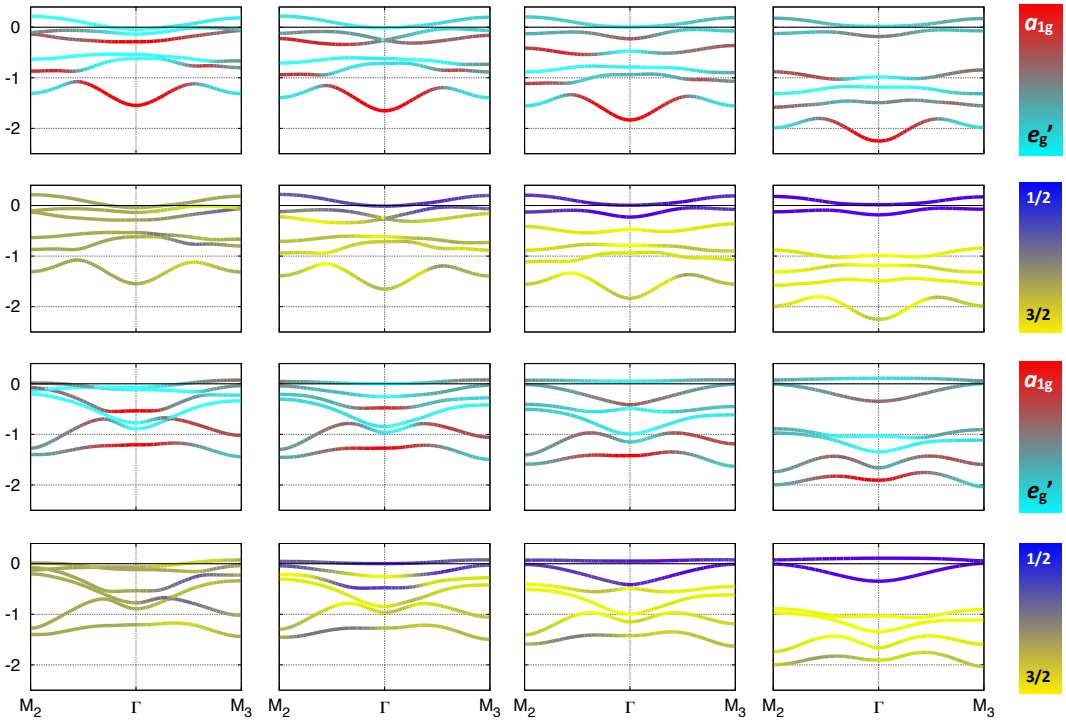

Figure 3.6: Bands of t_{2g} orbitals of Na_2IrO_3(first and second rows) and Li_2IrO_3(third and fourth rows) with the SOC strength $\lambda_{SO} = 0$(first column), $\frac{1}{2}\lambda_0$(second column), λ_0(third column), and $2\lambda_0$(last column), where $\lambda_0 = 0.4eV$ is the natural the SOC strength of the Ir atom. The first and third rows shows a_{1g}-e'_g weights of the bands, while the second and fourth rows shows the $j_{\text{eff}} = 1/2$ and $3/2$ weights. Note that, all of the states are doubly degenerate due to the time-reversal and inversion symmetry.

	Na_2IrO_3		Li_2IrO_3	
	$j_{\text{eff}} = 1/2$	$j_{\text{eff}} = 3/2$	$j_{\text{eff}} = 1/2$	$j_{\text{eff}} = 3/2$
Site 0	0.783	0.004	0.780	0.013
Site 1	0.000	0.068	0.001	0.068
Site 2	0.000	0.070	0.001	0.070
Site 3	0.001	0.073	0.001	0.068

Table 3.3: Weights of the $j_{\text{eff}} = 1/2$ and $3/2$ components of the $j_{\text{eff}} = 1/2$-Wannier orbitals on the center site(Site 0) and its nearest-neighboring sites(Site 1-3).

struct four Wannier orbitals, the minimum basis set that is allowed by the inversion and the time-reversal symmetry such that

$$\mathscr{T}|W_{\mu=\pm}\rangle = |W_{\mu=\mp}\rangle \tag{3.9}$$

$$\mathscr{P}|W_{a=\text{AB}}\rangle = |W_{a=\text{BA}}\rangle \tag{3.10}$$

where the $\mathscr{T}$, $\mathscr{P}$, μ, and a are the time-reversal operator, the inversion operator with respect to the center of the two neighboring Ir sites, the pseudospin index for the $j_{\text{eff}} = 1/2$ doublet, and the sublattice index inside the honeycomb lattice, respectively. From now on, they will be called as '$j_{\text{eff}} = 1/2$-Wannier orbitals' for the rest of this work. Four different trial orbitals , d_{xy}, d_{xz}, d_{yz} and $d_{3z^2-r^2}$, were used as the initial projectors for the Bloch states, and all of the trial orbitals yields the same $j_{\text{eff}} = 1/2$-Wannier orbitals represented in Fig. 3.7 and Table 3.3. Each Wannier orbitals has its own partner connected by the inversion and time reversal symmetry operations .

Unlike the $\{t_{2g}+p\}$- or atomic Wannier functions, the $j_{\text{eff}} = 1/2$-Wannier

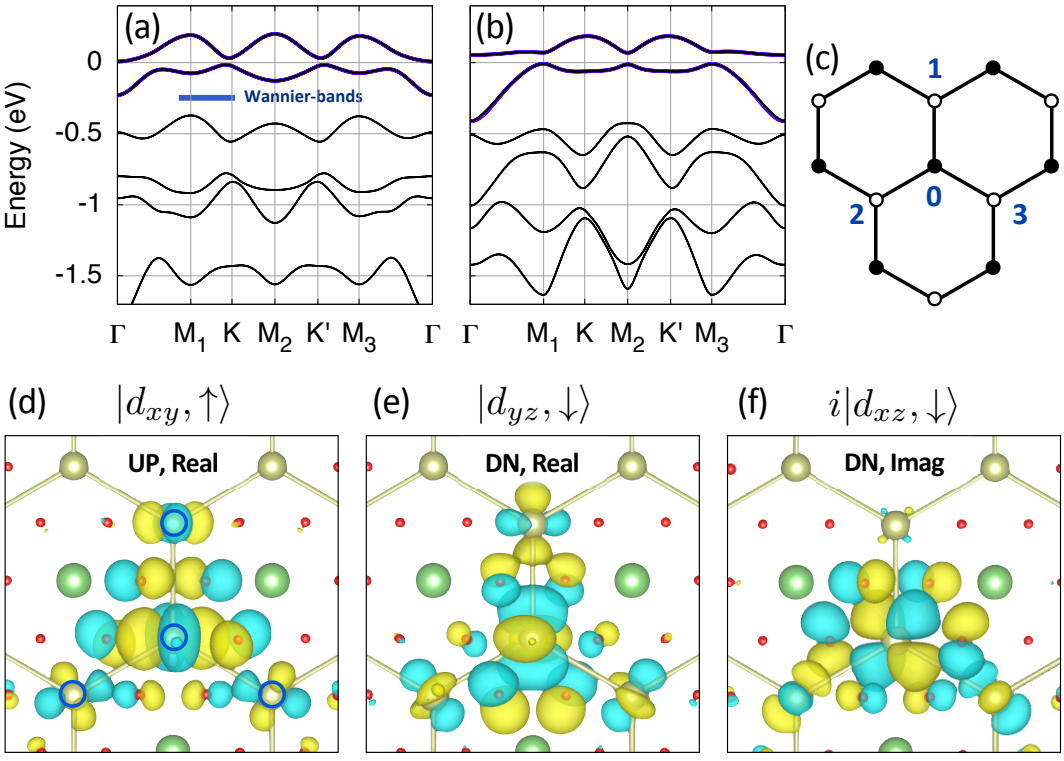

Figure 3.7: The bands of (a) Na_2IrO_3 and (b) Li_2IrO_3 with the SOC plotted in black line overlaid with the thick blue curves representing the Wannier-downfolded bands. (c) About $\sim$80% of the weight of the constructed $j_{\text{eff}} = 1/2$ Wannier orbitals is centered at site 0 and the rest $\sim$20% is spread evenly along its neighboring sites 1,2, and 3. The components on the center site is mostly $j_{\text{eff}} = 1/2$ states with its (d) spin-up real part, (e) spin-down real part, and (f) the spin-down imaginary part are shown.

orbitals are quite delocalized, where 20% of its components are spread along its three nearest-neighboring Ir sites as shown in Fig. 3.7.(c-e). The components on the center Ir site are mostly $j_{\text{eff}} = 1/2$ as shown in Table 3.3, while on the neighboring sites $j_{\text{eff}} = 3/2$ character is dominant. The dominance of the $j_{\text{eff}} = 1/2$ states at the center sites can be understood as the result of the negligible on-site energy terms except the SOC. The $j_{\text{eff}} = 3/2$ satellites are the natural consequence of the dominant $dpd\pi$-type hopping terms, which enforces the coupling between the neighboring $j_{\text{eff}} = 1/2$ to be zero as is pointed out in the work of Shitade *et al.*[7]. Interestingly, even in the presence of the much stronger $dpd\sigma$-type nearest-neighbor hopping terms in Li_2IrO_3, the character of the $j_{\text{eff}} = 1/2$-Wannier orbitals in both compounds looks almost identical, but we will not pursue that point further in this work.

3.5 Effective Hamiltonian for the $j_{\text{eff}} = 1/2$-Wannier orbitals

Due to the honeycomb-like Ir network, one can naively expect these layered iridates to have graphene-like effective Hamiltonian for the $j_{\text{eff}} = 1/2$ complex, but the actual situation is found to be quite different from those of graphene due to the presence of the long-ranged hopping terms and also

the complexity of our basis. The constructed model Hamiltonian looks like,

$$\begin{aligned}\mathscr{H}_{\text{eff}} &\simeq \sum_{\langle i,j\rangle\mu} t_{n1}^{\mathbf{r}_{ij}} \hat{c}_{i\mu}^{\dagger}\hat{c}_{j\mu} + \sum_{\langle\langle i,j\rangle\rangle\mu\nu} t_{n2;\mu\nu}^{\mathbf{r}_{ij}} \hat{c}_{i\mu}^{\dagger}\hat{c}_{j\nu} \\ &+ t_{n3} \sum_{\langle\langle\langle i,j\rangle\rangle\rangle\mu} \hat{c}_{i\mu}^{\dagger}\hat{c}_{j\nu} + \mathscr{H}_{interlayer}, \end{aligned} \tag{3.11}$$

in which the hopping terms can be represented in terms of the Pauli matrices such as

$$t_{\mu\nu}^{\mathbf{r}_{ij}} = C_{\mathbf{r}_{ij}}^{0}\delta_{\mu\nu} + i\mathbf{C}_{\mathbf{r}_{ij}}\cdot\sigma_{\mu\nu}, \tag{3.12}$$

where σ is the vector of Pauli matrices, the real vector $\mathbf{C} = (C^x, C^y, C^z)$, $\mu, \nu = \pm$ represents our Wannier doublets $|W_{\sigma=\pm}\rangle$, and $\mathbf{r}_{ij}$ means position vector between site i and j. Major hopping parameters are illusterated in Fig.3.8 and part of their values are in Table 3.4, while the list of other more detailed values of the hopping terms are in the Appendix.

From the values in Table 3.4, one can see that there are several unusual features in our hopping parameters. First, the next-nearest-neighbor term t_{n2} and third-nearest-neighbor hopping term t_{n3} are stronger than nearest-neighbor hopping term t_{n1}. In both cases the small values of the nearest-neighbor terms between the $j_{\text{eff}} = 1/2$-Wannier orbitals, compared to those from the $\{t_{2g}$+$p\}$- or atomic Wannier orbitals in Table 3.1, reflect the flat dispersions within the $j_{\text{eff}} = 1/2$-complex induced by the SOC. Especially, it is remarkable that t_{n1} in both compounds reduce by one order-of-magnitude, which is due to the delicate cancellation between various hopping channels within the t_{2g}-manifolds. Such cancellation easily breaks down under small amount of perturbations such as in-plane strain as shown in the next

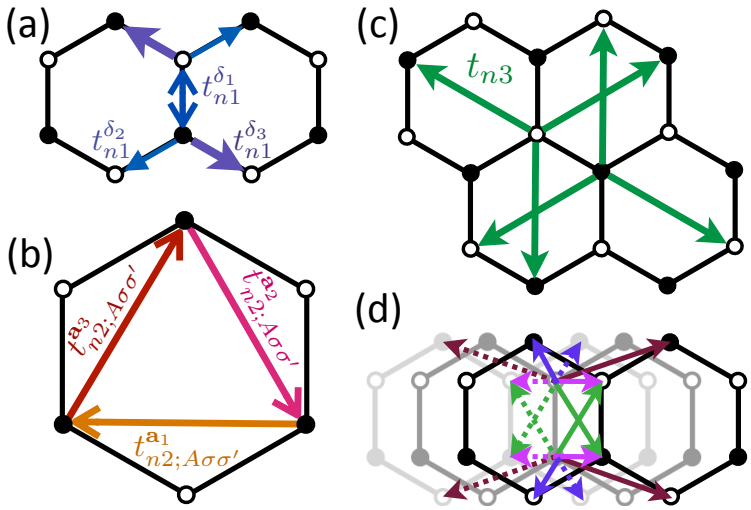

Figure 3.8: (Color online) Major hopping terms between the $j_{\text{eff}} = 1/2$-Wannier orbitals in both compounds, where the in-plane (a) nearest-neighbor, (b) next- and (c) third-nearest neighbor term and (d) inter-layer coupling terms are shown, whose values are in the Table. 3.4. The hopping terms with different character is represented as arrows with different shape and color.

	Na_2IrO_3				Li_2IrO_3			
	C^0	C^x	C^y	C^x	C^0	C^x	C^y	C^x
$t^{\delta_1}_{n1}$	13.1				-15.5			
$t^{\delta_2}_{n1}$	5.7				-6.0			
$t^{\delta_3}_{n1}$	7.4				-7.8			
$t^{\mathbf{a}_1}_{n2}$	-7.7	5.0	2.1	10.2	-18.7		1.6	-37.6
$t^{\mathbf{a}_2}_{n2}$	-6.2		-10.0	-3.9	-19.8	35.9		-4.7
$t^{\mathbf{a}_3}_{n2}$	-6.8	-3.1	-5.0	10.6	-19.3		35.7	5.9
t_{n3}	-40.3				-36.4			

Table 3.4: (in meV) Major hopping terms represented in Fig. 3.8 for Na_2IrO_3 and Li_2IrO_3 following the notations of (3.12), where the direction vectors for each hopping terms are in Fig. 3.2 and $\mathbf{a}_3 = -(\mathbf{a}_1 + \mathbf{a}_2)$. Hopping terms smaller than 1.0meV are left as blank.

section, and is less severe in t_{n2} where few numbers of the hopping channels are involved. Second, the nearest-neighbor hopping terms are highly anisotropic. It is due to the broken threefold symmetry originating from the monoclinic stacking of adjacent $A_{1/3}Ir_{2/3}O_2$-layers. still it affects the shape of constructed Wannier functions by distorting the IrO_6 octahedra. The effect of such anisotropy are amplified in the SOC-induced narrow top 4 bands, so yielding anisotropic t_{n1}. Third, due to the widespread $j_{\text{eff}} = 1/2$-Wannier orbitals the t_{n3} is enhanced compared to the those from the $\{t_{2g}+p\}$-Wannier orbitals. This t_{n3} term breaks the topological insulator phase of the SI-model and drives the system into a normal band insulator phase, as explained in the next section.

The last and the most interesting point is the nontrivial complex spin-dependent components **C** for t_{n2} of which values are in the Table. 3.4. Especially, in the case of Li_2IrO_3 the direction dependence is almost identical with the one proposed in [[7]] as is represented in Fig. 3.1.(b). Such **C**-vectors which mixes spin components, contrary to the KM-model where the pseudospin components are conserved, changes the nature of magnetic exchange interactions compared to the case of the KM-model[70]. It is remarkable that the magnitude of the **C**-vectors are weaker in Na_2IrO_3 compared to those in Li_2IrO_3. This is also reflected in the size of the gap m_K at the K and K'-points in Fig. 3.7.(a) and (b), which is easily found to be proportional to the magnitude of the **C**-vector such that $m_K = \frac{\sqrt{3}}{2}|\mathbf{C}_{\mathbf{a}_1} + \mathbf{C}_{\mathbf{a}_2} - \mathbf{C}_{\mathbf{a}_3}|$. The weaker magnitude of the t_{2n} and the unclear direction-dependence of the **C**-vectors in the case of Na_2IrO_3 are suspected to arise from the complexity of the Wannier orbitals and the competition between various hopping

channels, but we couldn't investigate them in detail in this work. Note that, the **C**-vector is null for the t_{2n} and t_{3n} for both compounds, since in these terms only the hopping integrals between same t_{2g}-orbitals are allowed so that complex or pseudospin-mixing hopping terms cannot occur in these cases.

3.6 Strain-induced topological insulator phases in Li_2IrO_3

As commented briefly in previous section, both Na_2IrO_3 and Li_2IrO_3 are just normal band insulators. In the presence of the inversion symmetry it can be checked conveniently by the parity analysis developed by Fu and Kane[61] where the Z_2-invariant $(\nu_0;\nu_1\nu_2\nu_3)$, which classifies the normal and topological insulators, is found to be the products of the parities of the occupied Bloch functions on time-reversal-invariant-momenta(TRIM) in the Brillouin zone such that

$$\begin{aligned} \delta_i &= \prod_{m=1}^{N} \xi_{2m}(\Gamma_i) \qquad (3.13) \\ (-1)^{\nu_0} &= \prod_{\{n_k\}=0,1} \delta_{i=(n_1n_2n_3)} \\ (-1)^{\nu_k} &= \prod_{n_k=1;\ n_{j\neq k}=0,1} \delta_{i=(n_1n_2n_3)}. \end{aligned}$$

Here, the eight TRIM $\Gamma_{i=(n_1n_2n_3)} \equiv \frac{n_1}{2}\mathbf{b}_1 + \frac{n_2}{2}\mathbf{b}_2 + \frac{n_3}{2}\mathbf{b}_3$ $(n_{1,2,3} = 0, 1)$ is the points on the three-dimensional Brillouin zone that satisfies the time-reversal-symmetry

	Γ	M_1	M_2	M_3	A	L_1	L_2	L_3	Z_2-inv.
Na_2IrO_3	-	-	-	-	-	-	-	-	(0;000)
Li_2IrO_3	-	-	-	-	-	-	-	-	(0;000)

Table 3.5: Parities of the unoccupied $j_{\text{eff}} = 1/2$ states on the eight TRIMs, and the resulting Z_2-invariants for Na_2IrO_3 and Li_2IrO_3. Parities are determined with respect to the center of the Ir hexagon.

condition such that $\Gamma_i = -\Gamma_i$, and $\xi_{2m}(\Gamma_i)$ is the parity of the *'half'* of occupied Bloch functions of relevant orbital complex where $\xi_{2m+1}(\Gamma_i)$ are the Kramers partners of each of the states. ν_0 is the *'strong'* index which tells us whether the system can have surface Dirac cones regardless direction of the surface, so that the system with $\nu_0 = 1$ is classified as a *'strong'* topological insulator(STI). The systems with $\nu_0 = 0$ but with nontrivial *'weak'* indices $\nu_{1,2,3}$, which are called as *'weak'* topological insulators(WTI), can also have surface Dirac cones depending on the direction of the surface[62].

Table 3.5 shows parities of the unoccupied $j_{\text{eff}} = 1/2$-Bloch states, since the products of the parities of the unoccupied orbital complex gives just same Z_2-invariant from the occupied complex. Unlike the SI-model, the Z_2-invariants for both compounds are just trivial as shown in Table 3.5. It is found that the third-nearest-neighbor hopping terms, which are absent in the SI-model, drives band inversion at the six $M_{1,2,3}$- and $L_{1,2,3}$-points. The gap at M-points are, only considering the in-plane hopping terms for sim-

plicity,

$$
\begin{aligned}
m_{\mathrm{M}_1\equiv\left(\frac{1}{2}00\right)} &= t_{n1}^{\delta_1} + t_{n1}^{\delta_3} - t_{n1}^{\delta_2} - t_{n3} \\
m_{\mathrm{M}_2\equiv\left(0\frac{1}{2}0\right)} &= t_{n1}^{\delta_2} + t_{n1}^{\delta_3} - t_{n1}^{\delta_1} - t_{n3} \\
m_{\mathrm{M}_3\equiv\left(\frac{\bar{1}}{2}\frac{1}{2}0\right)} &= t_{n1}^{\delta_1} + t_{n1}^{\delta_2} - t_{n1}^{\delta_3} - t_{n3}.
\end{aligned}
\tag{3.14}
$$

In the absence of t_{n3} and the inter-layer hopping terms the system is a WTI phase, since it is just a stacked two-dimensional QSH systems. When t_{n3} becomes larger than t_{n1} as in our cases, then the gaps at six $\mathrm{M}_{1,2,3}$- and $\mathrm{L}_{1,2,3}$-points close and reopen, changing the Z_2-invariant to be trivial.

By tuning the ratio between t_{n3} and t_{n1} we can drive the system back to the WTI phase, but in our $\mathscr{H}_{\mathrm{eff}}$ not only the intra-layer components but also inter-layer hopping terms exist, and the effective mass at the M- and L-points differ by the amount of the inter-layer components such that

$$
m_M \simeq t_{n1} - t_{n3} + \delta m_{\mathrm{interlayer}} \tag{3.15}
$$

$$
m_L \simeq t_{n1} - t_{n3} - \delta m_{\mathrm{interlayer}}. \tag{3.16}
$$

Because of these inter-layer terms, and also the anisotropy of t_{n1}, one can selectively achieve band inversion at a M-point we choose, and drive these layered iridates to be a STI.

As is stated in previous section, t_{n1} is easier to be changed than other hopping terms, and we have found a couple of ways how to tune it to achieve STI phase in the case of Li_2IrO_3. First we have found that, by changing the inter-layer distance as in Fig. 3.9 t_{n3}/t_{n1} can be tuned so that the transition to

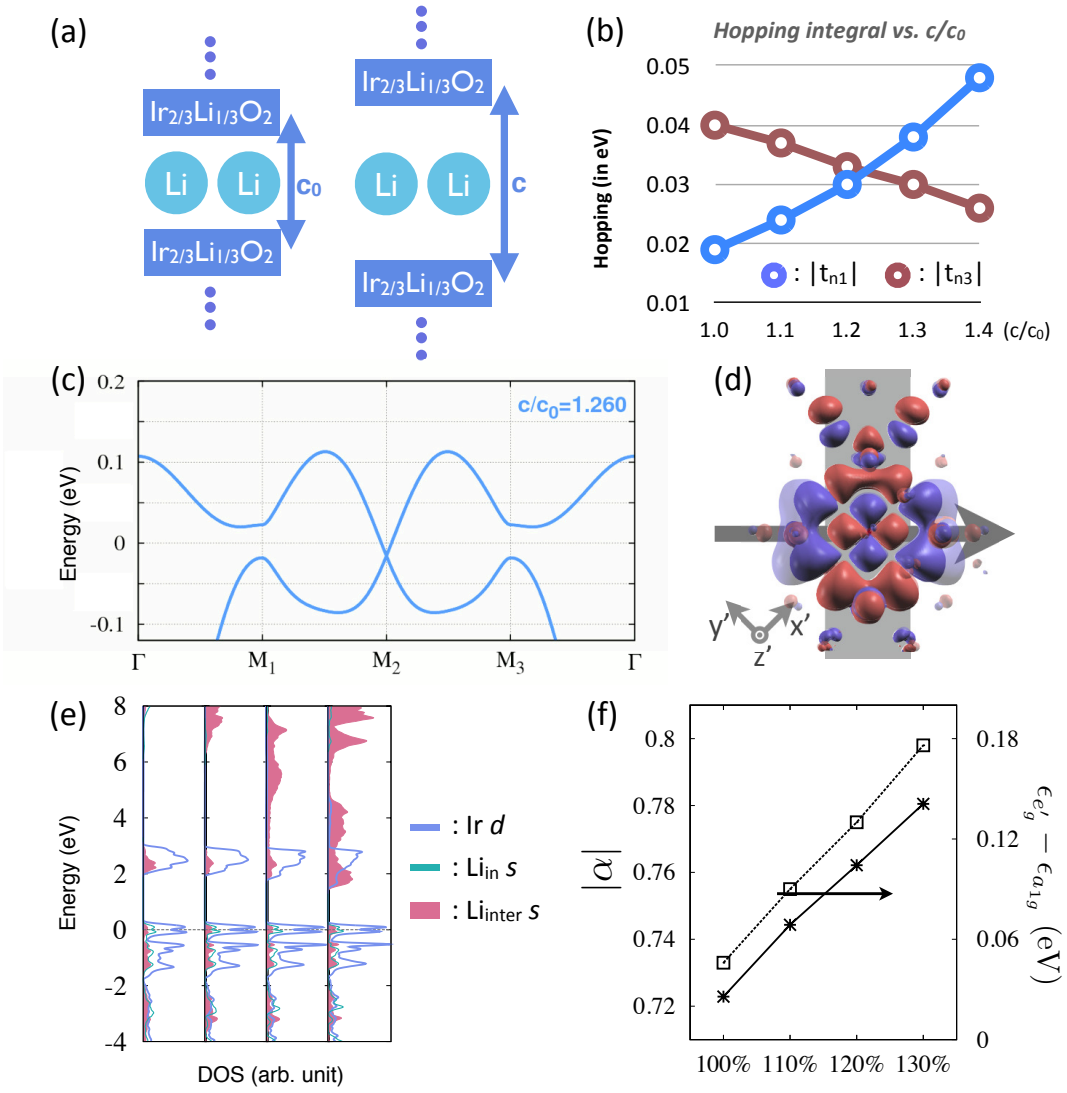

Figure 3.9: (a) Schematic side view of Li_2IrO_3 where the inter-layer distance c is increased from its equilibrium distance c_0. (b) The change of t_{n1} and t_{n3} in terms of the inter-layer distance, and (c) the band inversion at the M_2-point at $c/c_0 = 1.26$. (d) d_{xy} orbital from one of the $\{t_{2g}+p\}$-Wannier orbitals, where the solid and transparent surfaces are from the results of $c/c_0 = 1.0$ and 1.3, respectively, and the shaded arrow is along the out-of-plane direction. (e) The projected DOS of Ir d- and Li s-orbitals(10 times magnified) with increasing c/c_0 from 1.0 to 1.3. (f) Enhancement of the magnitude of the trigonal crystal field Δ_{tri} and the α in (3.18) in terms of the c/c_0-ratio.

the STI phase can be achieved. As the interlayer distance is increased up to 26%, the band inversion happens only at M_2-point, and the system changes into a STI with Z_2=(1;110). As the interlayer distance becomes large, the s-orbital components of the intercalated Li are mixed into the Ir t_{2g}-complex as shown in Fig. 3.9.(d) and (e), so extending the $\{t_{2g}+p\}$-Wannier orbitals along the out-of-plane direction. Such mixing of the s-orbital components affects the t_{n3}/t_{n1}-ratio by enhancing Δ_{tri} as in Fig. 3.9.(f). By rewriting our $j_{\text{eff}} = 1/2$-Wannier orbitals in terms of the a_{1g} and e'_g basis such that

$$\begin{aligned} |W_+\rangle &= \alpha|e'_{g+};\downarrow_{\mathbf{n}}\rangle + \beta|a_{1g};\uparrow_{\mathbf{n}}\rangle \\ |W_-\rangle &= \alpha|e'_{g-};\uparrow_{\mathbf{n}}\rangle + \beta|a_{1g};\downarrow_{\mathbf{n}}\rangle \end{aligned} \tag{3.17}$$

where α and β are complex numbers satisfying $|\alpha|^2 + |\beta|^2 = 1$ and $\mathbf{n}$ are along the out-of-plane direction. Note that $|e'_{g\pm}\rangle$ and $|a_{1g}\rangle$ are the eigenstate of the angular momentum operator $L_{\mathbf{n}}$ with eigenvalues ± 1 and 0, respectively. The nearest-neighbor hopping term can be written in terms of this expression such that

$$t_{n1} \simeq \frac{2|\alpha|^2 - |\beta|^2}{3} t_{dpd\pi} + \frac{1}{3}(t_{dpd\sigma} + 2t_{dpd\delta}) \tag{3.18}$$

where each nearest-neighbor hopping channels $t_{did\pi}$, $t_{did\sigma}$, and $t_{did\delta}$ are illustrated in Fig. 3.4. Since $t_{did\pi}$ is large, and also it is proportional to the difference of the square of α and β, small change of α can result in a large enhancement in t_{n1} as in this case. For the decreasing t_{n3}, the enlarged distance between the oxygen and Li cations yields reduced Coulomb potential

on the oxygen sites as in the case of the absent intercalating cations in the previous section. The reduced energy difference between Ir t_{2g}- and oxygen p-orbitals enhances the positive channel originating from the oxygen-mediated process which competes with the negative direct hopping process, so reducing overall t_{2n}.

Stretching the lattice by 30% along c-axis is highly unrealistic, since at that strain the lattice cannot sustain. To realize more realistic, and more intuitive strain in controlling the t_{n3}/t_{n1} ratio, we have tried uniaxial strain along $\mathbf{a}_1$ direction. Since the lattice distortion is not three-fold symmetric, the resulting band inversion only happens at M_2 point, changing the Z_2-invariant from (0;000) to (1;110) as illustrated in Fig. 3.10.(b-e). The nontrivial Z_2-invariant can be confirmed by drawing the single surface Dirac cone using the tight-binding parameters from the $\Delta a = 4\%$ unit cell, as shown in Fig. 3.10. It should be noted that the band inversion at M_2 point is assisted by the inter-plane hopping terms, so enabling sign change of effective mass (3.16) only at a/a_0 = 2%, which also makes this material to be a strong topological insulator.

3.7 Discussions

Considering the electronic structure of the transition metal oxides one should address the issue of correlation effect. Although the on-site correlation for the spatially extended 5d-orbitals are weaker than those of more localized 3d-orbitals, still it is reported that the magnitude of correlation on the 5d-complex is comparable to those of SOC[38, 46, 47, 48]. Also, the high-temperature

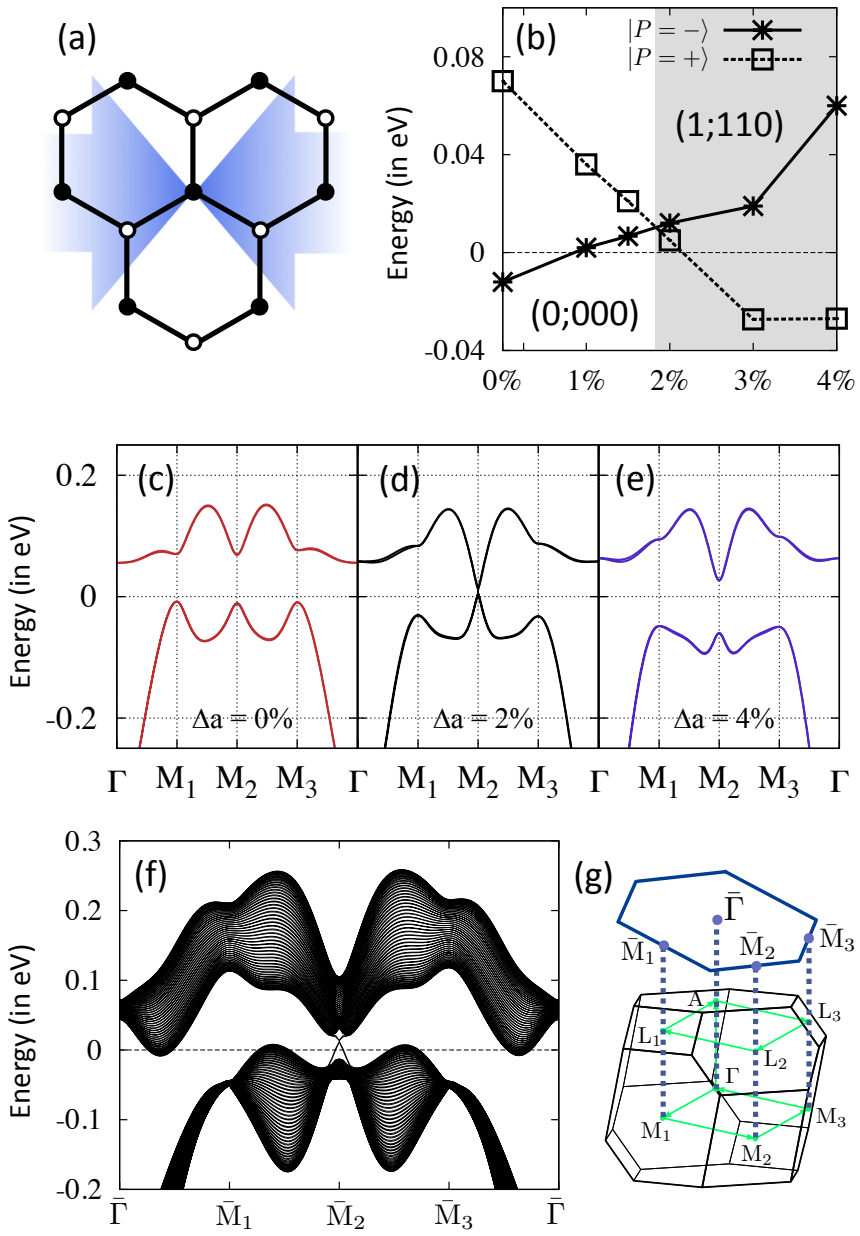

Figure 3.10: (a) The direction of the uniaxial strain to Li_2IrO_3 along the $\mathbf{a}_1$ direction. (b) The position of the lowest unoccupied and highest unoccupied $j_{\text{eff}} = 1/2$ states in terms of the strain, where the Z_2-invariant of the system turns into (1;110) at $\Delta\mathbf{a}_1 \simeq 2\%$. (c-e) Evolution of the $j_{\text{eff}} = 1/2$ bands as the strain is increased. (d) The surface state of from the slab of 50 Ir layers where the surface band indices are illustrated in (g).

Curie-Weiss tails are observed in Na_2IrO_3 and Li_2IrO_3[34], which implies localized moments at Ir sites in the high-temperature paramagnetic states. Although our band dispersions are flat to yields insulating or semimetallic ground states for both compounds, the nature of the ground states comes from the itinerant electrons characterized by delocalized Bloch states. In this case, one can question about the validity of the calculations without the on-site correlation effect, but still we can argue that, in the high temperature where the time-reversal symmetry is restored the character of the localized states should be similar to the occupied $j_{\text{eff}} = 1/2$-Wannier orbitals in our calculations. In the following chapter, from our calculation result we will check that the $j_{\text{eff}} = 1/2$ and $3/2$ character is robust even in the presence of the correlations in both compounds. Given that the $j_{\text{eff}} = 1/2$-character is robust, than we can apply the $\mathscr{H}_{\text{eff}}$ as a starting ground of the correlated systems, with some modifications such as the Hartree-like on-site energy.

The band structure of Li_2IrO_3 with the SOC is semimetallic, contrary to the case of Na_2IrO_3 which becomes insulating. Still, we have used the term 'topological *insulator*' in both cases to avoid unnecessary confusion with other nontrivial topological metallic phases such as recently suggested Weyl semimetal phase[64]. The semimetallic results for Li_2IrO_3 are in odd with recent experimental reports suggesting insulating behavior up to room temperature in this compound[34]. Such discrepancy might be originated from correlation effects, or from the significant amount of disorder in this material, which has been first reported by Singh and coworkers[33]. They also reported anomalous ρ-T behavior between 100K and 300K which they suspect to arise from disorder-induced carrier localization, implying that

the insulating phase above 100K might corresponds to our semimetallic bands. Detailed XRD analysis[65, 66] and also the first-principles calculation result[65] indicates that stacking faults are very easy to predominate in these materials. Since the inter-layer hopping terms are significant in understanding the low-energy sector of the band, it can be also suggested that, introducing stacking faults in our band calculation results may yield insulating ground state without the on-site correlation effect, or even disorder-induced topologically nontrivial state[67]. Such effect of stacking faults on the electronic structure in this system has not been investigated, and also can be important future subject.

Chapter 4

Effective Magnetic Interactions in the Strong-Interaction Limit

In this chapter, we consider the effect of the on-site Coulomb correlations on the A_2IrO_3 compounds in the presence of the SOC. First we check the robustness of the $j_{\text{eff}} = 1/2$ states, and discuss about the relation between the spatial shift of the $j_{\text{eff}} = 1/2$-Wannier orbitals and the magnetism. Next, from our DFT calculations we present the evolution of the ground states with respect to the increasing on-site correlations treated with GGA+U method. To understand the microscopic mechanism of the magnetism, we construct effective spin Hamiltonians of the $j_{\text{eff}} = 1/2$-pseudospin by means of perturbation theory, and discuss about the possible non-collinear magnetic ground states.

4.1 Introduction

The possible emergent phases resulting from the topological insulators with correlation effect, such as the topological Mott insulator[10] where the changeless spinon has well-defined surface states, or the fractional topological insulator phases on top of the topological band insulators[11], have been subjects for active researches in recent years. Especially the two-dimensional systems such as the so-called Kane-Mele-Hubbard(KMH) model, which is the KM-model with the Hubbard-type on-site correlations, has been studied in expectation of possible emerging phases originating from the strong quantum fluctuations that arise from the low-dimensionality. It has been found that, the model hosts a quantum spin-liquid phase at zero SOC beyond a critical correlation strength[8], an edge-Mott and bulk-topological insulator states with chiral spinon bands on the edge at finite SOC strength[9, 12]. Contrary to the case of KMH-model, it has been reported that the SI-model with the Hubbard term(SIH-model) hosts another nontrivial topological states with fourfold-degenerate fractional charge excitations at the bulk[70]. Comparing the two models, different spin structure for the noninteracting Hamiltonian changes the nature of the interacting ground states drastically, and it becomes crucial to precisely estimate the noninteracting Hamiltonian to determine the ground state of relevant materials.

Another way to approach the correlated states is to start from the effective spin Hamiltonian. The researches on the spin models of A_2IrO_3 have been active, since the suggestion of the so-called Heisenberg-Kitaev(HK) model on these compounds[29] which is the combination of the nearest-

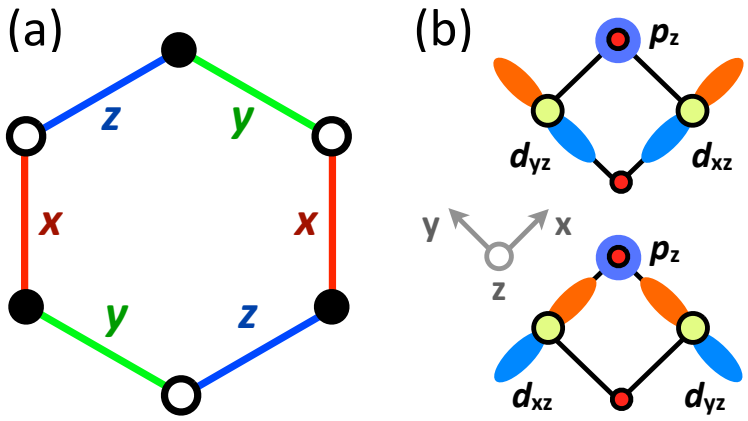

Figure 4.1: (a) Illustration of the nearest-neighbor γ-bonds in (4.1). (b) Two possible bondings between the neighboring t_{2g}-orbitals along the $\gamma = z$-bond.

neighbor Heisenberg model and the direction-dependent Ising interactions originally suggested in the Kitaev's exactly solvable model such that

$$\mathscr{H}_{\mathrm{HK}} = (1-\alpha)\sum_{\langle ij\rangle}\mathbf{S}_i\cdot\mathbf{S}_j - 2\alpha\sum_{\langle ij\rangle}^{\gamma-\mathrm{link}} S_i^{\gamma}S_j^{\gamma}, \quad (\gamma = x,y,z) \tag{4.1}$$

where γ represents three nearest-neighbor bonds between Ir sites as in Fig. 4.1. Note that the γ is determined by the direction of the p-orbital that is involved in the $dpd\pi$-bonding along the given nearest-neighbor bond direction[30]. Later, the HK-model has been expanded to include the next-nearest and the third-nearest-neighbor Heisenberg terms[35, 34] to stabilize the zigzag-antiferromagnetic order which are observed in recent neutron scattering experiments on Na_2IrO_3[65, 66].

The Kitaev term $S_i^{\gamma}S_j^{\gamma}$ has been derived considering the excited multiplet states induced by the Hund's coupling, since in the nearest-neighbor bonds only the trivial spin-independent hopping term survives. Recently a couple

of studies regarding the effect of the spin-dependent hopping terms on the spin Hamiltonian[68, 69] has been published, in which Kitaev-like exchange interactions between the next-nearest-neighbor spins arise from the spin-dependent hopping terms such that

$$\mathscr{H}_{\mathrm{SI-spin}} = -J_2 \sum_{\langle\langle ij \rangle\rangle} \mathbf{S}_i \cdot \mathbf{S}_j + 2J_2 \sum_{\langle\langle ij \rangle\rangle}^{\gamma-\mathrm{link}} S_i^{\gamma} S_j^{\gamma}. \tag{4.2}$$

In this case, the honeycomb lattice can be understood as weakly-coupled triangular lattices, and the ground states can be stripy or spiral order depending on the sign of the J_2-term and the magnitude of the nearest-neighbor terms.

The above $\mathscr{H}_{\mathrm{HK}}$ and $\mathscr{H}_{\mathrm{SI-spin}}$ arise from different physical origins, so we have to put them together to deal with the realistic systems. In that cases, increasing number of model parameters makes it hard for the theorists to explore and point the ground states within the multidimensional parameter space, and the help of first-principle calculations in determination of the reasonable parameters are crucial. With the DFT calculation and the parametrization provided by the Wannier function method, we have derived effective pseudospin Hamiltonian for the $j_{\mathrm{eff}} = 1/2$ states, which are found to be robust in the presence of the on-site correlation treated through the mean-field GGA+U method. First we present the phase diagram of Na_2IrO_3 and Li_2IrO_3 with respect to the increasing strength of the U-value from our DFT calculations. Analyzing the constructed Wannier orbitals with the finite U we find that the $j_{\mathrm{eff}} = 1/2$-character is robust, with some modifications on the spread and the position of the Wannier orbital

center depending on the magnetism. Interestingly, the $j_{\text{eff}} = 1/2$-Wannier orbitals show dimerization along the antiferromagnetic bonds in both compounds. After that, by applying perturbation theory to our $\mathscr{H}_{\text{eff}}$ we derive spin Hamiltonians for the $j_{\text{eff}} = 1/2$ pseudospins which includes Heigenberg, Kitaev-like terms, and also the Dzyaloshinskii-Moriya(DM) terms in the next-nearest-neighbor bonds. We combine our spin Hamiltonian with the original HK-model whose parameters are also estimated from our DFT calculations, and estimate the energies of several classical collinear ground states. We compare our results to those of recent theoretical works, and also comment briefly about the role of the DM terms.

4.2 Robustness of the $j_{\text{eff}} = 1/2$ states under the on-site Coulomb correlations

First, we discuss whether the $j_{\text{eff}} = 1/2$ character sustain when the correlation effect in taken into account, since the Coulomb repulsion favors integer occupations on each orbitals within the t_{2g}-complex. In the presence of the SOC, however, just widening the gap between the already separated $j_{\text{eff}} = 1/2$ states becomes energetically more favorable than mixing entire $j_{\text{eff}} = 1/2$ and $3/2$ complexes. The resulting robustness of $j_{\text{eff}} = 1/2$ states under correlation effect is reflected on the band structures in Fig. 4.2.(a) and (b), and also in the $j_{\text{eff}} = 1/2$-Wannier orbitals in Table. 4.1 and 4.2 for both compounds.

One can note that, the occupied $j_{\text{eff}} = 1/2$-Wannier orbitals $|W_{-}\rangle$ are widely

	Neel-AFM							FM
		$\|W_+\rangle$		$\|W_-\rangle$		$\|W_+\rangle$		$\|W_-\rangle$
	j_{eff}=1/2	j_{eff}=3/2	j_{eff}=1/2	j_{eff}=3/2	j_{eff}=1/2	j_{eff}=3/2	j_{eff}=1/2	j_{eff}=3/2
Site 0	0.874	0.005	0.701	0.006	0.817	0.010	0.765	0.006
Site 1	0.001	0.031	0.000	0.128	0.002	0.075	0.001	0.046
Site 2	0.000	0.043	0.000	0.079	0.000	0.045	0.001	0.089
Site 3	0.000	0.045	0.000	0.081	0.000	0.046	0.001	0.086
$\|\delta r\|$ (in Å)				0.17				0.20
Δr (in Å)		4.50		8.94		8.14		11.38
$\varepsilon_{\text{onsite}}$(in eV)		0.27		-0.27		0.10		-0.12

Table 4.1: The weights of the $j_{\text{eff}} = 1/2$ and $3/2$ components on the center (Site 0) and its nearest-neighboring sites (Site 1-3) of the $j_{\text{eff}} = 1/2$-Wannier orbital of Na_2IrO_3 from its Neel-antiferromagnetic(Neel-AFM) and ferromagnetic(FM) ground states, on-site energies of the empty($|W_+\rangle$) and occupied($|W_-\rangle$) $j_{\text{eff}} = 1/2$-Wannier doublets $|W_\pm\rangle$, the spread of the Wannier orbitals $\Delta r \equiv \langle r^2\rangle - \langle r\rangle^2$ and the magnitude of the center shift $|\delta r|$ of the occupied Wannier orbitals, where the direction of δr is in Fig. 4.2.(f).

	Neel-AFM							FM
		$\|W_+\rangle$		$\|W_-\rangle$		$\|W_+\rangle$		$\|W_-\rangle$
	j_{eff}=1/2	j_{eff}=3/2	j_{eff}=1/2	j_{eff}=3/2	j_{eff}=1/2	j_{eff}=3/2	j_{eff}=1/2	j_{eff}=3/2
Site 0	0.881	0.004	0.718	0.021	0.868	0.018	0.736	0.026
Site 1	0.000	0.030	0.109	0.002	0.000	0.040	0.000	0.017
Site 2	0.001	0.041	0.072	0.001	0.000	0.036	0.002	0.084
Site 3	0.001	0.041	0.069	0.001	0.000	0.035	0.002	0.085
$\|\delta r\|$ (in Å)				0.15				0.18
Δr (in Å)		4.36		7.78		4.37		8.14
$\varepsilon_{\text{onsite}}$(in eV)		0.22		-0.25		0.27		-0.25

Table 4.2: The weights of the $j_{\text{eff}} = 1/2$ and $3/2$ components on the center (Site 0) and its nearest-neighboring sites (Site 1-3) of the $j_{\text{eff}} = 1/2$-Wannier orbital of Li_2IrO_3 from its Neel-antiferromagnetic and ferromagnetic ground states, on-site energies of the empty and occupied $j_{\text{eff}} = 1/2$-Wannier doublets $|W_\pm\rangle$, the spread and the magnitude of the center shift of the occupied Wannier orbitals, where the direction of δr is in Fig. 4.2.(f).

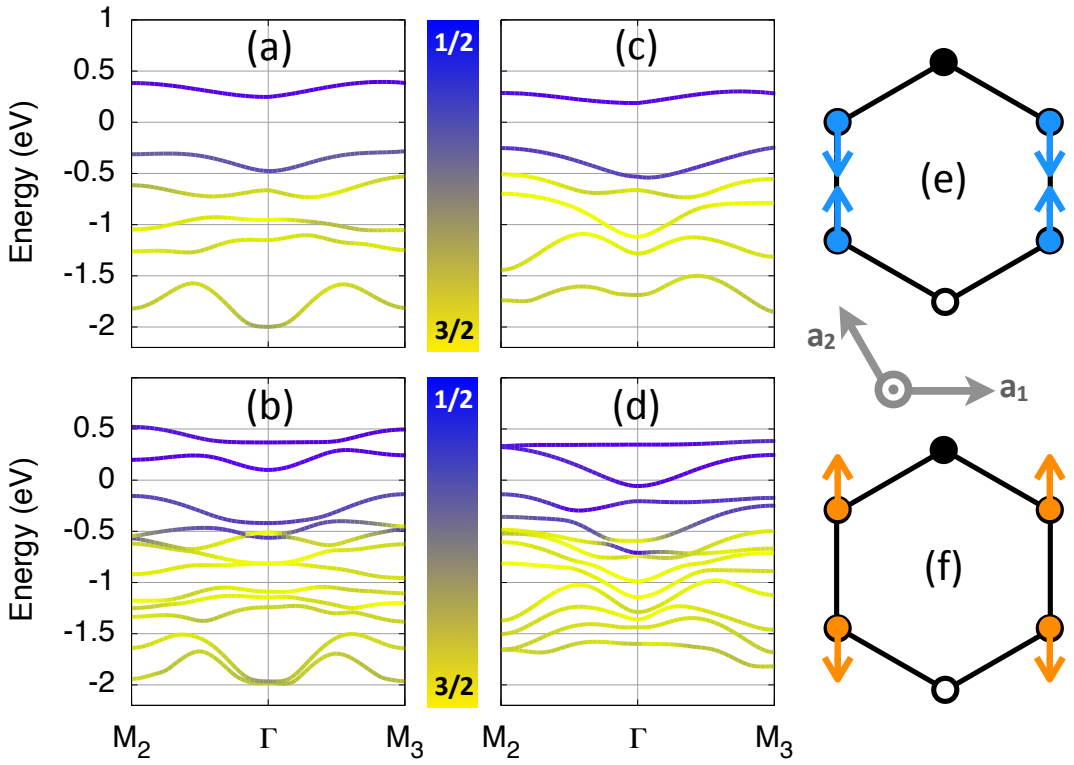

Figure 4.2: Bands of (a,b) Na_2IrO_3 and (c,d) Li_2IrO_3, where the bands in the upper row (a,c) are from the Neel-AFM ground state, while the ones in the lower row (b,d) are from the FM states, where in every bands $U = 1.5$eV has been used. (e) and (f) shows the shift of the center of the occupied $j_{\text{eff}} = 1/2$-Wannier orbitals of Neel-AF and FM ground states, respectively.

spread with stronger $j_{\text{eff}} = 3/2$-components around the nearest-neighboring sites. The anisotropy in the distributions of the $j_{\text{eff}} = 3/2$ satellite components is consistent with direction of the shift of the $j_{\text{eff}} = 1/2$-Wannier orbital centers, which favors AFM dimer formation and dislikes FM coupling by enlarging the distance between the Wannier orbitals. Considering only the nearest-neighbor hopping channel between the $j_{\text{eff}} = 1/2$-Wannier orbitals, the only allowed pseudospin interaction is the Heisenberg-type AFM interactions such that

$$J_{n1} \simeq -\frac{t_{n1}^2}{U}. \tag{4.3}$$

The energy gain from the exchange interactions can be lowered as the distance between neighboring $j_{\text{eff}} = 1/2$-Wannier orbitals are decreased in the Neel-AFM ground state, and vice versa for the FM state. Among the three nearest-neighbor bond directions, the shift of the Wannier orbital centers is along the δ_1-direction where the magnitude of the t_{n1} is strongest both Na_2IrO_3 and Li_2IrO_3 as shown in Table. 3.4. Finally, one can notice that the energy difference between the occupied and unoccupied Wannier orbitals are consistent with the strength of correlations of the iridate compounds estimated from the optical measurements[38, 47]. Although the value is smaller than the value $U_{t_{2g}} \sim$1.5eV used for the full t_{2g} complex in our first-principles calculations, the value for the $j_{\text{eff}} = 1/2$ complex $U_{j_{\text{eff}}=1/2}$ satisfies $U_{1/2} = \frac{1}{3}U_{t_{2g}}$ as the on-site Hartree mean-field interaction is projected onto the $j_{\text{eff}} = 1/2$ manifold, so becoming similar to the value observed in experiments.

4.3 Derivation of the pseudospin Hamiltonian

As briefly stated in the previous section, we can derive an effective pseudospin Hamiltonian from the $\mathscr{H}_{\text{eff}}$ through the perturbation theory. By applying the formalism which was used in the derivation of the $j_{\text{eff}} = 1/2$-pseudospin Hamiltonian for the hyperkagome system $Na_4Ir_3O_8$[53], we can get and effective Hamiltonian of the following form

$$\mathscr{H}_{\text{spin}} = \sum_{i,j} \left(J_{ij}\mathbf{S}_i \cdot \mathbf{S}_j + \mathbf{D}_{ij} \cdot (\mathbf{S}_i \times \mathbf{S}_j) + \mathbf{S}_i \cdot \hat{\Gamma}_{ij} \cdot \mathbf{S}_j \right), \tag{4.4}$$

where $\mathbf{S}$ means $j_{\text{eff}} = 1/2$ pseudospins, and the interaction terms are estimated as[53],

$$\begin{aligned} J_{ij} &= \frac{4}{U}\left(C^0_{ij}C^0_{ji} - \mathbf{C}_{ij} \cdot \mathbf{C}_{ji}\right) \\ \mathbf{D}_{ij} &= -\frac{4}{U}\left(C^0_{ji}\mathbf{C}_{ij} - C^0_{ij}\mathbf{C}_{ji}\right) \\ \hat{\Gamma}_{ij} &= \frac{4}{U}\left(\mathbf{C}_{ji}\mathbf{C}_{ij} + \mathbf{C}_{ij}\mathbf{C}_{ji}\right) \end{aligned} \tag{4.5}$$

provided that the hopping terms C^0 and $\mathbf{C}$ represented as in (3.12). Note that $\mathbf{C}^{ij} = (\mathbf{C}^{ji})^*$. All of the following values of exchange interactions are computed using the on-site correlation within the $j_{\text{eff}} = 1/2$ complex U=0.5eV.

In the Heisenberg term J in (4.5), AFM-contributions comes from the spin-independent hopping terms C^0, while the spin-dependent part $\mathbf{C}$ contributes to the ferromagnetic part. The Dzyaloshinskii-Moriya(DM) term and the anisotropic exchange tensor Γ only comes from the $\mathbf{C}$-vector, which originates directly from the SOC and only exist in the next-nearest-hopping

terms in both compounds as in Table 3.4. Note that, when neglecting the C^0-term for the next-nearest-neighbors, one get the spin Hamiltonian (4.2) with additional DM-terms which are absent in the previous works.

Above exchange interactions are from the hopping process between the $j_{\text{eff}} = 1/2$-Wannier orbitals. One also has to consider the hopping through the virtually excited multiplet states induced by the Hund's coupling which are considered in [30] where the interactions are

$$\Gamma_{n1}^{\prime ii} = -\frac{4t^2}{9U_{t_{2g}}}(\eta_1 + 2\eta_2), \tag{4.6}$$

where

$$\eta_1 = \frac{6J_{\text{H}}}{U_{t_{2g}} - 3J_{\text{H}}} \frac{U_{t_{2g}}}{U_{t_{2g}} - J_{\text{H}}} \tag{4.7}$$

$$\eta_2 = \frac{U_p}{\Delta_{pd} - U_p/2} \frac{U_p}{\Delta_{pd}} \tag{4.8}$$

$$\tag{4.9}$$

in which J_H is the Hund's coupling of Ir atom, Δ_{pd} is the energy difference between the Ir t_{2g}- and oxygen p-complexes, and $U_{t_{2g}}$ is the magnitude of the Coulomb correlation on the Ir t_{2g}-complex and U_p is the one for the oxygen p-complex. The value of $t \equiv t_{dpd\pi}$ are in Table 3.1. $U_{t_{2g}}$i is set to be 1.5eV and we set the value of U_p to be zero for simplicity. The list of the calculated exchange parameters are in Table 4.3 and the significant terms are illustrated in Fig. 4.3.

The characteristic features of the resulting pseudospin Hamiltonians directly follows from the form of the tight-binding Hamiltonian derived in

previous chapter, except the nearest-neighbor ferromagnetic Kitaev terms. Possibility for the existence of any other excited-state-mediated processes contributing to the nearest-neighbor Heisenberg terms is unknown to the authors, and we do not pursue that point in this thesis.

The smaller value of t_{n2} in $\mathscr{H}_{\text{eff}}$ in Na_2IrO_3 compared to Li_2IrO_3 is more strongly reflected on the next-nearest-neighbor exchange parameters J_{2n}, $\mathbf{D}_{2n}$, and Γ_{2n} because they are roughly proportional to the square of the hopping terms, while the nearest-neighbor Kitaev terms are stronger in Na_2IrO_3 due to the stronger $t_{dpd\pi}$ terms. The resulting spin model of Na_2IrO_3 can be understood as the HK-model with vanishingly small nearest- and next-nearest-neighbor Heisenberg terms. The model for Li_2IrO_3 is much more complex due to the presence of the next-nearest-neighbor DM and AF-Kitaev interactions. Searching for the ground states for these rather complex models are a demanding work, and instead in the next section we will compare and fit our model parameters for the both compounds to the results from the other theoretical studies.

4.4 Guessing out the magnetic ground state

In the case of Na_2IrO_3 where the next-nearest-neighbor $\mathbf{D}$ and Γ negligible, we can insert our parameters to the HK-model with additional second- and third-nearest-neighbor Heisenberg term such that

$$\mathscr{H}_{\text{HK}-J_2-J_3} = J\left[(1-\alpha)\left(\sum_{\langle ij\rangle} + J_2\sum_{\langle\langle ij\rangle\rangle} + J_3\sum_{\langle\langle\langle ij\rangle\rangle\rangle}\right)\mathbf{S}_i\cdot\mathbf{S}_j - 2\alpha\sum_{\langle ij\rangle}^{\gamma-\text{link}} S_i^\gamma S_j^\gamma\right], \tag{4.10}$$

		$\mathbf{r}$		$\delta_1, \mathbf{a}_1$			$\delta_2, \mathbf{a}_2$			$\delta_3, \mathbf{a}_3$	
		$i(jk)$	$x(yz)$	$y(xz)$	$z(xy)$	$x(yz)$	$y(xz)$	$z(xy)$	$x(yz)$	$y(xz)$	$z(xy)$
Na_2IrO_3	$n1$	$J_{\mathbf{r}}$		1.4			0.3			0.4	
		$\Gamma'^{ii}_{\mathbf{r}}$	0	0	Γ'^{ii}	Γ'^{ii}	0	0	0	Γ'^{ii}	0
	$n2$	$J_{\mathbf{r}}$		-0.6			-0.6			-0.8	
		$D_{\mathbf{r},i;A}$	-0.6	-0.3	-1.3	0	1.0	0.4	0.3	0.5	-1.2
		$\Gamma_{\mathbf{r},ii}$	0.4	0.1	1.7	0	1.6	0.2	0.2	0.4	1.8
		$\Gamma_{\mathbf{r},jk}$	0.3	0.8	0.2	0.6	0	0	-0.8	-0.5	0.2
	$n3$	$J_{\mathbf{r}}$		13.0			13.0			13.0	
Li_2IrO_3	$n1$	$J_{\mathbf{r}}$		2.1			0.3			0.5	
		$\Gamma'^{ii}_{\mathbf{r}}$	0	0	Γ'^{ii}	Γ'^{ii}	0	0	0	Γ'^{ii}	0
	$n2$	$J_{\mathbf{r}}$		-8.7			-7.4			-7.8	
		$D_{\mathbf{r},i;A}$	0	0	11.6	-11.5	-0.6	-1.6	0.3	10.9	-1.8
		$\Gamma_{\mathbf{r},ii}$	0	0	23.1	20.7	0.1	0.4	0	20.7	0.6
		$\Gamma_{\mathbf{r},jk}$	0.0	0.0	0.0	1.2	2.9	0.2	0.6	-0.1	0.6
	$n3$	$J_{\mathbf{r}}$		10.4			10.4			10.4	

Table 4.3: Values of the exchange interaction parameters (in meV) for Na_2IrO_3 and Li_2IrO_3 from both of the intra-$j_{\text{eff}} = 1/2$ contributions (4.5) and the $j_{\text{eff}} = 1/2$-$3/2$ contributions (4.6). $n1$, $n2$, and $n3$ represent nearest-, next-nearest-, and third-nearest-neighbors, respectively. Γ'^{ii} is about -25($\frac{6J_H}{1.5-3J_H}$ + 0.3) and -13($\frac{6J_H}{1.5-3J_H}$ + 0.3)meV for Na_2IrO_3 and Li_2IrO_3, respectively.

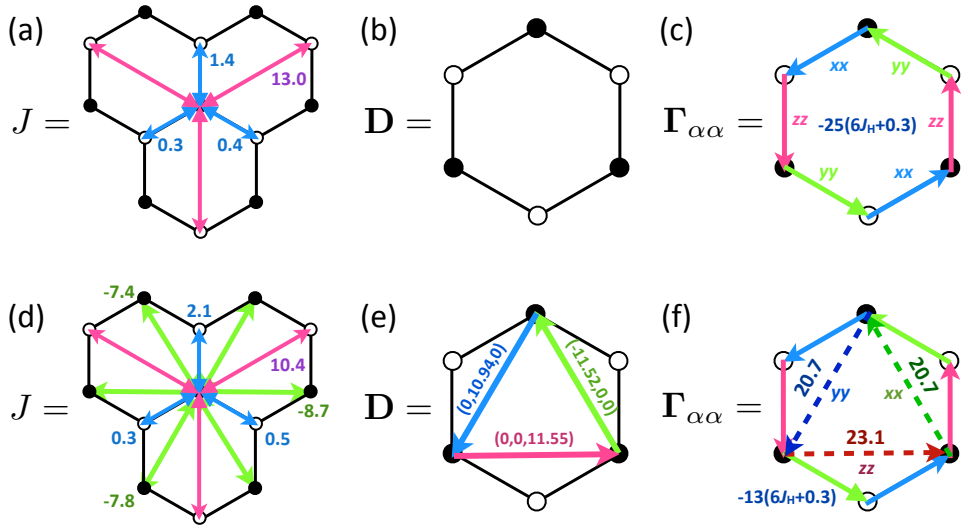

Figure 4.3: Illustrative representation of the pseudospin exchange parameters (a,d) J, (b,e) $\mathbf{D}$ and (c,f) Γ for (a-c) Na_2IrO_3 and (d-f) Li_2IrO_3, where only components with magnitude larger than 3meV are shown.

on which several theoretical analysis already has been done[35, 34] and will be called as HK-J_2-J_3-model in the following paragraphs. Our model can be simplified a little bit further as we ignore marginal terms such that

$$\mathscr{H}_{\mathrm{NIO}} \simeq J_{n3} \sum_{\langle\langle i,j \rangle\rangle} \mathbf{S}_i \cdot \mathbf{S}_j + K_{n1} \sum_{\langle i,j \rangle}^{\gamma-\mathrm{link}} S_i^{\gamma} S_j^{\gamma} \tag{4.11}$$

where $K_{n1} = \Gamma_{ii}$ for the corresponding γ-bonds. Although our model looks similar to the HK model except the third-nearest-neighbor Heisenberg terms instead of the nearest-neighbor ones, we cannot perform the simple analysis that yields stripy AF order at $-2J_{n1} = K_{n1}$ at the HK model[29]. Instead, we write down the classical spin energies for the four inequivalent collinear

magnetic orders for J_{n3} and K_{n1} such that

$$E_{\mathrm{FM}} = +\frac{3}{2}J_{1n} + \frac{3}{2}J_{3n} + \frac{1}{2}K_{1n} \tag{4.12}$$

$$E_{\mathrm{Neel}} = -\frac{3}{2}J_{1n} - \frac{3}{2}J_{3n} - \frac{1}{2}K_{1n} \tag{4.13}$$

$$E_{\mathrm{Stripy}} = -\frac{1}{2}J_{1n} + \frac{3}{2}J_{3n} + (\cos^2\theta - \sin^2\theta)\frac{1}{2}K_{1n} \tag{4.14}$$

$$E_{\mathrm{Zigzag}} = +\frac{1}{2}J_{1n} - \frac{3}{2}J_{3n} - (\cos^2\theta - \sin^2\theta)\frac{1}{2}K_{1n}, \tag{4.15}$$

where θ is the relative angle between the direction of the collinear spins and the local octahedral z'-axis. Note that, due to the Kitaev terms direction-dependence happens in the stripy and zigzag phases, which favors either θ=0 or $\pi/2$ depending on the sign. Comparing (4.13) and (4.14), we can see a phase transition from the Neel to the stripy phase at $\alpha = 1/3$ in the absence of J_{n3}. In the presence of J_{n3} with vanishing J_{n1}, from (4.15) one can check that the zigzag phase becomes the ground state, at least in the classical level.

We can also guess the ground states by comparing our model to the results of other theoretical analysis. Fitting our exchange parameters for Na_2IrO_3 yields $\alpha \sim 0.9$, $J_3 \sim 10$, with negligible contributions from the nearest- and next-nearest-neighbor Heisenberg interactions, the previous theoretical investigations on the model tell us that our set of parameters are located in the zigzag-AF order regime which is also the suggested ground state for this material[34, 35]. One can be tempted to conclude that, frustration is weak due to the absence of the next-nearest-neighbor Heisenberg terms in our model, which is in contrast to the large difference between the $T_N \approx$ 15K and the Curie-Weiss temperature $\theta_{\mathrm{CW}} \approx$ 125K[34]. Such large frustra-

tion owing to the competition between the nearest-neighbor ferromagnetic Kitaev term and the Heisenberg term may yield large frustrations in this system, which needs more elaborate future investigations.

In the case of Li_2IrO_3, things become much more complex due to the presence of the AFM-Kitaev terms of which magnitude comparable to those of the nearest-neighbor FM-Kitaev terms and the significant DM terms. It cannot be fitted to the framework of the HK-J_2-J_3-model used in Na_2IrO_3, yet a couple of works has been recently published to deal with the role of the next-nearest-neighbor AFM-Kitaev terms, such that the model has the form of

$$\mathscr{H}_{\mathrm{SI-spin}} = J_{n1} \sum_{\langle ij \rangle} \mathbf{S}_i \cdot \mathbf{S}_j + J_{n2} \sum_{\langle\langle ij \rangle\rangle} \mathbf{S}_i \cdot \mathbf{S}_j + K_{n2} \sum_{\langle\langle ij \rangle\rangle}^{\gamma-\mathrm{link}} S_i^{\gamma} S_j^{\gamma}. \tag{4.16}$$

where $K_{n2} \approx -2J_{n2}$[68, 69]. It has very similar form with our spin Hamiltonian for Li_2IrO_3, except the absence of J_{n3} and K_{n1} in the above one. When J_{n1} and K_{n1} becomes negligibly small compared to other exchange parameters in (4.16), then the system decouples into two independent triangular lattices, each of them favoring spiral spin order when $J_{2n} < 0$. Introducing $J_{n1} > 0$, which interconnects two interlacing sublattices, stabilizes the Neel AF order. In case of our model, the strong third-nearest-neighbor Heisenberg term may stabilize the zigzag AF order instead of the Neel phase as in the case of Na_2IrO_3, but the competition between the spiral and the zigzag or Neel phase should be investigated. Also, the role of K_{n1} on (4.16) should be understood.

As a zeroth-order approximation to the magnetic ground states, we have

calculated classical ground state energies of our model in arbitrary spin configuration. We adopted an 24-site spin cluster with satisfying a periodic boundary condition that makes the unit cell obey the periodicity of the spiral phase, which is the outcome of $\mathscr{H}_{\mathrm{SI-spin}}$ with $J_{n1}=0$ and $K_{n2}=-2J_{n2}$. For the energy optimization the optimize module within the SciPy package has been used[27]. Our result have found that, without J_{n3} our model favors spiral phase as predicted, and the DM term further stabilize it by reorienting the moments on the same sublattice to be perpenticular to each other. Introducing J_{n3} breaks the spiral phases, so that the zigzag phase become the ground state. Such tendency does not change as J_{H} is increased. It is possible that the DM terms invoke incommensurate spin canting onto the zigzag phase, which may be revealed in the calculations with larger supercell.

As the spiral order is found to be unstable, to understand the effect of each exchange interaction on the spin energy we estimate classical spin energy of some collinear configurations for Li_2IrO_3. The result is

$$E_{\mathrm{FM}} = +\frac{3}{2}J_{1n} + 3J_{2n} + \frac{3}{2}J_{3n} + \frac{1}{2}K_{1n} + K_{2n} \tag{4.17}$$

$$E_{\mathrm{Neel}} = -\frac{3}{2}J_{1n} + 3J_{2n} - \frac{3}{2}J_{3n} - \frac{1}{2}K_{1n} + K_{2n} \tag{4.18}$$

$$E_{\mathrm{Stripy}} = -\frac{1}{2}J_{1n} - J_{2n} + \frac{3}{2}J_{3n} + (\cos^2\theta - \sin^2\theta)\left(+\frac{1}{2}K_{1n} + K_{2n}\right) \tag{4.19}$$

$$E_{\mathrm{Zigzag}} = +\frac{1}{2}J_{1n} - J_{2n} - \frac{3}{2}J_{3n} + (\cos^2\theta - \sin^2\theta)\left(-\frac{1}{2}K_{1n} + K_{2n}\right) \tag{4.20}$$

where we have used $J_{1n}=1.0$, $J_{2n}=-8.0$, $J_{3n}=10.4$, $K_{1n}=\Gamma^{ii}_{1n}=-78J_H/(1.5-3J_H)$, and $K_{2n}=\Gamma^{ii}_{2n}=21\mathrm{meV}$ for Li_2IrO_3. We use the Hund's coupling J_H of Ir as a free parameter, and plot the energies as a functions of J_H in Fig. 4.4.(d).

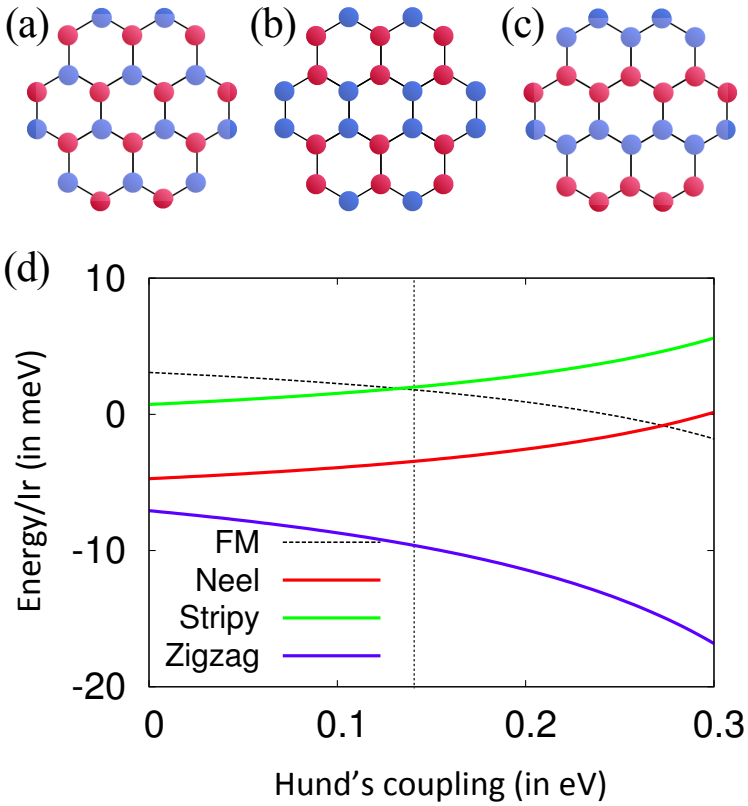

Figure 4.4: Schematic spin ordering of (a) Neel-AF, (b) stripy, and (c) zigzag configuration. (d) shows the energy per an Ir atom of each configurations (4.17-4.20) in terms of the Hund's coupling in the case of Li_2IrO_3.

The zigzag AF order becomes ground state over our range of J_H, and it becomes more stable as J_H increases. Unlike other theoretical analysis, in our model J_{n1} is negligibly small so that the Neel AF phase is hard to be stabilized. The large amount of K_{n2} enhances the tendency to the stripy and zigzag phase, but in stripy phase K_{n1} and K_{n2} competes each other to yield smaller energy gain, so that the energy of the zigzag phase becomes lowest. It should be noted that, there's no direct measurement for the magnitude of Hund's coupling, but recent constrained RPA calculations on Sr_2IrO_4 and Ba_2IrO_4 have estimated J_H to be about 0.15eV[71].

4.5 Phase diagram from the DFT calculations

Instead of guessing out the ground state from the spin model, we can directly calculate the magnetic ground states by comparing the total energy of the different magnetic configurations from the DFT calculations. There are 13 different magnetic configurations which are commensurate with the unit cell - paramagnetic phase, and the Neel, stripy, and zigzag phases with spin moments parallel to global x,y,z-axis. For each magnetic configurations, we performed DFT+SO+U calculations for both the LDA and GGA exchange-correlation functionals. For the DFT+U calculations Vienna Ab-initio Simulation Package(VASP) adopting the projector-augmented wave basis set has been used[28]. We have used two different DFT+U methodologies; the rotationally-invariant formalism in which the on-site correlation and the Hund's coupling terms are incorporated explicitly[20], and Dudarev's simplified formalism where only the on-site correlations are considered with

reduced effective magnitude $U_{\text{eff}} \equiv U - J$[21].

Table 4.4 shows the LDA+SO+U calculation results with simplified DFT+U formalism for both compounds. For Na_2IrO_3, one can see that the zigzag phase is stable over the range of U-value we have used. At U=0.0eV spin moments favors y-direction, but rotate to lie on the xz-plane. It is seen that the energy of the stripy phase becomes lower as the U increases while for the Neel phase vice versa. It is also noted that the energy for the x- and z-direction shows differences as U is increased beyond U=2.0eV. In the both of the stripy and zigzag configurations, the moments tend to favor the xz-plane at least by ≤ 0.5meV per an Ir atom, and such tendency is consistent with the moment directions estimated from recent neutron scatterings[66, 65]. Incorporating the effect of Hund's coupling does not change the situation in this case except some quantitative differences in the relative energies between the magnetic configurations and the magnitudes of spin moments, as shown in Table 4.5. The stability of the zigzag phase is consistent with recent other LDA+SO+U calculation results for this compound[34].

In the case of Li_2IrO_3, the rotationally-invariant and the simplified DFT+U formalisms shows qualitatively different results. The paramagnetic phase is stable for U=0.0eV, possibly due to the lager bandwidth compared to the case of Na_2IrO_3. At the intermediate correlation strength $0.0 < U \lesssim 1.0$eV, the zigzag phase is the ground state for both cases but the direction of the spin moment is different; while the y-direction is favored in the simplified DFT+U results, the moments tends to favor the xz-plane in the rotationally-invariant DFT+U calculations. For both cases, ferromagnetic phase with moments along the y-axis tends to be stabilized in $U \leq 2.0$eV regime as U in-

	U=0.0eV	U=0.5eV	U=1.0eV	U=1.5eV	U=2.0eV	U=3.0eV
Na_2IrO_3	ZZ	ZZ	ZZ	ZZ	ZZ	ZZ
	(0.00,0.16,0.00)	(0.14,0.00,0.20)	(0.15,0.00,0.20)	(0.15,0.00,0.21)	(0.15,0.00,0.21)	(0.10,0.00,0.26)
	ZZ : 4.8	ZZ : 2.0	ZZ : 5.0	ZZ : 5.9	ZZ : 1.2	ZZ : 1.7
	(0.11,0.00,0.17)	(0.00,0.19,0.00)	(0.00,0.20,0.00)	(0.00,0.21,0.00)	(0.19,0.00,0.18)	(0.23,0.00,0.14)
	Neel : 10.6	ST : 14.5	ST : 15.5	ST : 11.0	ZZ : 6.1	ST : 2.9
	(0.00,0.09,0.00)	(0.00,0.13,0.00)	(0.19,0.00,-0.18)	(0.20,0.00,-0.18)	(0.00,0.22,0.00)	(0.21,0.00,-0.21)
Li_2IrO_3	PM	ZZ	ZZ	ZZ	FM	FM
	(0.00,0.00,0.00)	(0.00,0.24,0.00)	(0.00,0.27,0.00)	(0.00,0.28,0.00)	(-0.01,0.36,0.00)	(-0.01,0.36,0.00)
		ZZ : 2.7	ZZ : 6.7	FM : 1.2	ZZ : 1.5	FM : 2.0
		(0.19,-0.01,0.09)	(0.26,0.00,0.08)	(-0.01,0.37,0.00)	(0.00,0.29,0.00)	(0.35,-0.01,-0.01)
		FM : 5.8	FM : 7.0	FM : 3.7	FM : 2.4	ZZ : 2.6
		(0.35,-0.01,0.01)	(-0.01,0.38,0.00)	(0.36,-0.01,0.00)	(0.35,-0.01,0.00)	(-0.01,0.30,0.00)

Table 4.4: Table of the magnetic ground states, first and second excited states of Na_2IrO_3 and Li_2IrO_3 with respect to the increasing on-site U from the LDA+SO+U calculations. For each rows the magnetic configuration, the energy difference with respect to the ground state per an unit cell(4 formula units), and the spin moment direction of the collinear spins. FM, ST, ZZ denote ferromagnetic, stripy, and zigzag phase, respectively. Spin moments are represented in the global xyz-coordinate.

	U=0.0eV	U=0.5eV	U=1.0eV	U=1.5eV	U=2.0eV	U=3.0eV
Na_2IrO_3	ZZ	ZZ	ZZ	ZZ	ZZ	ZZ
	(0.00,0.16,0.00)	(0.13,0.00,0.15)	(0.13,0.00,0.15)	(0.13,0.00,0.16)	(0.14,0.00,0.15)	(0.13,0.00,0.16)
	ZZ : 4.8	ZZ : 2.6	ZZ : 5.4	ZZ : 6.5	ZZ : 6.8	ZZ : 2.3
	(0.11,0.00,0.17)	(0.00,0.15,0.00)	(0.00,0.16,0.00)	(0.00,0.17,0.00)	(0.00,0.18,0.00)	(0.18,0.00,0.12)
	Neel : 10.6	Neel : 25.8	ST : 19.8	ST : 16.9	ST : 15.1	ZZ : 6.2
	(0.00,0.09,0.00)	(0.00,0.11,0.00)	(0.16,0.00,-0.15)	(0.17,0.00,-0.15)	(0.17,0.00,-0.15)	(0.00,0.19,0.00)
Li_2IrO_3	PM	ZZ	ZZ	ZZ	ZZ	ZZ
	(0.00,0.00,0.00)	(0.16,0.00,0.06)	(0.13,0.00,0.08)	(-0.01,0.00,0.10)	(-0.07,0.00,0.12)	(-0.09,0.00,0.14)
		ZZ : 2.3	ZZ : 2.5	FM : 0.9	FM : 1.8	Neel : 4.1
		(0.00,0.18,0.00)	(0.00,0.20,0.00)	(-0.01,0.29,0.00)	(-0.01,0.28,0.00)	(0.01,0.00,0.16)
		FM : 3.2	FM : 3.2	ST : 1.4	ZZ : 1.9	FM : 5.1
		(0.28,-0.01,0.01)	(-0.01,0.30,0.00)	(0.01,0.00,0.13)	(0.25,0.00,-0.05)	(0.00,0.28,0.00)

Table 4.5: Table of the magnetic ground states, first and second excited states of Na_2IrO_3 and Li_2IrO_3 with respect to the increasing on-site U from the LDA+SO+U calculations, where for the DFT+U calculation the rotationally-invariant form suggested by Lichtenstein *et al*[] was used with the value of the Hund's coupling J=0.5eV is adopted, except for U=0.0eV case for both compounds. For each rows the magnetic configuration, the energy difference with respect to the ground state per an unit cell(4 formula units), and the spin moment direction of the collinear spins. FM, ST, ZZ denote ferromagnetic, stripy, and zigzag phase, respectively. Spin moments are represented in the global *xyz*-coordinate.

	U=0.0eV	U=1.0eV	U=2.0eV	U=3.0eV
Li_2IrO_3	PM	ZZ	ZZ	ZZ
	(0.00,0.00,0.00)	(0.04,0.00,0.06)	(-0.07,0.00,0.09)	(-0.08,0.00,0.11)
		FM : 5.5	FM : 4.7	ST : 7.6
		(-0.01,0.25,0.00)	(-0.01,0.24,0.00)	(0.05,0.00,0.12)
		Neel : 5.7	FM : 6.0	FM : 7.8
		(0.01,0.00,0.10)	(0.23,-0.01,-0.01)	(0.00,0.23,0.00)

Table 4.6: Table of the magnetic ground states, first and second excited states of Li_2IrO_3 with respect to the increasing on-site U from the LDA+SO+U calculations, where for the DFT+U calculation the rotationally-invariant form suggested by Lichtenstein *et al*[] was used with the value of the Hund's coupling J=1.0eV is adopted, except for U=0.0eV case for both compounds. For each rows the magnetic configuration, the energy difference with respect to the ground state per an unit cell(4 formula units), and the spin moment direction of the collinear spins. FM, ST, ZZ denote ferromagnetic, stripy, and zigzag phase, respectively. Spin moments are represented in the global *xyz*-coordinate.

	U=0.0eV	U=0.5eV	U=1.0eV	U=1.5eV	U=2.0eV	U=3.0eV
Na_2IrO_3	ZZ	ZZ	ZZ	ST	ST	ST
	(0.14,0.00,0.23)	(0.15,0.00,0.22)	(0.15,0.00,0.22)	(0.22,0.00,-0.20)	(0.23,0.00,-0.20)	(0.25,0.00,-0.18)
	ZZ : 6.1	ZZ : 8.5	ST : 2.8	ZZ : 0.2	ZZ : 2.1	ST : 1.8
	(0.00,0.18,0.00)	(0.00,0.19,0.00)	(0.21,0.00,-0.19)	(0.15,0.00,0.23)	(0.15,0.00,0.23)	(0.21,0.00,-0.24)
	ST : 21.7	ST : 9.3	ZZ : 9.3	ZZ : 0.5	ZZ : 10.6	ZZ : 3.6
	(0.20,0.00,-0.18)	(0.20,0.00,-0.19)	(0.00,0.20,0.00)	(0.22,0.00,-0.18)	(0.00,0.21,0.00)	(0.15,0.00,0.25)
Li_2IrO_3	FM	FM	FM	FM	FM	FM
	(0.42,-0.03,0.01)	(0.05,-0.46,0.00)	(0.02,-0.44,0.00)	(0.01,-0.41,0.00)	(0.01,-0.40,0.00)	(0.01,-0.39,0.00)
	FM : 0.4	FM : 1.3	FM : 3.5	FM : 2.9	FM : 2.4	FM : 1.6
	(0.01,-0.43,0.00)	(0.45,-0.02,0.01)	(0.43,-0.02,0.00)	(0.40,-0.01,0.00)	(0.39,-0.01,0.00)	(0.38,-0.01,-0.01)
	ZZ : 16.4	ZZ : 12.4	ZZ : 9.0	ZZ : 9.4	ZZ : 8.7	ZZ : 6.8
	(0.01,-0.24,0.00)	(0.01,-0.30,0.00)	(0.01,-0.30,0.00)	(0.01,-0.30,0.00)	(0.01,-0.31,0.00)	(0.01,-0.32,0.00)

Table 4.7: Table of the magnetic ground states, first and second excited states of Na_2IrO_3 and LI_2IrO_3 with respect to the increasing on-site U from the GGA+SO+U calculations. For each rows the magnetic configuration, the energy difference with respect to the ground state per an unit cell(4 formula units), and the spin moment direction of the collinear spins. FM, ST, ZZ denote ferromagnetic, stripy, and zigzag phase, respectively. Spin moments are represented in the global xyz-coordinate.

creases. The ferromagnetic phase becomes the ground state at $U \leq 2.0$eV in the simplified DFT+U calculations, while in the rotationally-invariant DFT+U calculations the zigzag phase with the moments on the xz-plane persists to be the ground state up to $U \geq 3.0$eV, which is consistent with the other LDA+SO+U calculation results adopting the same DFT+U scheme[34]. Such tendency is also observed in the result of J=1.0eV calculations in Table 4.6, except that the stripy phase is stabilized at $U = 3.0$eV instead of the Neel phase.

Although the ground state from the rotationally-invariant LDA+U calculations are consistent with the result from our spin model energy analysis, still some inconsistency is observed. One can notice that, the energy of the Neel and stripy phase becomes lowered while the ferromagnetic phase becomes more costly in energy in the results of the rotationally-invariant DFT+U calculations. Roughly speaking, the difference between the simplified and the rotationally-invariant DFT+U results in this system is the presence of the inter-orbital matrix elements dependent to the Hund's coupling, from which the multiplet excited states yielding (4.6) are induced. Fig. 4.4.(d) tells us that the larger K_{1n} yields the lower energy of the ferromagnetic and zigzag phase. Yet, our DFT calculations with $J = 0, 0.5, 1.0$eV, of which results are in Table 4.4, 4.5, and 4.6, respectively, does not show such behavior. Rather, the role of the inter-orbital terms in the rotationally-invariant DFT+U seems to reduce the differences in energy of different magnetic configurations in our system, which is in contrary to the model results. Since the rotationally-invariant DFT+U formalism contains various inter-orbital interaction channels, it may introduce contributions other than the one yielding

(4.6), which points we do not investigate further in this thesis.

For the GGA results in Table 4.7, The tendency becomes quite confusing compared to the LDA results. First, in the case of Na_2IrO_3, the stable stripy phase in the high-U region is somewhat contradictory to the neutron data and the result of the LDA+SO+U calculations performed with by the WIEN2K code[34] which favor zigzag order. Since the different of the energy, the results can be affected depending on the exchange-correlation functionals. Also in the case of Li_2IrO_3, contrary to our model analysis and also to other DFT calculation results[34], in our DFT calculation FM phase is stable in our parameter range of $0 \leq U \leq 3.0$eV. The energy difference with the zigzag phase tends to decrease along the increasing U, but one needs unrealistically large value of U to stabilize the zigzag phase. Regarding the shorter Ir-Ir distance which favors nearest-neighbor AF Heisenberg terms these dominance of the FM phase is somewhat hard to understand. Such results may imply that the GGA functional, which favors lager density gradients and fits to the molecular systems, is not suitable at least in treating the 5d-transition metal oxides where the 5d-orbitals are spatially well-extended.

4.6 Discussions

In our GGA+SO+U calculations, the $\mathscr{H}_{\text{spin}}$ the $j_{\text{eff}} = 1/2$-ness of our Wannier orbitals are sustained yet the character is modified by the inclusion of the correlation, and especially by the shift of the orbital center which comes in in the processes of the orbital spread minimizations. Considering how much the amount of modifications are physically meaningful, and

how much amounts are the artifacts included in the calculations is not easy subject at this moment. In the previous sections, we considered the shift of the Wannier orbital centers only to discuss issue of the stabilizations of the AF-dimers of the Wannier orbitals, and in the construction of the spin Hamiltonians we used the results without inclusion of the U. One reason is that we did not have the the superexchange formalism with the broken on-site time-reversal symmetry, in which the the meaning of the each hopping terms becomes much more complex. Deriving spin Hamiltonian based on the $j_{\rm eff} = 1/2$-Wannier orbitals with broken time-reversal symmetry with fixed Wannier centers may gives more relevant spin models for both compounds, and is an interesting future subject.

The delocalized nature of our $j_{\rm eff} = 1/2$-Wannier orbital may have considerable importance when the on-site correlation U on the Ir sites is considered, since the on-site U-matrix on the t_{2g} complex is folded into the $j_{\rm eff} = 1/2$-Wannier space to yield nearest-neighbor inter-site Coulomb repulsions, whose strength is roughly proportional the ratio between the $j_{\rm eff} = 1/2$ and $3/2$ components. Although weak, still such inter-site Coulomb repulsions may tune the nature of the electronic and the magnetic ground states and the elementary excitations, as suggested in recent resonant inelastic X-ray spectroscopy measurements[46].

Estimation of the spin Hamiltonian including both the $j_{\rm eff} = 1/2$- and $3/2$-complexes may suggest clearer insight to the understanding of the microscopic mechanism for the magnetism of these compounds. Our approach in this work, which combines two different results from two different contributions, are somewhat artificial, and it also suspected to miss additional

interaction channels as in the case of the next-nearest-neighbor terms in Na_2IrO_3 in our spin model analysis. Discrepancy with the experimental values of the nearest-neighbor Heisenberg term J_{n1} is another problem, since in the spin-wave spectrum J_{n1} is estimated to be about 4.5meV for Na_2IrO_3[65], which is more than three times larger than the values we calculated. More elaborate schemes such as the one developed in Ref. [72] is needed to treat entire $j_{\text{eff}} = 1/2$- and $3/2$-complexes on equal footing.

Finally, the validity of the pseudopotential-based DFT calculations in the compounds including heavy-elements such as Ir as in this work. In the band structure calculation different schemes gives almost identical results, but in the total energy calculations of various magnetic configurations where the energy difference is very small it can give significant differences.

Chapter 5

Summary and Perspectives

In this thesis, we have investigated the basic electronic structure with and without the SOC and the on-site U for Na_2IrO_3 and Li_2IrO_3. First, in the absence of the SOC, we have investigated the major hopping channels for the t_{2g} electrons, and also discussed how the strong hybridization of Ir t_{2g}- and oxygen p-orbitals affects the electronic structures in theses layeres compounds. Also, the role of the A-site cation on the electronic structure is investigates, which is found to be just the source for the electron and the electrostatic potentials. As SOC is turned on, the robustness of the $j_{\text{eff}} = 1/2$ is checked on both compounds, and the effective noninteracting models suggested on these systems are compared to the realistic cases. Although we need some perturbations such as lattice strains, this systems, especially in the case of Li_2IrO_3, can host strong topological insulator phases, and has possibility to be the candidate of the topological insulators with moderate on-site correlations.

One can question that, whether the arguments we have made for the

non-interacting electrons in this thesis hold for other layered compounds with one holes in the t_{2g}-complex. Especially, whether the $j_{\mathrm{eff}} = 1/2$-ness of the low-energy degree of freedom is universal or not in the systems of $5d$ transition metal with cubic symmetry with d^5 configuration is an interesting question. We deduce that the robustness of the $j_{\mathrm{eff}} = 1/2$ depends on the competition between the SOC and the hopping terms between the $\{t_{2g}+p\}$-Wannier basis, especially the *dpd-pi*-type bonding that induces quasi-molecular orbital stateMazinQMO. In $A_2\mathrm{IrO}_3$ compounds it is smaller than SOC, so the $j_{\mathrm{eff}} = 1/2$ character remain intact. In other layered compounds such as IrTe_2[74], the *dpd-pi*-type hopping terms might greatly enhanced owing to the spatially extended *p*-orbitals and also the smaller on-site energy differences $\Delta\varepsilon_{pd}$. so that SOC might be quenched in such systems. Detailed electronic structure calculations on those compounds might be intriguing subjects.

Due to the crystal structure, various type of disorder are easy to predominate these type of compounds. Especially the layer-stacking type disorder are known to be very easy to occur in these layered iridates[65]. Although small compare to the change of the in-plane hopping terms, the effect of the different stacking order on the electronic structure has not been discussed yet. Although the system is already gapped, such dramatic changes such as in the case of multilayer graphenes may not happen, still such disorders might help the system to be topologically nontrivial as in the case of the topologcal Anderson insulators[67]. Also, the effect of the in-plane site mixing might give interesting effect on the electronic and magnetic properties, which are worth to be the future projects for these materials.

As we incorporate the on-site Coulomb interactions, it is found that the $j_{\text{eff}} = 1/2$-ness of the states near the Fermi level remains intact, and the application of the effective models based on the $j_{\text{eff}} = 1/2$-Wannier basis can be justified. Our spin models for Na_2IrO_3 and Li_2IrO_3, which are derived from the noninteracting effective Hamiltonian by using the perturbation theory, shows qualitative difference but yields the same zigzag phase to be the ground state, which is also the ground state from our LDA+SO+U calculations. The presence of the DM interactions, which only exists in the case of Li_2IrO_3, seems not affecting the collinear ground state at a classical level.

One can also study the superlattice or thin-flim of the these compounds to increase the low-dimensionality, and also incorporating the effective of the disorder. The inter-layer couplings in these system are significant, and the effect of the low-dimensionality can affect the electronic structure and magnetic properties significantly. To enhance the low-dimensionality, one can fabricate superlattice of alternating layers of Ir and d^0 or d^6 atoms such as Sn. Removing the interlayer coupling will change the electronic and magnetic structure significantly, and will yield two-dimensional quantum magnets which is tunable by chemical pressure and external lattice strain.

Overall, layered iridate systems has very rich electronic and magnetic diversity due to the various chemical compositions, lattice strains, and disorders. Also the possible topologically nontrivial phases in the weak- and strong-correlation limit makes them to be physically interesting and practically important materials.

Appendix A

Table of $j_{\text{eff}} = 1/2$ hopping terms

In this appendix we present more detailed information about our effective $j_{eff} = 1/2$ tight-binding Hamiltonian. Since our Wannier orbitals are spatially broader than atomic d-orbitals, the hopping terms between the Ir atoms even beyond sixth nearest-neighbor doesn't decay out. But the key features in our Hamiltonian - the band inversion at the M_2 point, and the exchange interactions - is recovered only with the terms up to third nearest-neighbor inter- and inter-layer hopping. So in Table A.1 we list up the first 30 distinct kind of hopping terms calculated from our Wannier interpolation calculation.

$\mathbf{r}_{ij}$	$C^0_{\mathbf{r}_{ij}}$	$C_{\mathbf{r}_{ij},x}$	$C_{\mathbf{r}_{ij},y}$	$C_{\mathbf{r}_{ij},z}$
$000;\mathrm{A} \to 000;\mathrm{B}$	-0.016	0.000	0.000	-0.001
$000;\mathrm{B} \to 010;\mathrm{A}$	-0.008	0.000	0.000	0.000
$000;\mathrm{B} \to 110;\mathrm{A}$	-0.006	0.000	0.000	0.000
$000;\mathrm{A} \to 100;\mathrm{A}$	-0.019	0.000	0.000	0.038
$000;\mathrm{A} \to 010;\mathrm{A}$	-0.020	-0.035	-0.008	0.004
$000;\mathrm{A} \to 100;\mathrm{A}$	-0.019	0.008	-0.035	-0.005
$000;\mathrm{A} \to 100;\mathrm{B}$	-0.035	0.000	0.000	0.000
$000;\mathrm{B} \to 100;\mathrm{A}$	-0.035	0.000	0.000	0.000
$000;\mathrm{B} \to 120;\mathrm{A}$	-0.036	0.000	0.000	0.000
$000;\mathrm{A} \to \bar{1}01;\mathrm{A}$	-0.019	0.000	0.000	-0.002
$000;\mathrm{A} \to 001;\mathrm{B}$	-0.014	0.000	0.000	0.000
$000;\mathrm{B} \to 001;\mathrm{A}$	-0.014	0.000	0.000	0.000
$000;\mathrm{A} \to 101;\mathrm{B}$	0.013	0.000	0.000	0.000
$000;\mathrm{A} \to \bar{1}01;\mathrm{B}$	0.009	0.000	0.000	0.000
$000;\mathrm{B} \to \bar{1}01;\mathrm{A}$	0.009	0.000	0.000	0.000
$000;\mathrm{B} \to 021;\mathrm{A}$	0.008	0.000	0.000	0.000
$000;\mathrm{B} \to 22\bar{1};\mathrm{A}$	0.008	0.000	0.000	0.000
$000;\mathrm{B} \to 11\bar{1};\mathrm{A}$	-0.008	0.000	0.000	0.000
$000;\mathrm{B} \to 011;\mathrm{A}$	-0.008	0.000	0.000	0.000
$000;\mathrm{B} \to 111;\mathrm{A}$	-0.007	0.000	0.000	0.000
$000;\mathrm{A} \to 0\bar{1}1;\mathrm{B}$	-0.007	0.000	0.000	0.000
$000;\mathrm{A} \to 001;\mathrm{A}$	-0.003	0.000	0.000	-0.006
$000;\mathrm{B} \to 001;\mathrm{B}$	-0.003	0.000	0.000	0.006
$000;\mathrm{B} \to 220;\mathrm{A}$	-0.006	0.000	0.000	0.000
$000;\mathrm{B} \to 020;\mathrm{A}$	-0.006	0.000	0.000	0.000
$000;\mathrm{B} \to 210;\mathrm{A}$	-0.005	0.000	0.000	0.000
$000;\mathrm{A} \to 1\bar{1}0;\mathrm{B}$	-0.005	0.000	0.000	0.000
$000;\mathrm{B} \to \bar{1}11;\mathrm{A}$	-0.005	0.000	0.000	0.000
$000;\mathrm{B} \to 21\bar{1};\mathrm{A}$	-0.005	0.000	0.000	0.000
$000;\mathrm{A} \to 010;\mathrm{B}$	-0.005	0.000	0.000	0.000

Table A.1: Partial list of up to thirty largest hopping terms following the notation of (3.12). The notation in the first column is explained in Fig.A.1. The full list is recovered by applying the hermiticity $C^0_{\mathrm{r}_{ij}} = C^0_{\mathrm{r}_{ji}}$ and $\mathbf{C}_{\mathrm{r}_{ij}} = -\mathbf{C}_{\mathrm{r}_{ji}}$, due to the hermiticity, and also $\mathbf{C}_{\mathrm{r}_{ij};\mathrm{A}\to\mathrm{A}} = -\mathbf{C}_{\mathrm{r}_{ij};\mathrm{B}\to\mathrm{B}}$ where A and B are the sublattice indices.

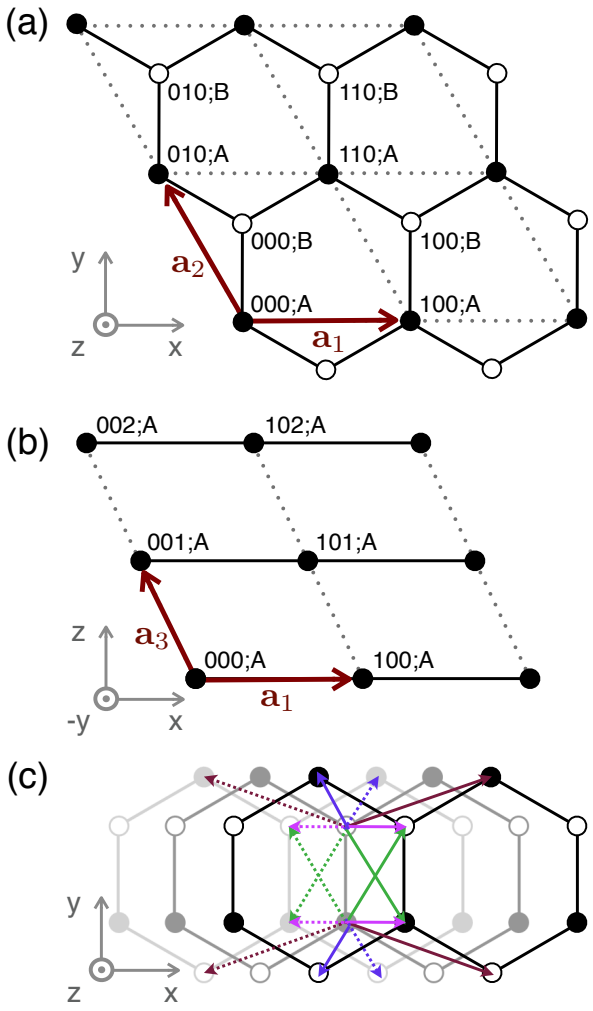

Figure A.1: (Color online) (a) shows planar view of an Ir honeycomb lattice with position index of each Ir atoms in terms of the Bravais lattice vectors, with a single unit cell represented as dotted lines. (b) shows side view of the stacking of Ir lattices. In (a) and (b) $\mathbf{a}_1$ to $\mathbf{a}_3$ are the Bravais lattice vectors of the unit cell used in this calculation. (c) shows projected view of adjacent Ir layers onto the xy-plane, and major inter-layer hopping terms are illustrated as arrows with different colors and line types.

Bibliography

[1] M. Z. Hasan, and C. L. Kane, Rev. Mod. Phys. **82**, 3045 (2010).

[2] C. L. Kane, and E. J. Mele, Phys. Rev. Lett. **95**, 146802 (2005).

[3] C. L. Kane, and E. J. Mele, Phys. Rev. Lett. **95**, 226801 (2005).

[4] F. D. M. Haldane, Phys. Rev. Lett. **61**, 2015 (1988).

[5] Y. Yao, F. Ye, X. -L. Qi, S. -C. Zhang, and Z. Fang, Phys. Rev. B **75**, 041401(R) (2007)

[6] S. Murakami, Phys. Rev. Lett. **97**, 236805 (2006).

[7] A. Shitade *et al.*, Phys. Rev. Lett. **102**, 256403 (2009).

[8] Z. Y. Meng *et al.*, Nature **464**, 847 (2010).

[9] M. Hohenadler, T. C. Lang, and F. F. Assaad, Phys. Rev. Lett. **106**, 100403 (2011).

[10] D. Pesin and L. Balents, Nature Physics **6**, 376 (2010).

[11] M. Levin and A. Stern, Phys. Rev. Lett. **103**, 196803 (2009).

[12] Y. Yamaji and M. Imada, Phys. Rev. B **83**, 205122 (2011).

[13] A. Kitaev, Ann. Phys. (N.Y.) 321, 2 (2006).

[14] R. Martin, *Electronic Structures: Basic Theory and Practical Methods*, Cambride University Press, 2008.

[15] P. Hohenberg and W. Kohn, Phys. Rev. **136** B864 (1964).

[16] W. Kohn and L. J. Sham, Phys. Rev. **140**, A 1133, (1965).

[17] D. M. Ceperley and B. J. Alder, Phys. Rev. Lett. **45**, 566 (1980).

[18] J. P. Perdew, K. Burke, and M. Ernzerhof, Phys. Rev. Lett. **77**, 3865 (1996).

[19] V. I. Anisimov, J. Zaanen and O. K. Andersen, Phys. Rev. B **44**, 943 (1991).

[20] A. I. Lichtenstein, J. Zaanen, and V. I. Anisimov, Phys. Rev. B 52, 5467(R), (1995).

[21] S. L. Dudarev, G. A. Botton, S. Y. Savrasov, C. J. Humphreys and A. P. Sutton, Phys. Rev. B **57**, 1505 (1998).

[22] M. T. Czyzyk and G. A. Sawatzky, Phys. Rev. B **49**, 14211 (1994).

[23] W. E. Pickett, S. C. Erwin and E. C. Ethridge, Phys. Rev. B **58**, 1201 (1998).

[24] U. Von Barth and L. Hedin, J. Phys. C: Solid State Phys. **5**, 1629 (1972).

[25] J. Kubler, K-H. Hock, J. Sticht and A. R. Williams, J. Phys. F: Met. Phys. **18**, 469 (1988).

[26] G. Theurich and N. A. Hill, Phys. Rev. B **64**, 073106 (2001).

[27] http://www.scipy.org

[28] G. Kresse and J. Hafner, Phys. Rev. B **47**, 558 (1993).

[29] J. Chaloupka, G. Jackeli, and G. Khaliullin, Phys. Rev. Lett. **105**, 027204 (2010).

[30] G. Jackeli and G. Khaliullin, Phys. Rev. Lett. **102**, 017205 (2009).

[31] H.-C. Jiang *et al.*, Phys. Rev. B **83**, 245104 (2011).

[32] J. Reuther, R. Thomale, and S. Trebst, Phys. Rev. B **84**, 100406(R) (2011).

[33] Y. Singh and P. Gegenwart, Phys. Rev. B **82**, 064412 (2010).

[34] Y. Singh *et al.*, Phys. Rev. Lett. **108**, 127203 (2012).

[35] I. Kimchi, and Y. -Z. You, Phys. Rev. B **84**, 180407(R) (2011).

[36] S. Bhattacharjee, S. -S. Lee, and Y. B. Kim, arXiv:1108.1806 (2012).

[37] H. Zhang *et al.*, Nature Physics **5**, 438 (2009).

[38] B. J. Kim *et al.*, Phys. Rev. Lett. **101**, 076402 (2008).

[39] B. J. Kim *et al.*, Science **323**, 1329 (2009).

[40] H. Jin *et al.*, Phys. Rev. B **80**, 075112 (2009).

[41] H. Jin *et al.*, arXiv:0907.0743 (2009).

[42] C. H. Kim *et al.*, Phys. Rev. Lett. **108**, 106401 (2012).

[43] Y. Okamoto *et al.*, Phys. Rev. Lett. **99**, 137207 (2007).

[44] B. -J. Yang, and Y. B. Kim, Phys. Rev. B **82**, 085111 (2010).

[45] X. Liu *et al.*, Phys. Rev. B **83**, 220403(R) (2011).

[46] H. Gretarsson *et al.*, arXiv:1209.5424.

[47] R. Comin *et al.*, Phys. Rev. Lett. **109**, 266406 (2012).

[48] C. H. Sohn *et al.*, To be submitted.

[49] H. Kobayashi *et al.*, J. Mater. Chem. **13**, 957 (2003).

[50] M. J. OḾalley, H. Verweij, and P. M. Woodward, J. Solid. State. Chem. **181**, 1803 (2008).

[51] The DFT code, OpenMX, is available at the web site (http://www.openmx-square.org) in the constitution of the GNU General Public License.

[52] T. Ozaki, Phys. Rev. B **67**, 155108 (2003).

[53] T. Micklitz, and M. R. Norman, Phys. Rev. B **81**, 174417 (2010).

[54] A. H. MacDonald, and S. H. Vosko, J. Phys. C: Solid State Phys. **12**, 2977 (1979).

[55] G. B. Bachelet, D. R. Hamann, and M. Schlüter, Phys. Rev. B **26**, 4199 (1982).

[56] G. Theurich and N. A. Hill, Phys. Rev. B **64**, 073106 (2001).

[57] N. Marzari and D. Vanderbilt, Phys. Rev. B **56**, 12847 (1997).

[58] I. Souza, N. Marzari, and D. Vanderbilt, Phys. Rev. B **65**, 035109 (2001).

[59] J. P. Perdew, and A. Zunger, Phys. Rev. B **23**, 5048 (1981).

[60] M. J. Han, T. Ozaki, and J. Yu, Phys. Rev. B **73**, 045110 (2006).

[61] L. Fu and C. L. Kane, Phys. Rev. B **76**, 045302 (2007).

[62] L. Fu, C. L. Kane, and E. J. Mele, Phys. Rev. Lett. **98**, 106803 (2007).

[63] X. Wan *et al.*, Phys. Rev. B **83**, 205101 (2011).

[64] L. Balents, Physics **4**, 36 (2011).

[65] S. K. Choi *et al.*, Phys. Rev. Lett. **108**, 127204 (2012).

[66] F. Ye *et al.*, Phys. Rev. B **85**, 180403(R) (2012).

[67] J. Li *et al.*, Phys. Rev. Lett. **102**, 136806 (2009).

[68] J. Reuther, R. Thomale, and S. Rachel, Phys. Rev. B **86**, 155127 (2012).

[69] M. Kargarian, A. Langari, and G. A. Fiete, Phys. Rev. B **86**, 205124 (2012).

[70] A. Rüegg, and G. A. Fiete, Phys. Rev. Lett. **108**, 046401 (2012).

[71] R. Arita *et al.*, Phys. Rev. Lett. **108**, 086403 (2012).

[72] B.H. Kim, G. Khaliullin, and B.I. Min, Phys. Rev. Lett. **109**, 167205 (2012).

[73] I.I. Mazin *et al.*, Phys. Rev. Lett. **109**, 197201 (2012).

[74] S. Pyon, K. Kudo, and M. Nohara, J. Phys. Soc. Jpn, **81**, 053701 (2012).

국문 초록

원자의 스핀-궤도 결합(Spin-orbit coupling, SOC)은 원자 핵 부근의 전자들이 느끼는 상대론적 효과에 의해 발생하며, 따라서 원자 핵의 쿨롱 포텔셜의 크기가 강해지는 무거운 원소들로 구성된 물질에서 중요한 에너지 잣대가 된다. 이러한 스핀-궤도 결합은 금속 표면에서의 라쉬바 효과(Rashba effect) 또는 3차원 위상 절연체 (Topological insulator)를 이끌어 내는 동인으로서 알려져 있고, 또한 그 외 여러 가지의 양자적 자기 상태를 유도해 낼 것이라 제안되고 있다. 스핀-궤도 결합은 고체 내에서 총 각운동량 j를 양자수로 가지는 스핀-오비탈 얽힘 상태를 만들어내고, 이러한 얽힘 상태들을 기저로 하여 다양한 새로운 종류의 양자 상태들이 발생할 수 있다. 그 중에서도 특별히 $Sr_{n+1}Ir_nO_{3n+1}$ ($n = 1, 2, \infty$) 처럼 전이원소 주변에 국소적인 정육면체 대칭성을 가지는 $5d$-전이원소 산화물의 경우에는, 이리듐 원자의 t_{2g} d-오비탈과 $s = 1/2$ 스핀 성분이 결합되어 이루어지는 $j_{\mathrm{eff}} = 1/2$ 상태가 페르미 준위 근방에서의 전자의 자유도로서 기능하게 된다. 여기에, $5d$-전이원소 산화물에서의 또 다른 중요한 에너지 잣대인 쿨롱 전자 상호작용이 더해져 다양한 창발적인(emergent) 양자 상태들이 유도될 수 있음이 제안되고 있다. 본 논문에서 다루는 A_2IrO_3 (A=Na,Li) 계열 화합물의 경우, 이론적으로 $j_{\mathrm{eff}} = 1/2$ 상태를 기반으로 한 약한 위상 절연체 상태(Weak-topological insulator) 와 또한 강한 상호작용이 존재하는 극한에서의 키타에프 스핀-액체 상태(Kitaev spin-liquid) 가 제안

되어 있다. 다만, $j_{\mathrm{eff}} = 1/2$ 상태가 존재함이 이론과 실험 양 쪽에서 증명된 $Sr_{n+1}Ir_nO_{3n+1}$ 의 경우와는 달리, A_2IrO_3 계열 화합물에서는 이러한 가정에 대한 검증이 이루어 진 적이 없다.

본 논문에서는, A_2IrO_3 계열 화합물의 전자적 상태에 스핀-궤도 결합이 끼치는 영향, 특히 $j_{\mathrm{eff}} = 1/2$ 상태의 존재 여부와 또한 그로부터 발생하는 양자적 상태들을 다룰 것이다. 실제적인 결정 구조에 기반한 정량적인 결과 분석을 위해서, 본 논문에서는 밀도 범함수 이론(Density functional theory)에 기반한 전자구조 계산을 사용할 것이다. 이를 통해서 우리가 다루고자 하는 물질의 밴드 구조를 얻어내고 분석하며, 또한 강한 스핀-궤도 결합이 이 물질의 밴드에 끼치는 어떠한 영향을 끼치는지를 이해하고, 본 논문에서 다루는 에너지 영역 안에서의 가장 국소화된 와니어 오비탈(Maximally-localized Wannier orbital)을 생성, 이로부터 유효 해밀토니안을 유도할 것이다. 이리듐의 t_{2g}-오비탈만을 포함한 와니어 오비탈과 또한 산소의 p-오비탈까지 전부 포함한 와니어 오비탈을 비교함으로서, 이 물질의 밴드 구조에 기여하는 다양한 이리듐과 산소 사이의 전자 건너뜀 경로(Hopping channel)들을 분석하며, 이를 통해서 결정에 가해지는 압력과 이로 인한 결정상수의 변화가 전자 구조에 끼치는 영향을 이해하게 될 것이다. 또한, 같은 방법을 사용하며, 페르미 준위 근처의 상태들이 $j_{\mathrm{eff}} = 1/2$ 로서의 성질을 가짐을 확인하는 동시에, 이 상태들을 기저로 하는 유효 해밀토니안이 이 물질에 대해 이론적으로 제안되었던 모델들과 유사한 성질을 가진다는 것을 보일 것이다. 만들어진 유효 해밀토니안을 통해서, 두번째와 세번째로 가까운 건너뜀 경로들이 전자 구조에 큰 영향을 끼치는 것을 알 수 있으며, 이에 비해 상대적으로 작은 인접한 이리듐 층 사이의 연결 또한 전자 구조에 무시할 수 없는 영향을 끼치는 것을 알 수 있다. 이 중, 세 번째 이웃과 첫번째 이웃 사이를 잇는 건너뜀 성분 사이의 비율이 이 물질에서의 밴드 절연체와 위상 절연체 사이의 상전이를 유도하

며, 결정 구조에 가해지는 압력을 통해서 이 비율을 조절할 수 있다는 사실을 예측할 수 있다.

본 논문에서는 또한, 이리듐 5*d*-오비탈의 전자 간의 상호작용이 그 외 다른 에너지 잣대보다 강해지는 영역에서 약한 상호작용 영역에서의 결과에 기반하여 스핀들 사이의 자성을 결정하는 유효 해밀토니안을 유도할 것이다. 결과로서 유도되는 $j_{\mathrm{eff}} = 1/2$ 유사스핀 해밀토니안은, 하이젠버그 항 뿐 아니라 키타에프 항, 그리고 선행 연구들에서는 그 존재가 예측되지 않았던 지알로신스키-모리야(Dzyaloshinskii-Moriya) 항 역시 존재한다. 여기에서 유도된 해밀토니안을 이전 연구들과 비교하여 이 모델의 바닥 상태를 추측해 낼 것이며, 또한 모델의 고전적인 바닥 상태와 그 상태에서의 스핀 배열에 대한 계산 결과를 소개할 것이다. 모델 방법론을 사용하여 얻은 결과들을 DFT+U 방법을 사용하여 계산한 스핀 바닥 상태와 또한 실험적인 결과들과 비교하며, 마지막으로 우리가 사용한 방법론의 한계에 대해서 논할 것이다.

본 연구는 $A_2\mathrm{IrO}_3$ 계열 화합물 뿐 아니라 유사한 구조를 가진 다른 층상 산화물의 전자구조에 대한 구체적인 이해를 높이며, 보다 정밀한 이론적인 분석을 위한 현실적인 시작점을 제공할 것이다.

주요어 밀도범함수 이론, 5*d*-전이금속 산화물, 스핀-궤도 결합, 쿨롱 상호작용, 위상 절연체, 와니어 오비탈

학번 2005-23191